



NATIONAL TECHNICAL UNIVERSITY OF ATHENS
INTERDISCIPLINARY POSTGRADUATE PROGRAM
“MATERIALS SCIENCE & TECHNOLOGY”

**STUDY OF THE SIMULTANEOUS EFFECT OF PULSE
CURRENT PARAMETERS AND ORGANIC ADDITIVES
ON THE ELECTROLYTIC DEPOSITION OF
Ni-MATRIX/ZrO₂ NANOCOMPOSITE COATINGS**

MASTER THESIS
ANGELIKI NIKOLAOU
Physicist of NKUA

SUPERVISION

Dr. Constantina Kollia
Professor at NTUA

ATHENS, MARCH 2024



NATIONAL TECHNICAL UNIVERSITY OF ATHENS
INTERDISCIPLINARY POSTGRADUATE PROGRAM
“MATERIALS SCIENCE & TECHNOLOGY”

**STUDY OF THE SIMULTANEOUS EFFECT OF PULSE
CURRENT PARAMETERS AND ORGANIC ADDITIVES
ON THE ELECTROLYTIC DEPOSITION OF
Ni-MATRIX/ZrO₂ NANOCOMPOSITE COATINGS**

MASTER THESIS
ANGELIKI NIKOLAOU
Physicist of NKUA

EXAMINATION COMMITTEE

CONSTANTINA KOLLIA

Professor of NTUA

.....

.....

ATHENS, March 2024



ΕΘΝΙΚΟ ΜΕΤΣΟΒΙΟ ΠΟΛΥΤΕΧΝΕΙΟ
ΔΙΑΤΜΗΜΑΤΙΚΟ ΠΡΟΓΡΑΜΜΑ
ΜΕΤΑΠΤΥΧΙΑΚΩΝ ΣΠΟΥΔΩΝ (Δ.Π.Μ.Σ.)
"ΕΠΙΣΤΗΜΗ ΚΑΙ ΤΕΧΝΟΛΟΓΙΑ ΥΛΙΚΩΝ"

**ΜΕΛΕΤΗ ΤΑΥΤΟΧΡΟΝΗΣ ΕΠΙΔΡΑΣΗΣ
ΠΑΡΑΜΕΤΡΩΝ ΤΟΥ ΠΑΛΜΙΚΟΥ ΡΕΥΜΑΤΟΣ
ΚΑΙ ΟΡΓΑΝΙΚΩΝ ΠΡΟΣΘΕΤΩΝ ΣΤΗΝ
ΗΛΕΚΤΡΟΑΠΟΘΕΣΗ Ni/ZrO₂ ΝΑΝΟΣΥΝΘΕΤΩΝ
ΕΠΙΚΑΛΥΨΕΩΝ**

ΜΕΤΑΠΤΥΧΙΑΚΗ ΕΡΓΑΣΙΑ

ΑΓΓΕΛΙΚΗΣ ΝΙΚΟΛΑΟΥ

Φυσικός ΕΚΠΑ

ΕΠΙΒΛΕΨΗ

ΚΟΛΛΙΑ ΚΩΝΣΤΑΝΤΙΝΑ

Καθηγήτρια ΕΜΠ

ΑΘΗΝΑ, Μάρτιος 2024

Abstract

This master's thesis is dedicated to exploring the effects of pulse current parameters, organic additives, and their combined effects on the electrolytic deposition process, with a specific focus on the development of Ni-Matrix/ZrO₂ nanocomposite coatings. The study encompasses a comprehensive investigation involving 27 meticulously prepared samples, each meticulously crafted to encompass a broad spectrum of experimental conditions. Central to this investigation is the utilization of 2-butyne-1,4-diol as the primary brightener (organic additive), accompanied by the application of both pulse and direct current methodologies to elucidate their distinct influences on coating formation and properties.

In this thesis, the effect of organic additives, type of current and type of nanoparticles are identified as primary variables controlling the metal crystallization and coatings properties.

The experimental design is underpinned by attention to detail and methodological precision. Parameters such as pH, current density, stirring rate, and temperature are controlled and maintained at consistent levels throughout the duration of the study, ensuring reliability and reproducibility of results. By adhering to rigorous experimental protocols, this research aims to provide comprehensive insights into the nuanced interactions between key process variables and their cumulative impact on coating morphology, structure, and performance.

The structural and surface properties of the coatings are characterized using a diverse array of analytical techniques, including scanning electron microscopy (SEM), energy-dispersive X-ray spectroscopy (EDS), X-ray diffraction (XRD), and surface roughness testing. These techniques afford a detailed understanding of the microstructural evolution, phase composition, and surface topography of the deposited coatings, enabling correlations to be drawn between process parameters and observed material properties.

In addition to structural characterization, the mechanical properties of the coatings are assessed through Vickers microhardness measurements. By quantifying the mechanical response of the coatings to applied loads, valuable insights are gained into their hardness, durability, and resistance to deformation, thereby informing potential applications in diverse engineering contexts.

Through this multidisciplinary approach, this research endeavors to advance our fundamental understanding of electrolytic deposition processes and pave the way for the development of tailored Ni-Matrix/ZrO₂ nanocomposite coatings with enhanced performance characteristics. By elucidating the complex relationships between pulse current parameters, organic additives, and coating properties, this study aims to contribute to the ongoing discourse surrounding surface engineering and materials science, ultimately facilitating the realization of innovative solutions for a broad spectrum of industrial applications.

In summary, this master's thesis represents a comprehensive exploration of the simultaneous effects of pulse current parameters and organic additives on the electrolytic deposition of Ni-Matrix/ZrO₂ nanocomposite coatings. The main objective of this work is to identify the electrocrystallization interactions in the production of Ni-Matrix/ZrO₂ nanocomposites. A series of experiments are designed to isolate single variables and identify the controlling parameters of these interactions and their impact on the final properties.

Through meticulous experimentation, rigorous analysis, and systematic characterization, this research endeavors to expand the frontiers of knowledge in the field of surface engineering and catalyze advancements in materials science and technology.

Περίληψη

Η παρούσα διατριβή αφορά στη μελέτη των επιδράσεων των παραμέτρων του παλμικού ρεύματος, των οργανικών προσθέτων και της συνιστάμενης επίδρασης τους στη διαδικασία ηλεκτρολυτικής απόθεσης, με έμφαση στην ανάπτυξη νανοσυνθετων επικαλύψεων με μήτρα Νικελίου και νανο-ZrO₂. Η μελέτη περιλαμβάνει μια περιεκτική έρευνα όπου αφορά την προετοιμασία 27 δειγμάτων καθένα από τα οποία σχεδιάστηκε με προσοχή για να περιλαμβάνει ένα ευρύ φάσμα πειραματικών συνθηκών. Σημαντική σε αυτή τη μελέτη είναι η χρήση της 2-βουτυν-1,4-διόλη ως κύριου λειαντικού (οργανικού πρόσθετου), σε συνδυασμό με την εφαρμογή και των δύο μεθοδολογιών παλμικού και συνεχούς ρεύματος, με σκοπό να διερευνηθούν οι διακριτές και ταυτόχρονες επιδράσεις τους στο σχηματισμό και τις ιδιότητες των επικαλύψεων.

Ο πειραματικός σχεδιασμός χαρακτηρίζεται από λεπτομερή έρευνα και ακρίβεια. Παράμετροι όπως ο pH, η πυκνότητα του ρεύματος, η ταχύτητα ανάδευσης και η θερμοκρασία ελέγχονται και διατηρούνται σε σταθερές τιμές καθ' όλη τη διάρκεια της μελέτης, εξασφαλίζοντας την αξιοπιστία και την επαναληψιμότητα των αποτελεσμάτων. Με την τήρηση αυστηρών πρωτοκόλλων πειραματικής διαδικασίας, η έρευνα αυτή στοχεύει στην παροχή ολοκληρωμένων εισηγήσεων σχετικά με τις αλληλεπιδράσεις των βασικών παραμέτρων της διαδικασίας και των επιπτώσεών τους στη μορφολογία, τη δομή και τις ιδιότητες των επικαλύψεων.

Οι δομικές και επιφανειακές ιδιότητες των επικαλύψεων χαρακτηρίζονται με τη χρήση αναλυτικών τεχνικών, συμπεριλαμβανομένης της σάρωσης ηλεκτρονικού μικροσκοπίου (SEM), της ενεργού αναλυτικής ακτινοβολίας X (EDS), της περίθλασης ακτινοβολίας X (XRD) και του καθορισμού της τραχύτητας της επιφάνειας. Αυτές οι τεχνικές παρέχουν μια λεπτομερή κατανόηση της μικροδομής, της φάσης και της επιφανειακής τοπογραφίας των επικαλύψεων, επιτρέποντας την ανάπτυξη συσχετίσεων μεταξύ των παραμέτρων της διαδικασίας και των παρατηρούμενων ιδιοτήτων του υλικού.

Εκτός από τον δομικό χαρακτηρισμό, οι μηχανικές ιδιότητες των επικαλύψεων αξιολογούνται μέσω μετρήσεων μικροσκληρότητας Vickers. Με την ποσοτικοποίηση της αντίδρασης των δειγμάτων στα εφαρμοζόμενα φορτία, αποκτούνται πολύτιμες πληροφορίες σχετικά με τη σκληρότητά τους, την αντοχή τους και την αντίστασή τους στην παραμόρφωση, καθορίζοντας έτσι πιθανές εφαρμογές σε διάφορα μηχανικά περιβάλλοντα.

Μέσω αυτής της προσέγγισης, η έρευνα αυτή επιδιώκει να προωθήσει τη βασική μας κατανόηση στη διαδικασία της ηλεκτρολυτικής απόθεσης και να ανοίξει το δρόμο για την ανάπτυξη εξατομικευμένων νανοςύνθετων επικαλύψεων μήτρας Νικελίου και νανο-ZrO₂ με βελτιωμένες ιδιότητες. Με την ενδελεχή εξέταση των πολύπλοκων σχέσεων μεταξύ των παραμέτρων του παλμικού ρεύματος, των οργανικών προσθέτων και των ιδιοτήτων της επικάλυψης, αυτή η μελέτη στοχεύει να συμβάλει στην ήδη παρούσα έρευνα που αφορά την επιστήμη και τεχνολογία των υλικών, ενισχύοντας την ανάπτυξη καινοτόμων λύσεων για ένα ευρύ φάσμα βιομηχανικών εφαρμογών.

Συνοψίζοντας, αυτή η διατριβή αποτελεί μια περιεκτική εξερεύνηση των συγχρονισμένων επιδράσεων των παραμέτρων του παλμικού ρεύματος και των οργανικών προσθέτων στην ηλεκτρολυτική απόθεση των εξατομικευμένων νανοσύνθετων επικαλύψεων μήτρας Νικελίου και νανο-ZrO₂. Μέσω της λεπτομερούς πειραματικής διαδικασίας, αυστηρής ανάλυσης και συστηματικού χαρακτηρισμού, αυτή η έρευνα στοχεύει στη διεύρυνση των συνόρων γνώσης στον τομέα της επιστήμης και τεχνολογίας υλικών και επιφανειών και στην προώθηση των εξελίξεων στην επιστήμη και την τεχνολογία των υλικών.

Introduction

Electroplating, an ancient technique documented since the 1950s, represents a finishing process applied to object surfaces (substrates) to enhance mechanical properties, adhesion, corrosion resistance, and other surface characteristics. Coatings play a significant role in protecting metal surfaces from corrosion, and various techniques have been developed to apply these coatings effectively. Coatings are often and easily applied to prevent metal corrosion. This technique has several variants such as electroplating, Physical Vapor Deposition (PVD), Chemical Vapor Deposition (CVD), laser beam deposition, and ion implantation. Of all the types of coating, electroplating is the most economical and its production rate is so high that this method fits the use in industry. When the material for coating or plating the object is nickel, the method is completely named 'nickel electroplating'.

Nickel electroplating not only enhances the aesthetic appeal of metal surfaces but also significantly improves their mechanical and chemical properties. Moreover, the advent of nanotechnology has enabled the production of nanocrystalline nickel deposits through electroplating, which exhibit lower porosity and superior mechanical properties. These nano-sized nickel grains contribute to increased corrosion resistance, strength, and improved tribological properties of the metal.

The electroplating process involves the deposition of an aqueous metallic species onto a negatively charged electrode (cathode) through electrolysis. This chemical transformation occurs as an electrical current passes through the conducting medium, the electrolyte. The positive ions migrate to the cathode, where they accept electrons and deposit as neutral atoms on the electrode surface. The anodic reaction, dependent on both the anode and surrounding electrolyte, may involve processes like oxygen evolution or dissolution of soluble anodes.

The application of electroplating extends beyond pure nickel deposition. It encompasses the codeposition of micron- or nanosized particles of metallic or non-metallic compounds and polymers with a metal or alloy matrix, resulting in composite coatings with tailored properties. Such composite deposits find applications across diverse sectors, ranging from high-tech industries like electronics to traditional sectors such as automotive, textiles, and food production.

Composite coatings offer great potential by combining properties from two different materials into a single coating. This allows for the creation of new surface properties that can be tailored and applied to any material's surface. Among different manufacturing methods, electrodeposition is particularly promising for producing composite metal matrix coatings, especially nanocomposites.

In the pursuit of wear- and corrosion-resistant coatings, self-lubricating systems, and dispersion-strengthened coatings, researchers have explored a wide range of particles for composite electrodeposition. These include hard oxides (e.g., ZrO_2 , SiO_2 , Al_2O_3 , TiO_2), carbides (e.g., WC , SiC), polymeric microcapsules, carbon nanotubes, among others. The integration of nanoparticles into composite coatings has garnered

significant attention due to their potential to enhance performance while maintaining low production costs and operating temperatures.

Furthermore, organic additives, such as 2-butyne-1,4-diol and saccharin, play a pivotal role in electroplating baths, serving various purposes such as leveling, grain refinement, and stress reduction. The continual evolution of electroplating techniques, particularly in the realm of metal matrix nanocomposites, offers unprecedented opportunities in transportation, electrical, and manufacturing sectors.

In summary, the integration of nickel electroplating and composite coating technologies represents a promising avenue for enhancing the corrosion resistance and mechanical properties of metal surfaces across diverse industrial applications. Through meticulous research and development, these techniques continue to evolve, offering innovative solutions to contemporary challenges in materials science and engineering.

Acknowledgements

I would like to express my sincere gratitude to:

My supervisor, to Assoc. Prof. Konstantina Kollia, for her continuous patience, dedication, support, constructive criticism, and guidance and care in developing my research abilities.

Dr Maria Myrto Dardavila, for her valuable comments and suggestions, meaningful scientific talks and assistance and her inherent desire and kindness to help and guide me.

Msc Athanasios Tzanis for his suggestions and assistance and his help with the SEM and EDS analysis.

The contribution of Dr Nick Panagiotou with the XRD measurements.

The contribution of Dr P. Gyftou with the Vickers Microhardness measurements.

All my friends and colleagues at the department of chemical engineering.

My Mother and Sisters, for their continues support and endless love and care.

School of chemical engineering
National and Technical university of Athens
Athens, 2024

Table of contents

Abstract.....	3
Περίληψη.....	5
Introduction.....	8
Acknowledgments.....	11

Part 1. Theoretical part

CHAPTER I: Crystalline Foundations: The structure of Metals

1. Structure and Properties of Metals.....	20
Introduction.....	20
1.1 Metallic solids.....	20
1.1.1 Properties of metals.....	20
1.2 Crystalline solids: Crystalline lattices.....	21
1.2.1 Crystalline lattices.....	21
1.2.2 Crystal structure of metals.....	23
1.2.3 Lattice planes and Miller indices.....	25
1.2.4 Determination of crystal structure by X-ray diffraction.....	26
1.3 Crystal defects.....	27
1.3.1 Point Defects: Vacancies and self-interstitial.....	28
1.3.2 Impurities in solids.....	28
1.3.3 Dislocations-Linear defects.....	29
1.3.4 Interfacial defects.....	30
1.4 Nickel.....	31
1.4.1 Physical and chemical properties.....	31
1.4.2 Uses of Nickel.....	32
1.4.3 Effects of Nickel on Human health.....	32
1.4.4 Nickel structure.....	32

CHAPTER II: Structure and properties of ceramics

2. Structure and properties of ceramics.....	35
Introduction.....	35
2.1 Crystal structure.....	35
2.2 Imperfections in ceramics.....	38
2.2.1 Atomic point defects.....	38
2.2.2 Impurities in ceramics.....	38

2.3	Zirconia.....	39
2.3.1	Cubic Zirconia.....	40
2.3.2	Tetragonal Zirconia.....	41
2.3.3	Monoclinic Zirconia.....	41
2.3.4	Nano-Zirconia.....	42

CHAPTER III: Fundamentals of composite Materials

3.	Composite materials.....	44
	Introduction.....	44
3.1	Characteristics.....	44
3.2	Types of composite materials.....	45
3.3	Particle-reinforced composites.....	47
3.4	Nano-composite materials.....	47

CHAPTER IV: A comprehensive Review in Electrolysis

4.	The process of electrolysis.....	49
	Introduction.....	49
4.1	Connection between chemistry and Electricity.....	50
4.2	Electroneutrality and Oxidation-Reduction Process.....	50
4.3	Electrical double layer.....	52
4.4	Potential differences at interfaces.....	54
4.5	Electrochemical cell.....	54
4.6	Faradaic and non-Faradaic current.....	56
4.7	The standard hydrogen electrode and reference electrodes.....	56
4.7.1	The calomel electrode.....	57
4.7.2	The Silver/Silver chloride electrode.....	58
4.8	Cell potential.....	58
4.9	The Laws of Electrolysis.....	59
4.10	Mass transfer in electrolytic cell.....	59
4.11	Energy losses in electrochemical cell.....	60
4.12	Ohmic voltage drop.....	61
4.12.1	Factors that influence ohmic potential drop.....	61
4.13	Polarization of electrodes.....	62

CHAPTER V: Electrolytic deposition (Electroplating) of Metals

	Introduction.....	63
5.	The process of electroplating.....	64
5.1	Fundamentals of electrodeposition.....	64

5.2	Deposition mechanism.....	66
5.3	Type of current.....	67
5.4	Additives.....	70
5.4.1	Brightener: 2-butyne-1,4-diol.....	70
5.5	Nickel Electrodeposition.....	71
5.5.1	Different types of Nickel electrolytic baths.....	71
5.5.2	Nickel electrodeposition mechanism.....	73
5.5.3	Current Efficiency.....	73
5.5.4	Nickel eclectic orientations.....	74
5.6	Composite and nano-composite coatings.....	76
5.7	Electrodeposition parameters.....	79
5.7.1	Effect of pH.....	79
5.7.2	Effect of Temperature.....	80
5.7.3	Effect of Stirring/Agitation rate.....	80
5.7.4	Effect of type of current.....	81
5.7.5	Effect of current density.....	82
5.7.6	Effect of surfactant.....	82
5.7.7	Effect of Electrolyte and incorporated particles.....	83
5.7.8	Effect of additives and brighteners.....	84
5.7.9	Effect of substrate.....	84

PART 2. Experimental part

CHAPTER VI: Experimental procedure: Production of Nickel-Matric nanocomposite coatings

6.	Nickel-Matrix nanocomposite coatings.....	86
	Introduction.....	86
6.1	Experimental Setup.....	87
6.2	Pre-treatment of samples.....	87
6.3	Produced coatings.....	87

CHAPTER VII: Characterization and Analysis Techniques

7.	Methods of characterization and analysis	
	Introduction.....	93
7.1	Scanning Electron Microscopy (SEM).....	94
7.2	Energy Dispersive X-ray Spectroscopy (EDS).....	95
7.3	X-ray Diffraction (XRD).....	96
7.4	Vickers Microhardness.....	98

7.5	Surface Roughness Tester.....	99
CHAPTER VIII: Experimental Results-Characterization of Coatings		
8.	Presentation of the experimental results.....	102
	Introduction.....	102
8.1	XRD analysis of composite and nano-composite coatings.....	102
8.2	SEM and EDS analysis of composite and nano-composite coatings.....	104
8.3	Vickers Microhardness.....	108
8.4	Roughness.....	117
PART 3. Conclusions and Future Work		
CHAPTER IX: Conclusions and Future Work		
9.1	Conclusions.....	126
9.1.1	The effect of the organic additive 2-butyne-1,4-diol.....	126
9.1.2	The effect of nano-ZrO ₂	126
9.1.3	Synergetic effect of 2-butyne-1,4-diol and nano-ZrO ₂ under Direct Current.....	127
9.1.4.	The effect of pulse current.....	130
9.2	General conclusions.....	130
9.3	Future work.....	130
References.....		132

THEORETICAL PART

CHAPTER I:
**Crystalline Foundations: The
structure of Metals**

1. Structure and properties of Metals

Introduction

Metals, with their intrinsic ability to seamlessly meld strength with versatility, constitute the cornerstone of humanity's technological progress. As the cornerstone of countless industrial applications, metals exhibit a remarkable interplay of atomic arrangements and mechanical behaviors that govern their performance in diverse environments. Understanding the structural characteristics and inherent properties of metals is pivotal for engineers, scientists, and researchers alike, as it lays the groundwork for innovations that push the boundaries of what is achievable in materials science.

1.1 Metallic solids

Metallic solids are a type of solids that are entirely comprised of atoms that are held together by metallic bonds. Metallic bonding is a type of intramolecular force of attraction that occurs between a lattice of positive ions and a "sea" of delocalized electrons. [1]. Typically, common metallic solids exist in the form of aggregates comprising crystals, exhibiting a varying scale of dimensions ranging from a few micrometers to several centimeters [2].

A metal crystal consists of two parts:

- positive ions
- free-flowing electrons that are also known as a "sea" of delocalized electrons [2].

In the "electron sea" model, atoms in a metallic solid lose their outer electrons and form a regular lattice of positive metallic ions. The outer electrons do not "belong" to any atom but form a sea of delocalized electrons that are free and move randomly throughout the fixed lattice of positive ions. According to the electron sea model, all metals conduct electricity well because the outer electrons are free to move through the lattice under the influence of an electric field. Metals are malleable and ductile because there are defects in the solid state or one layer of atoms can slide over another layer easily [3].

1.1.1 Properties of metals.

The properties of metals are a result of the arrangement and characteristics of their constituent atoms, with the way in which the atoms are arranged playing a crucial role in this correlation. Properties such as rigidity, electrical conductivity and optical, magnetic and chemical properties derive from the properties of atoms [4].

For instance, the melting point of a solid is a crucial property. For a solid to undergo melting, the forces holding its constituent units in place must be partially overcome. Metals generally exhibit high melting points, although there can be variations. Another crucial property is hardness, which depends on the ease with which the

structural units of a solid can move relative to each other, and consequently, on the strength of the attractive forces between the units. [1].

1.2 Crystalline Solids: Crystalline lattices

Solids can exist in two fundamental forms: crystalline or amorphous. A crystalline solid is characterized by the presence of one or more crystals, each exhibiting a meticulously ordered structure. In metals, for instance, the solid state typically manifests as cohesive masses composed of individual crystals. These crystals align in a specific pattern, imparting distinctive properties to the material. On the other hand, an amorphous solid lacks the well-defined structure observed in crystalline counterparts. Its arrangement of structural units is disorderly and lacks the repeating, organized patterns found in crystals [1].

1.2.1 Crystalline lattices

A crystal is a three-dimensional assembled arrangement of structural units (a structural unit can be an atom, molecule, or ion, depending on the type of crystal). The ordered structure of a crystal is conventionally described in terms of a crystal plane—an abstract framework that represents the crystal's structure. More precisely, a crystal lattice is a three-dimensional, infinite arrangement of points, each surrounded by its neighbors in an identical manner. This arrangement defines the basic structure of the crystal. The crystal structure itself is determined by assigning an identical structural pattern to each lattice point [1], [4].

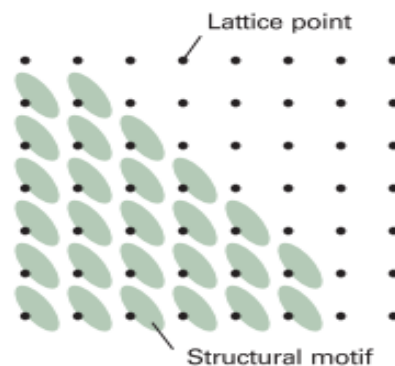


Figure 1: Each lattice point specifies the location of a structural motif (for example, a molecule or a group of molecules). The crystal lattice is the array of lattice points; the crystal structure is the collection of structural motifs arranged according to the lattice [4].

The unit cell of a crystal is the smallest three-dimensional unit that, when replicated, forms the entire crystal [1].

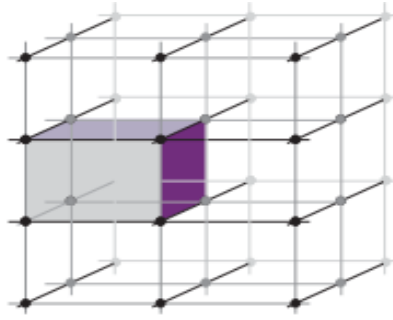


Figure 2: A unit cell is a parallel-sided (but not necessarily rectangular) figure from which the entire crystal structure can be constructed by using only translations (not reflections, rotations, or inversions) [4].

The lengths of the sides of a unit cell are denoted by the letters a , b , and c , while the angles between them are represented by α , β , and γ (**Figure 3**). Unit cells are classified into seven crystal systems by noting the rotational symmetry elements they possess [4].

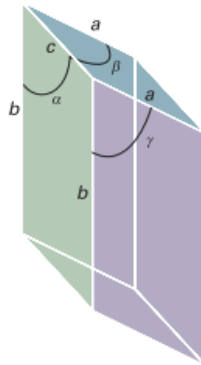


Figure 3: The notation for the sides and angles of a unit cell. Note that the angle α lies in the plane (b , c) and perpendicular to the axis a [4].

There are seven basic shapes for unit cells, and from these shapes, seven crystal systems are derived, forming the basis for classifying crystals. A crystal belonging to a specific crystal system possesses a unit cell with one of these seven shapes. Each unit cell shape is defined by the angles of its edges and the relative lengths of those edges [1]. A cubic unit cell, for example, has four threefold axes in a tetrahedral array. A monoclinic unit cell has one twofold axis, the unique axis is by convention the b axis. A triclinic unit cell has no rotational symmetry, and typically all three sides and angles are different [4].

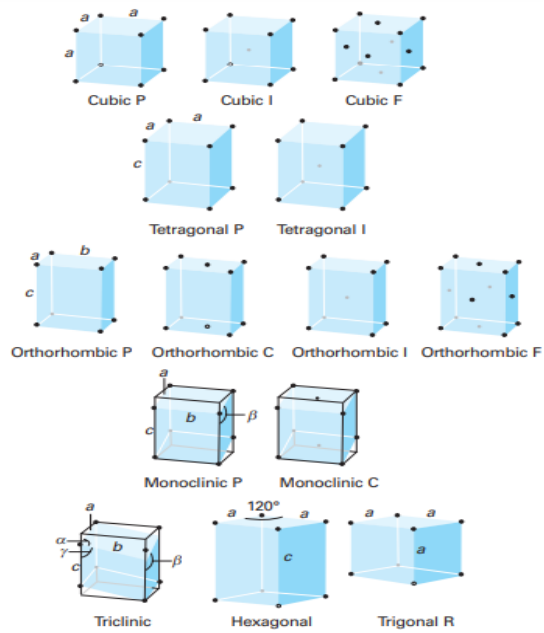


Figure 4: The fourteen Bravais lattices. The points are lattice points, and are not necessarily occupied by atoms. P denotes a primitive unit cell (R is used for a trigonal lattice), I a bodycentred unit cell, F a face-centred unit cell, and C (or A or B) a cell with lattice points on two opposite face [4]

There are only 14 distinct space lattices in three dimensions, as illustrated in Fig. 4. These Bravais lattices are conventionally represented using primitive unit cells in some cases and non-primitive unit cells in others. [4].

1.2.2 Crystal structure of metals

Assuming that the metallic bond is not directionless, the maximum attraction occurs when each atom is surrounded by the largest possible number of other atoms.

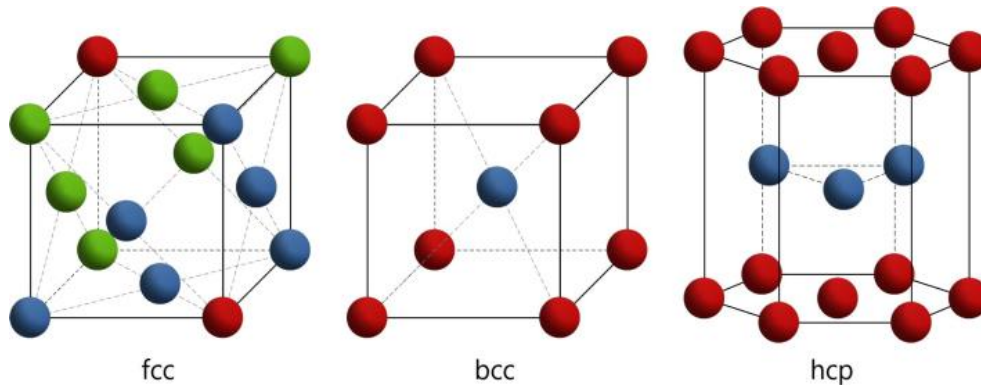


Figure 5: Crystal structure of metals

Therefore, it is expected that metals crystallize in one of the densely packed structures:

- **Body-Centered Cubic (BCC):** In a body-centered cubic structure, atoms are located at the corners and in the center of the cube. This results in a higher packing efficiency compared to simple cubic structures. In BCC, each atom is in contact with eight neighboring atoms.

- Cubic Close-Packed (CCP): Also known as face-centered cubic (FCC) or cubic closest packing, this structure has a stacking sequence of ABCABC... Each layer is a face-centered cubic lattice, and the layers are packed efficiently. Metals like copper and gold have CCP crystal structures. In a face-centered cubic structure, atoms are located at the corners and in the center of each face of the cube. This arrangement has the highest packing efficiency among the cubic structures. In FCC, each atom is in contact with twelve neighboring atoms.

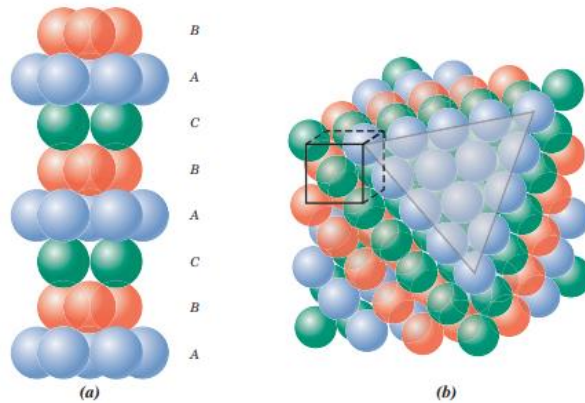


Figure 6: . (a) Close-packed stacking sequence for the face-centered cubic structure. (b) A corner has been removed to show the relation between the stacking of close-packed planes of atoms and the FCC crystal structure, the heavy triangle outlines a (111) plane [5].

- Hexagonal Close-Packed (HCP): In an HCP structure, the atoms are arranged in layers with an ABAB... stacking sequence. Each layer is a hexagonal lattice, and the layers are packed in a way that results in efficient packing. Metals like magnesium and zinc adopt HCP structures. In HCP, each atom is in contact with eight neighboring atoms.

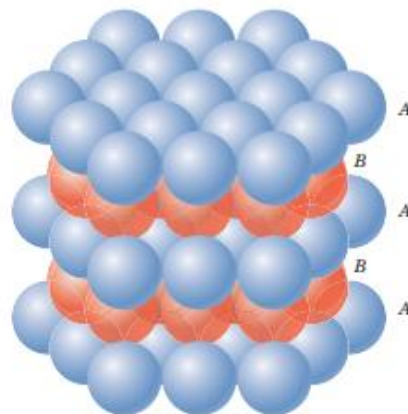


Figure 7: . Close-packed plane stacking sequence for the hexagonal close-packed structure [5].

<i>Metal</i>	<i>Crystal Structure^a</i>	<i>Atomic Radius^b (nm)</i>	<i>Metal</i>	<i>Crystal Structure</i>	<i>Atomic Radius (nm)</i>
Aluminum	FCC	0.1431	Molybdenum	BCC	0.1363
Cadmium	HCP	0.1490	Nickel	FCC	0.1246
Chromium	BCC	0.1249	Platinum	FCC	0.1387
Cobalt	HCP	0.1253	Silver	FCC	0.1445
Copper	FCC	0.1278	Tantalum	BCC	0.1430
Gold	FCC	0.1442	Titanium (α)	HCP	0.1445
Iron (α)	BCC	0.1241	Tungsten	BCC	0.1371
Lead	FCC	0.1750	Zinc	HCP	0.1332

Table 1: Atomic Radius and Crystal Structures for 16 Metals [5].

1.2.3 Lattice planes and Miller indices

In a Bravais lattice, a lattice plane is any two-dimensional plane that contains at least three non-linear Bravais points. These lattice planes play a crucial role in understanding the geometric arrangement of atoms or points in the lattice structure. Due to the translational symmetry of the Bravais lattice, each lattice plane will include an unbounded number of lattice points, forming a two-dimensional Bravais lattice [6].

The lattice plane serves as a fundamental unit for analyzing the crystallographic properties of materials. It provides insights into the periodic arrangement of atoms or particles within the crystal lattice.

The distance between the planes of the lattice points in a crystal is an important quantitative parameter of its structure [4].

The crystal levels are determined by a set of Miller indices. Miller indices are very useful for expressing the separation of planes [4].

Miller indices are a set of three integers that represent the orientation of a crystal plane or direction in a crystal lattice. These indices were introduced by British mineralogist and crystallographer William H. Miller in the 19th century. Miller indices are widely used in crystallography and materials science to describe the orientation of planes and directions within crystals.

In theory, the procedure for identifying the Miller indices of a crystallographic plane can be described as follows.

1. Identify the points at which the crystallographic plane intercepts the x, y and z coordinates in terms of the number of lattice parameters. Notably, the coordinate origin cannot be located on the above crystal facet. If the crystallographic plane passes through the coordinate origin, the origin of the coordinate system must be redefined.
2. Take reciprocals of the three intercepts, respectively.
3. Clear fractions but do not reduce to lowest integers, which are denoted as $h : k : l$.
4. Enclose the resulting number in parentheses (hkl).

Again, a negative number should be written with a bar over the number, which means the corresponding intercept is negative. In particular, if the crystal facet is parallel to the coordinate axis, the corresponding number in (hkl) will be zero. In each unit cell, planes of a form represent groups of equivalent planes that have their particular indices because of the orientation of the coordinates.⁴² These groups of similar planes can be represented by {hkl}, namely, the crystal facets possess the same arrangement of atoms but nonparallel spatial orientations, which is different with (hkl). For example, the planes of the form {100} in a cubic system include (100), (010) and (001) [7].

The separation of the {hkl} planes of a cubic lattice is given by [4]:

$$\frac{1}{d_{hkl}^2} = \frac{h^2 + k^2 + l^2}{a^2} \quad (1)$$

The corresponding expression for a general orthorhombic lattice is the generalization of this expression:

$$\frac{1}{d_{hkl}^2} = \frac{h^2}{a^2} + \frac{k^2}{b^2} + \frac{l^2}{c^2} \quad (2)$$

1.2.4 Determination of crystal structures by x-ray diffraction

In 1913, W. H. and W. L. Bragg observed that materials with a macroscopic crystalline form produced characteristic images when subjected to reflected X-rays, distinct from the images generated by liquids. In crystalline materials, for a given wavelength and direction of X-ray incidence, sharp peaks were observed in specific directions, now known as Bragg peaks [6].

W. L. Bragg calculated these peaks by assuming that the crystal consists of parallel planes of ions separated by a distance d . The conditions for a narrow peak in scattered radiation were twofold: first, the X-rays must be mirror-reflected by the ions in each plane, and second, the reflected rays from successive planes must contribute amplifyingly [6].

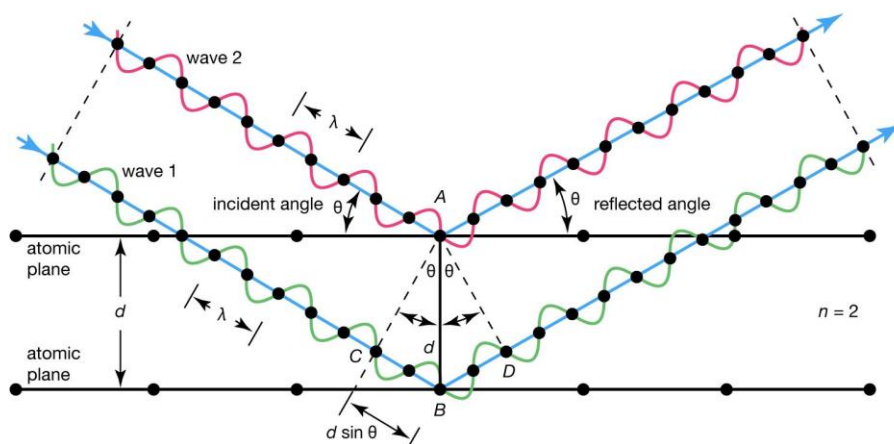


Figure 8: Bragg diffraction [8].

The general relationship between the wavelength of the incident X-rays, angle of incidence and spacing between the crystal lattice planes of atoms is known as Bragg's Law, expressed as:

$$n \lambda = 2d \sin\Theta \quad (3)$$

where n (an integer) is the "order" of reflection, λ is the wavelength of the incident X-rays, d is the interplanar spacing of the crystal and Θ is the angle of incidence [6].

Bragg's law, Equation 3, is a necessary but not sufficient condition for diffraction by real crystals. It specifies when diffraction will occur for unit cells having atoms positioned only at cell corners. However, atoms situated at other sites (e.g., face and interior unit cell positions as with FCC and BCC) act as extra scattering centers, which can produce out-of-phase scattering at certain Bragg angles. The net result is the absence of some diffracted beams that, according to Equation 3, should be present. Specific sets of crystallographic planes that do not give rise to diffracted beams depend on crystal structure. For the BCC crystal structure, $h + k + l$ must be even if diffraction is to occur, whereas for FCC, h , k , and l must all be either odd or even; diffracted beams for all sets of crystallographic planes are present for the simple cubic crystal structure. These restrictions, called reflection rules, are summarized in

<i>Crystal Structure</i>	<i>Reflections Present</i>	<i>Reflection Indices for First Six Planes</i>
BCC	$(h + k + l)$ even	110, 200, 211, 220, 310, 222
FCC	h , k , and l either all odd or all even	111, 200, 220, 311, 222, 400
Simple cubic	All	100, 110, 111, 200, 210, 211

Table 2 [5].

<i>Crystal Structure</i>	<i>Reflections Present</i>	<i>Reflection Indices for First Six Planes</i>
BCC	$(h + k + l)$ even	110, 200, 211, 220, 310, 222
FCC	h , k , and l either all odd or all even	111, 200, 220, 311, 222, 400
Simple cubic	All	100, 110, 111, 200, 210, 211

Table 2: X-Ray Diffraction Reflection Rules and Reflection Indices for Body-Centered Cubic, Face-Centered Cubic, and Simple Cubic Crystal Structures [5].

1.3 Crystal defects

In reality, crystals are not characterized by perfect order. They have various defects.

The crystal defects can be divided into the following groups, according to their dimensional nature:

- a. Point defects: Vacancies, interstitial atoms, impurity atoms, and combinations of these.
- b. Line defects: i.e., dislocations.
- c. Two-dimensional defects: stacking faults, grain boundaries, etc.

- d. Three-dimensional defects: precipitates, inclusions, holes, etc [9].

Crystal defects can influence the strength and ductility of metals. For example, dislocations (line defects) can move through the crystal lattice, affecting the metal's ability to deform under stress. Vacancies and interstitial atoms, can hinder the movement of dislocations, making it more difficult for atoms to slide past one another. This can increase the hardness of the metal. Grain boundaries, which are planar defects, can act as sites for corrosion initiation. The presence of defects can create an environment where corrosion is more likely to occur.

1.3.1. Point Defects: Vacancies and self-interstitial

The simplest of the point defects is a vacancy, or vacant lattice site, one normally occupied but from which an atom is missing. All crystalline solids contain vacancies, and, in fact, it is not possible to create such a material that is free of these defects. The necessity of the existence of vacancies is explained using principles of thermodynamics; in essence, the presence of vacancies increases the entropy (i.e., the randomness) of the crystal [5].

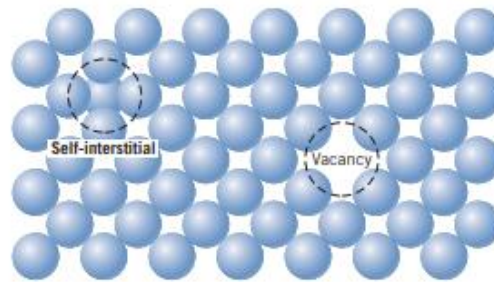


Figure 9: Two-dimensional representations of a vacancy and a self-interstitial [5].

A self-interstitial is an atom from the crystal that is crowded into an interstitial site—a small void space that under ordinary circumstances is not occupied.

1.3.2 Impurities in solids

A pure metal consisting of only one type of atom just isn't possible, impurity or foreign atoms are always present, and some exist as crystalline point defects. In fact, even with relatively sophisticated techniques, it is difficult to refine metals to a purity in excess of 99.9999%. At this level, on the order of 10^{22} to 10^{23} impurity atoms are present in 1 m³ of material. Most familiar metals are not highly pure, rather, they are alloys, in which impurity atoms have been added intentionally to impart specific characteristics to the material. Ordinarily, alloying is used in metals to improve mechanical strength and corrosion resistance. For example, sterling silver is a 92.5% silver–7.5% copper alloy. In normal ambient environments, pure silver is highly corrosion resistant, but also very soft. Alloying with copper significantly enhances the mechanical strength without reducing the corrosion resistance appreciably. The addition of impurity atoms to a metal results in the formation of a solid solution and/or a new second phase, depending on the kinds of impurity, their concentrations, and the temperature of the alloy [5].

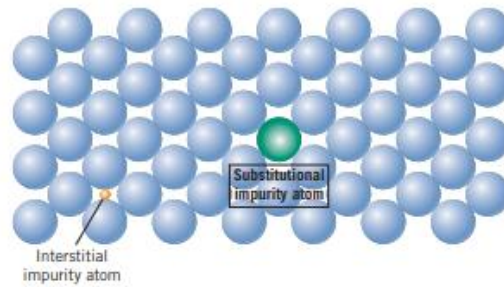


Figure 10: Two-dimensional schematic representations of substitutional and interstitial impurity atoms [5].

1.3.3 Dislocations- Linear defects

A dislocation is a linear or one-dimensional defect around which some of the atoms are misaligned. One type of dislocation is represented in Fig11: an extra portion of a plane of atoms, or half-plane, the edge of which terminates within the crystal. This is termed an edge dislocation, it is a linear defect that centers on the line that is defined along the end of the extra half-plane of atoms. This is sometimes termed the dislocation line, which, for the edge dislocation in Figure 11, is perpendicular to the plane of the page. Within the region around the dislocation line there is some localized lattice distortion. The atoms above the dislocation line in Figure 11 are squeezed together, and those below are pulled apart; this is reflected in the slight curvature for the vertical planes of atoms as they bend around this extra half-plane. The magnitude of this distortion decreases with distance away from the dislocation line; at positions far removed, the crystal lattice is virtually perfect. Sometimes the edge dislocation in Figure 11 is represented by the symbol \perp , which also indicates the position of the dislocation line. An edge dislocation may also be formed by an extra halfplane of atoms that is included in the bottom portion of the crystal; its designation is a \top [5].

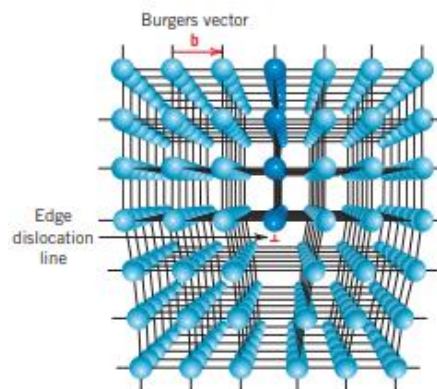


Figure 11: The atom positions around an edge dislocation; extra half-plane of atoms shown in perspective [5].

Another type of dislocation, called a screw dislocation, may be thought of as being formed by a shear stress that is applied to produce the distortion shown in Figure 12a:

The upper front region of the crystal is shifted one atomic distance to the right relative to the bottom portion. The atomic distortion associated with a screw dislocation is also linear and along a dislocation line, line AB in Figure 12b. The screw dislocation derives its name from the spiral or helical path or ramp that is traced around the dislocation line by the atomic planes of atoms. Sometimes the symbol \circlearrowright is used to designate a screw dislocation [5].

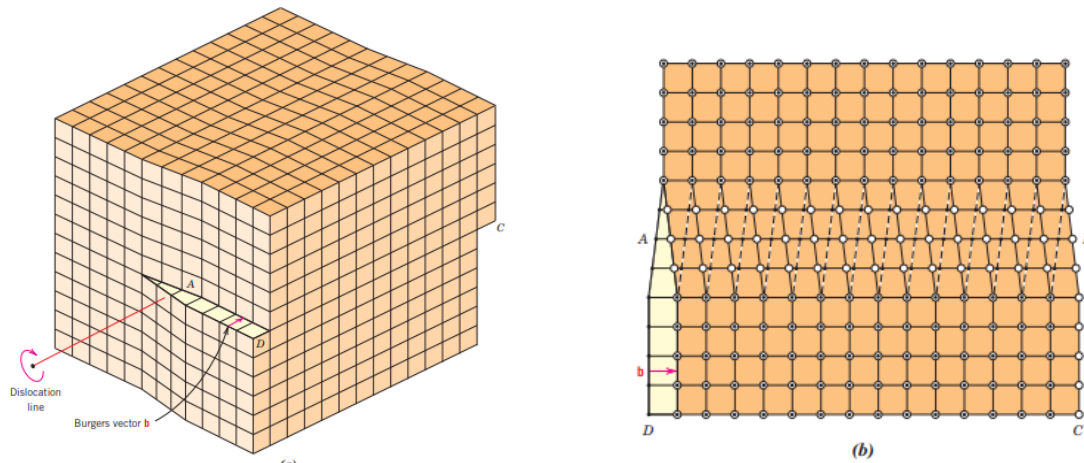


Figure 12: a) A screw dislocation within a crystal, b) The screw dislocation in (a) as viewed from above [5].

1.3.4 Interfacial defects

- **External Surfaces:**
One of the most obvious boundaries is the external surface, along which the crystal structure terminates. Surface atoms are not bonded to the maximum number of nearest neighbors and are therefore in a higher energy state than the atoms at interior positions. The bonds of these surface atoms that are not satisfied give rise to a surface energy, expressed in units of energy per unit area (J/m^2 or erg/cm^2). To reduce this energy, materials tend to minimize, if at all possible, the total surface area. For example, liquids assume a shape having a minimum area—the droplets become spherical. Of course, this is not possible with solids, which are mechanically rigid.
- **Grain Boundaries:**
Another interfacial defect, the grain boundary, is the boundary separating two small grains or crystals having different crystallographic orientations in polycrystalline materials. Within the boundary region, which is probably just several atom distances wide, there is some atomic mismatch in a transition from the crystalline orientation of one grain to that of an adjacent one.
- **Phase Boundaries:**
Phase boundaries exist in multiphase materials, in which a different phase exists on each side of the boundary. In addition, each of the constituent phases has its own distinctive physical and/or chemical characteristics. Phase boundaries play an important role in determining the mechanical characteristics of some multiphase metal alloys.
- **Twin Boundaries:**

A twin boundary is a special type of grain boundary across which there is a specific mirror lattice symmetry, that is, atoms on one side of the boundary are located in mirror-image positions to those of the atoms on the other side. The region of material between these boundaries is appropriately termed a twin. Twins result from atomic displacements that are produced from applied mechanical shear forces (mechanical twins) and also during annealing heat treatments following deformation (annealing twins). Twinning occurs on a definite crystallographic plane and in a specific direction, both of which depend on the crystal structure. Annealing twins are typically found in metals that have the FCC crystal structure, whereas mechanical twins are observed in BCC and HCP metals [5].

1.4 Nickel

Nickel is a ubiquitous metal that has been used by man since antiquity as a natural alloy for weapons. Several hundred years after the birth of Christ, Chinese craftsmen incorporated a nickel alloy, called white copper, into household objects and art. By the 17th century, an inexpensive, nickel-zinc-copper alloy from China appeared in Europe. The Swedish chemist A. F. Cronstedt recognized nickel as the 28th element of the periodic table in 1754 by separating an impure form of nickel from niccolite (NiAs). In 1820, Berthier isolated nickel as a pure metal [10].

Full-scale commercial production of nickel began only in the last 100 years, since J. F. Wharton produced malleable nickel that first appeared in a US 3-cent piece in 1865. In the 1890s, L. F. Mond discovered nickel carbonyl ($\text{Ni}[\text{CO}]_4$) and inaugurated the Mond carbonyl process to separate nickel from its ore. Although nickel carbonyl was always recognized as a highly toxic compound, nickel sulfate was recommended as a medicinal agent for the treatment of chorea, epilepsy, migraine, and neuralgia in the early 20th century. The medicinal use of nickel was abandoned in the 1930s, but studies at that time suggested that nickel was an essential element for metabolism in animals [10].

1.4.1. Physical and chemical properties

Nickel is a silver-white metal that forms the first transition series group VIIIb of the periodic table along with cobalt and iron, and has an atom. wt. of 58.71, specific gravity of 8.9, and melting pt. of 1453 °C. Nickel possesses relatively high thermal and electrical conductivity as well as ferromagnetic properties; however, the conductive and magnetic properties are less than silver and iron, respectively. The siderophilic properties of nickel facilitate the formation of nickel-iron alloys. As a member of the transition metal series, nickel is resistant to corrosion by air, water, and alkali, but nickel dissolves readily in dilute oxidizing acids. Nickel salts of strong acids and organic acids are soluble in water whereas nickel salts of weak inorganic acids are insoluble in water. In contrast to the soluble nickel salts (chloride, nitrate, sulfate), metallic nickel, nickel sulfides, and nickel oxides are poorly soluble in water. Nickel carbonates and nickel hydroxides are moderately soluble in water [10].

1.4.2 Uses of Nickel

Most Ni is used in alloys that are strong and corrosion resistant such as stainless steel. Stainless steel production is the single largest application of Ni and has been the most rapidly growing use in recent years. Thus, Ni is found in a wide variety of commodities such as automobiles, batteries, coins, jewelry, surgical implants, kitchen appliances, and sinks and utensils. Nickel is also used in Ni-Fe (used for magnetic components in electrical equipment), Ni-Cu (noted for resistance to corrosion especially in marine applications), Ni-Cr (used in heating elements for stoves and furnaces), and in Ni-Ag (used as a base for electroplated articles) alloys. Nickel-steel alloys are crucial in armor plating and in armaments. Other high-Ni alloys are used for such high technology applications as turbine blades, jet engine components, and in nuclear reactors [11].

1.4.3 Effects of Nickel on Human Health.

No toxicological incidents from Ni and its salts been recorded in the early 1900s. In fact, Ni salts had some medicinal value for the treatment of epilepsy, chorea, migraine, and neuralgia. Nickel was also used as a sedative and tonic of peculiar and elective power in controlling the damaging effects of sexual vice on the nervous system. However, since World War II, the use of Ni for medicinal purposes has been completely abandoned and it has been widely recognized that in addition to nickel carbonyl $[\text{Ni}(\text{CO})_4]$, exposure to Ni and other Ni compounds may adversely affect human health. The physiological response in humans to Ni depends on the following factors: physicochemical characteristics of the Ni compound, the concentration, the length and type of exposure, and the sensitivity and well-being of the exposed individual. In addition, the route of exposure and the target tissue are important. Individuals may be exposed to Ni in the workplace or through contact with everyday items such as Ni-containing jewelry, cooking utensils, stainless steel kitchens, and clothing fasteners. Contact dermatitis, consisting of itching of the fingers, wrists, and forearms, is the most common effect in humans from chronic (long-term) Ni exposure. Respiratory effects, such as asthma and an increased risk of chronic respiratory infections, have also been reported in humans from inhalation exposure to Ni [11].

1.4.4. Nickel Structure

Nickel exhibits a face-centered cubic (FCC) crystal structure at room temperature. In this arrangement, the nickel atoms are positioned at the corners and centers of each face of a cube. The FCC structure is characterized by a high degree of symmetry and close-packed atomic arrangement. The FCC crystal structure contributes to some of the physical properties of nickel, such as its high melting point, good thermal and electrical conductivity, and ductility. The electronic configuration for the Ni atom is $(\text{Ar})(3d)^{10}(4s)^2$, and the atomic radius is 0.124 nm.

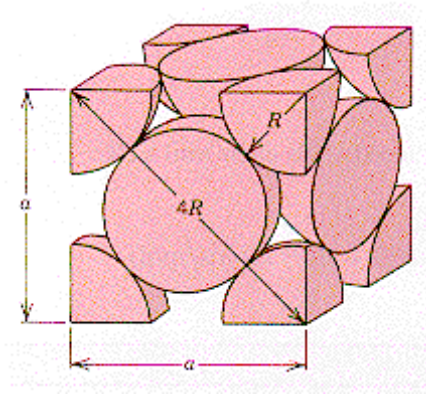


Figure 13: Crystal structure of Nickel [5].

CHAPTER II:
Structure and properties of
Ceramics

2. Structure and Properties of Ceramics

Introduction

Ceramic materials are inorganic and nonmetallic compounds, typically formed through the combination of metallic and nonmetallic elements. The interatomic bonds in ceramics are predominantly ionic, with some covalent character. The term "ceramic" is derived from the Greek word "keramikos," meaning "burnt stuff," reflecting the common practice of achieving desirable properties through high-temperature heat treatment, known as firing. In the past 60 years or so, there has been significant progress in understanding the fundamental nature of ceramic materials and the underlying phenomena responsible for their unique properties. Traditionally, ceramics referred to materials like china, porcelain, bricks, tiles, glasses, and high-temperature ceramics, with clay as a primary raw material. However, advancements have led to a broader definition of ceramics [5]. The evolving generation of ceramic materials has had a profound impact on various industries, including electronics, computers, communication, aerospace, and more. These materials play a crucial role in modern technology and have become integral components in diverse applications that shape our daily lives.

2.1 Crystal structure

For those ceramic materials for which the atomic bonding is predominantly ionic, the crystal structures may be thought of as being composed of electrically charged ions instead of atoms. The metallic ions, or cations, are positively charged because they have given up their valence electrons to the nonmetallic ions, or anions, which are negatively charged. Two characteristics of the component ions in crystalline ceramic materials influence the crystal structure: the magnitude of the electrical charge on each of the component ions, and the relative sizes of the cations and anions. With regard to the first characteristic, the crystal must be electrically neutral; that is, all the cation positive charges must be balanced by an equal number of anion negative charges. The chemical formula of a compound indicates the ratio of cations to anions, or the composition that achieves this charge balance. For example, in calcium fluoride, each calcium ion has a +2 charge (Ca^{2+}), and associated with each fluorine ion is a single negative charge (F^-). Thus, there must be twice as many F^- as Ca^{2+} ions, which is reflected in the chemical formula CaF_2 .

The second criterion involves the sizes or ionic radii of the cations and anions, r_C and r_A , respectively. Because the metallic elements give up electrons when ionized, cations are ordinarily smaller than anions, and, consequently, the ratio r_C/r_A is less than unity. Each cation prefers to have as many nearest-neighbor anions as possible. The anions also desire a maximum number of cations nearest neighbors.

Stable ceramic crystal structures form when those anions surrounding a cation are all in contact with that cation. The coordination number (i.e., number of anions nearest neighbors for a cation) is related to the cation–anion radius ratio. For a specific coordination number, there is a critical or minimum r_C/r_A ratio for which

this cation–anion contact is established, this ratio may be determined from pure geometrical considerations [5].

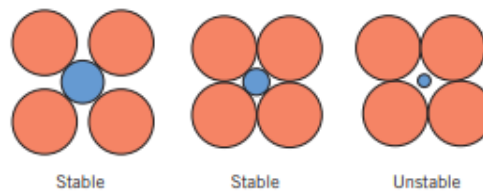


Figure 14: Stable and unstable cation–anion coordination configurations. Red circles represent anions, blue circles denote cations [5].

- **AX-Type Crystal Structures**

Some of the common ceramic materials are those in which there are equal numbers of cations and anions. These are often referred to as AX compounds, where A denotes the cation and X the anion. There are several different crystal structures for AX compounds, each is typically named after a common material that assumes the particular structure.

Perhaps the most common AX crystal structure is the sodium chloride (NaCl), or rock salt, type. The coordination number for both cations and anions is 6, and therefore the cation–anion radius ratio is between approximately 0.414 and 0.732. A unit cell for this crystal structure is generated from an FCC arrangement of anions with one cation situated at the cube center and one at the center of each of the 12 cube edges. An equivalent crystal structure results from a face-centered arrangement of cations. Thus, the rock salt crystal structure may be thought of as two interpenetrating FCC lattices—one composed of the cations, the other of anions. Some common ceramic materials that form with this crystal structure are NaCl, MgO, MnS, LiF, and FeO.

The second AX type is Cesium Chloride Structure. The coordination number is 8 for both ion types. The anions are located at each of the corners of a cube, whereas the cube center is a single cation. Interchange of anions with cations, and vice versa, produces the same crystal structure. This is not a BCC crystal structure because ions of two different kinds are involved.

A third AX structure is one in which the coordination number is 4—that is, all ions are tetrahedrally coordinated. This is called the zinc blende, or sphalerite, structure, after the mineralogical term for zinc sulfide (ZnS). All corner and face positions of the cubic cell are occupied by S atoms, whereas the Zn atoms fill interior tetrahedral positions. An equivalent structure results if Zn and S atom positions are reversed. Thus, each Zn atom is bonded to four S atoms, and vice versa. Most often the atomic bonding is highly covalent in compounds exhibiting this crystal structure, which include ZnS, ZnTe, and SiC.

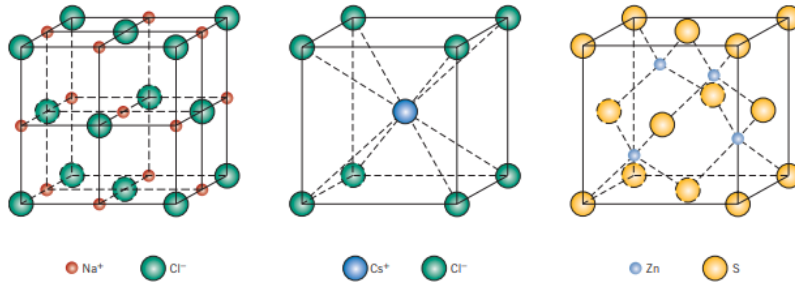


Figure 15: Unit Cells of NaCl(left), CsCl(middle), ZnS(right) [5].

Some ceramics have a covalent network crystal structure, where each atom is bonded to its neighboring atoms by strong covalent bonds. Diamond, a form of carbon, is an example of a covalent network crystal. Diamond is a metastable carbon polymorph at room temperature and atmospheric pressure. Its crystal structure is a variant of the zinc blende structure (

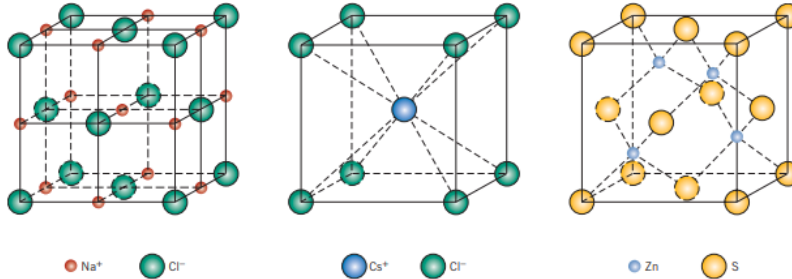


Figure 15: Unit Cells of NaCl(left), CsCl(middle), ZnS(right).) in which carbon atoms occupy all positions (both Zn and S).

The unit cell for diamond is shown in Figure 16. Each carbon atom has undergone sp^3 hybridization so that it bonds (tetrahedrally) to four other carbons. The crystal structure of diamond is appropriately called the diamond cubic crystal structure, which is also found for other Group IVA elements in the periodic table.

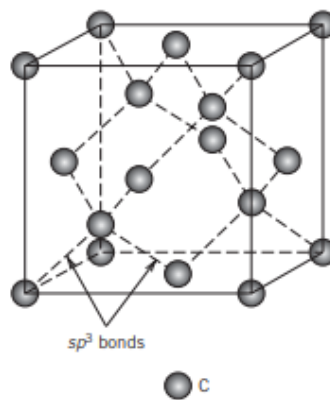


Figure 16:A unit cell for the diamond cubic crystal structure [5].

- A_mX_p -Type Crystal Structures

If the charges on the cations and anions are not the same, a compound can exist with the chemical formula A_mX_p , where m and/or $p \neq 1$. An example is AX_2 , for which a common crystal structure is found in fluorite (CaF_2). The ionic radii ratio r_C/r_A for CaF_2 is about 0.8, which gives a coordination number of 8. Calcium ions are positioned at the centers of cubes, with fluorine ions at the corners. The chemical formula shows that there are only half as many Ca^{2+} ions as F^- ions, and therefore the crystal structure is similar to $CsCl$, except that only half the center cube positions are occupied by Ca^{2+} ions. One unit cell consists of eight cubes. Other compounds with this crystal structure include ZrO_2 (cubic), UO_2 , PuO_2 , and ThO_2 .

- **$A_mB_nX_p$ -Type Crystal Structures**

It is also possible for ceramic compounds to have more than one type of cation; for two types of cations (represented by A and B), their chemical formula may be designated as $A_mB_nX_p$. Barium titanate ($BaTiO_3$), having both Ba^{2+} and Ti^{4+} cations, falls into this classification. This material has a perovskite crystal structure. At temperatures above $120^\circ C$ ($248^\circ F$), the crystal structure is cubic.

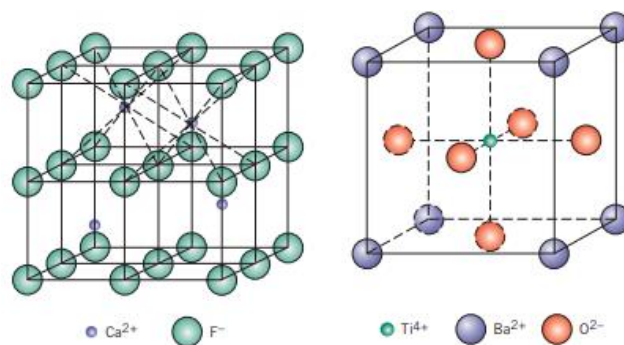


Figure 17: Unit Cells of CaF_2 (left), perovskite(right)

It may be recalled that for metals, close-packed planes of atoms stacked on one another generate both FCC and HCP crystal structures. Similarly, a number of ceramic crystal structures may be considered in terms of close-packed planes of ions, as well as unit cells. Ordinarily, the close-packed planes are composed of the large anions. Hexagonal crystal structures are observed in some ceramic materials, where atoms are arranged in a hexagonal lattice. For example, aluminum oxide (Al_2O_3) often has a hexagonal crystal structure.

2.2. Imperfections in Ceramics

2.2.1 Atomic point defects

Atomic defects involving host atoms may exist in ceramic compounds. As with metals, both vacancies and interstitials are possible, however, because ceramic materials contain ions of at least two kinds, defects for each ion type may occur.

For example, in NaCl, Na interstitials and vacancies and Cl interstitials and vacancies may exist.

2.2.2 Impurities in Ceramics

Impurity atoms can form solid solutions in ceramic materials much as they do in metals. Solid solutions of both substitutional and interstitial types are possible. For an interstitial, the ionic radius of the impurity must be relatively small in comparison to the anion. Because there are both anions and cations, a substitutional impurity substitutes for the host ion to which it is most similar in an electrical sense: If the impurity atom normally forms a cation in a ceramic material, it most probably will substitute for a host cation. For example, in sodium chloride, impurity Ca^{2+} and O^{2-} ions would most likely substitute for Na^+ and Cl^- ions, respectively. Schematic representations for cation and anion substitutional as well as interstitial impurities are shown in Figure 17. To achieve any appreciable solid solubility of substituting impurity atoms, the ionic size and charge must be very nearly the same as those of one of the host ions. For an impurity ion having a charge different from that of the host ion for which it substitutes, the crystal must compensate for this difference in charge so that electroneutrality is maintained with the solid. One way this is accomplished is by the formation of lattice defects vacancies or interstitials of both ion type.

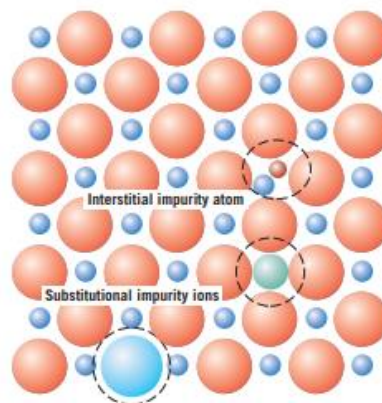


Figure 18: Schematic representations of interstitial, anion-substitutional, and cation substitutional impurity atoms in an ionic compound [5].

2.3. Zirconia

Zirconium (Zr) is a metal with the atomic number 40. It was first discovered in 1789 by the chemist Martin Klaproth. The material has a density of 6.49 g/cm^3 , a melting point of $1852 \text{ }^\circ\text{C}$ and a boiling point of $3580 \text{ }^\circ\text{C}$. It has a hexagonal crystal structure and is grayish in color. Zr does not occur in nature in a pure state. It can be found in conjunction with silicate oxide with the mineral name Zircon ($\text{ZrO}_2 \cdot x \text{SiO}_2$) or as a free oxide (Zirconia, ZrO_2) with the mineral name Baddeleyite [12]. Zirconium compounds are widespread in the lithosphere. According to various Clarke numbers (numbers expressing the average content of chemical elements in the earth's crust, hydrosphere, Earth, cosmic bodies, geochemical or cosmochemical systems, etc., in

relation to the total mass of this system), zirconium content ranges from 170 to 250 g/t. Concentration in seawater is $5 \cdot 10^{-5}$ mg/l. Zirconium is a lithophilic element. In nature, there are only its compounds with oxygen in the form of oxides and silicates. [13].

Zirconia is an extremely versatile ceramic that has found use in oxygen pumps and sensors, fuel cells, thermal barrier coatings, and other high-temperature applications, all of which make use of the electrical, thermal, and mechanical properties of this material. Proof of the interest and usefulness of zirconia can be seen from the voluminous literature found on this material [14]

Zirconia ceramics are used for the manufacture of critical parts, for example, in the nuclear industry, in metallurgy for troughs, crucibles for the continuous casting of steels, crucibles for melting platinum and rare earth elements, pipes, in the manufacture of drawing tools for forming wire products, and in the automotive industry for the manufacture of brake discs for high-end cars. In the aviation and space industry, it is irreplaceable, since due to its properties aircraft and spaceships can withstand very high temperatures. It is also used in medicine, for example, for endoprosthetic as the heads of artificial hip joints. It exhibits its best qualities for dental prostheses in dentistry [13].

ZrO₂ occurs in three forms: monoclinic, tetragonal and cubic. The monoclinic phase is stable at room temperatures up to 1170 °C, the tetragonal at temperatures of 1170-2370 °C and the cubic at over 2370 °C. However, noticeable changes in volume are associated with these transformations: during the monoclinic to tetragonal transformation a 5% decrease in volume occurs when zirconium oxide is heated, conversely, a 3-4% increase in volume is observed during the cooling process [12].

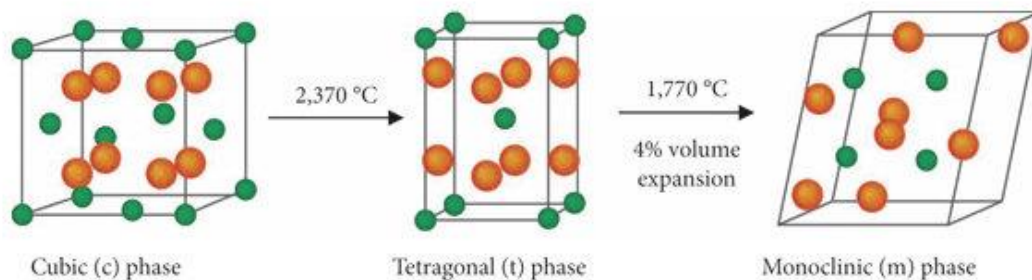


Figure 19: Temperature-related phase transformation of zirconia [15].

Most engineering applications make use of the tetragonal and cubic phases, even though their stability at low temperatures is quite low. In fact, the engineering use of all three phases of zirconia in pure form is rare.

Generally, zirconia is doped with oxides such as Y₂O₃ that stabilize the high-temperature phases at room temperature. This has enormous consequences for both the mechanical and electrical properties of zirconia, even though the local atomic and electronic structure of Zr⁴⁺ in all three polymorphs is for the most part dopant independent [14].

2.3.1 Cubic zirconia

Pure cubic zirconia is a high temperature phase existing from 2377 to 2710°C in the stoichiometric form. It has a fluorite structure, in space group $Fm\bar{3}m$, with $a \approx 5.15 \text{ \AA}$.

The cubic phase extends over a very large range of oxygen compositions, from Zr_2O_3 to ZrO_2 . The preferred stoichiometry (in an unlimited supply of oxygen) is uncertain, as are the structural implications of non-stoichiometry. It can be seen that oxygen non-stoichiometry stabilizes the cubic phase to $\sim 1525^\circ\text{C}$, well below the stability range of the stoichiometric compound (2377°C) [16].

Large transparent crystals of cubic zirconia stabilized by rare earth (REE) oxides dopants are used in jewelers as an imitation diamond due to their high refractive index and dispersion [13].

2.3.2 Tetragonal zirconia

Stoichiometric cubic zirconia transforms to tetragonal polymorph at 2377°C . The tetragonal phase is normally stable down to 1205°C [16].

Both monoclinic and tetragonal structures are distortions of the cubic structure of the fluorite type with coordination numbers 7, 8, and 8 for these structural types.

Means for stabilizing t- ZrO_{2-x} , below 1205°C include alloying with other oxides and the so-called “grain size stabilization” [16].

2.3.3 Monoclinic zirconia

Zirconia undergoes a phase transformation on cooling from tetragonal to monoclinic phase at about 1170°C which is accompanied by a 4% volume increase [17].

Baddeleyite has the space group symmetry $P21/c$ with four ZrO_2 in the unit cell. The unit-cell dimensions are: $a = 5.169$, $b = 5.232$, $c = 5.341 \text{ \AA}$ [18].

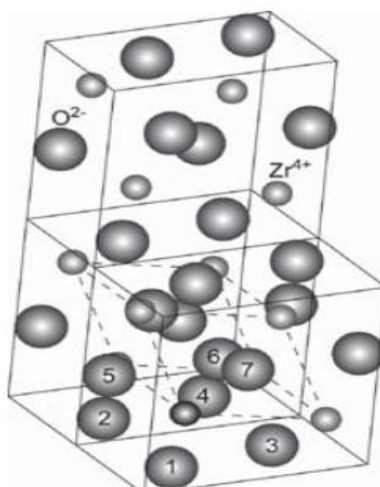


Figure 20: Crystal structure of monoclinic zirconia as seen from the $[1\bar{3}1]$ direction [14].

Baddeleyite ZrO_2 was discovered in 1892 by Joseph Baddeley, a tea tycoon, in Ceylon (now Sri Lanka). Baddeleyite crystals are usually 30–50 μm , the mineral belongs to the monoclinic system, and has a hardness of 6.5(Mohs) and a density from 5.4 to 6.0 g/cm^3 . Baddeleyite was found not only in terrestrial but also in lunar rocks, as well as in some achondritic meteorites [19].



Figure 21: Baddeleyite from Phalaborwa, South Africa [20].

Baddeleyite has a different colour, it ranges from colourless to iron black. In thin fragments it is translucent. Cleavage according to (001) is perfect, according to (010) and (110) it is imperfect. When heated to 1100–1200 $^{\circ}C$, it reversibly transforms into a tetragonal modification (ruffite), the reverse transition occurs at 950- 850 $^{\circ}C$, the tetragonal modification transition temperature increases in the presence of SnO_2 impurity [13].

2.3.4 Nano-zirconia

Nano-zirconia, specifically baddeleyite, refers to zirconium dioxide (ZrO_2) particles at the nanoscale that exhibit the crystal structure characteristic of baddeleyite.

In recent years, ZrO_2 nanoparticles have attracted wide attention due to their size-dependent properties and significant technological applications. ZrO_2 nanoparticles with a high refractive index are used as fillers in transparent coatings such as anticorrosive, antireflection, and scratch-proof coatings [21].

Hydrothermal synthesis of ZrO_2 nanocrystals is of interest as allowing preparation of a monodisperse material with preset particle size and crystal structure. The particle size of monoclinic ZrO_2 nanocrystals formed under hydrothermal conditions is approximately equal, 15-30 nm [22].

Sol-gel is a technique that can result in the formation of nano-crystalline zirconia with particle size less than 20nm [23].

Another technique for synthesizing nano zirconia is ball-milling. The ball-milling process strongly influences the formation of uniform-sized spherical particles with a high surface area. Fully crystalline monoclinic ZrO₂ nanoparticles with an average particle size of 64 nm [21].

CHAPTER III: Fundamentals of Composite Materials

3. Composite materials

Introduction

A composite material is composed of two or more substances exhibiting different chemical and physical properties. Its purpose is to enhance the characteristics of the base materials it comprises. Composites provide notable advantages in various aspects of material performance, surpassing the capabilities of single-material alternatives, especially when compared to the individual use of the constituent components. At a macroscopic scale, the phases are indistinguishable, but at some microscopic scales, the phases are clearly separate, and each phase exhibits the characteristics of the pure material [24].

Composites occur very commonly in nature. Some of the best examples are wood, bone, various minerals, mollusk shells, and insect exoskeletons. In wood, the cellulose fibers of the cell wall are “glued” together by the lignin matrix. Bone is composed of calcium hydroxyapatite crystals in a protein matrix. Mollusk shells are composites of calcium carbonate layers in various geometries bound together by a multilayer matrix. Insect exoskeletons bear a striking resemblance to man-made fiber-reinforced composites [24].

3.1 Characteristics

Various materials can be classified as composites, characterized by their composition of multiple distinctly different and identifiable substances at the microscopic level. These composites find extensive use across diverse industries and applications, primarily driven by the demand for materials that are both strong and lightweight. Utilizing composites results in weight reduction and enables the creation of designs that can customize the mechanical properties to match the structural loading requirements. Moreover, composites are increasingly substituting conventional engineering materials in numerous industrial, recreational, architectural, transportation, and infrastructure applications.

This particular category of composites always involves two essential components: a reinforcing phase and a matrix phase. The reinforcing phase commonly includes materials like graphite, glass, ceramics, or polymer fibers, while the matrix is usually a polymer, though it could also be ceramic or metal [24].

Numerous composite materials consist of two main phases: the matrix, which is continuous and envelops the second phase known as the reinforcing phase. The properties of composites are influenced by the characteristics of both constituent phases, their proportions, and the configuration of the dispersed phase. Dispersed phase geometry refers to factors such as particle shape, size, distribution, and orientation, and these attributes are depicted in the overall composite properties.

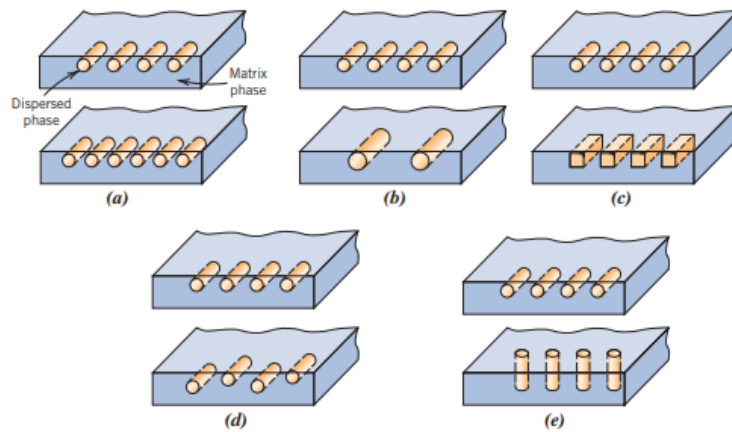


Figure 22: Schematic representations of the various geometrical and spatial characteristics of particles of the dispersed phase that may influence the properties of composites: (a) concentration, (b) size, (c) shape, (d) distribution, and (e) orientation.

In particle-reinforced composites, the dispersed phase exhibits equiaxed characteristics, meaning that the particle dimensions are roughly uniform in all directions. In contrast, for fiber-reinforced composites, the dispersed phase takes on the geometry of a fiber, featuring a significant length-to-diameter ratio. Structural composites, designed with multiple layers, aim for low densities and exceptional structural integrity. In the case of nanocomposites, the dimensions of dispersed phase particles are at the nanometer scale [4].

3.2 Types of composite materials

The range of composites employed in manufacture/construction is extensive, but they fall into these broad categories:

- **Metal-Matrix Composite**
 Metal composite materials have found application in many areas of daily life for quite some time. Often it is not realized that the application makes use of composite materials. Materials like cast iron with graphite or steel with a high carbide content, as well as tungsten carbides, consisting of carbides and metallic binders, also belong to this group of composite materials [25]. These innovative materials offer boundless opportunities for advancements in contemporary material science and development. The properties of metal matrix composites (MMCs) can be tailored and customized according to specific applications, providing designers with the flexibility to incorporate desired characteristics. This potential allows MMCs to meet all the envisioned requirements of designers. Metal matrix composites can be classified in various ways. One classification is the consideration of type and contribution of reinforcement components in particle-, layer-, fiber- and penetration composite materials.

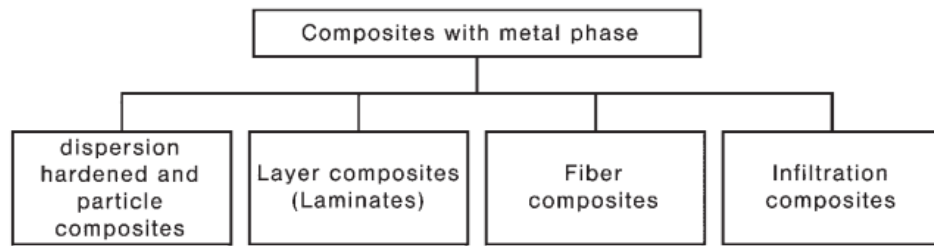


Figure 23: Classification of composite materials with metal matrixes [25].

- Polymer–Matrix composites

Polymer–matrix composites (PMCs) consist of a polymer resin as the matrix and fibers as the reinforcement medium. These materials are used in the greatest diversity of composite applications, as well as in the largest quantities, in light of their room-temperature properties, ease of fabrication, and cost.

Polyesters and vinyl esters stand out as the most widely utilized and cost-effective polymer resins in the realm of composite materials. Primarily employed in glass fiber–reinforced composites, these matrix materials offer a diverse array of properties owing to numerous available resin formulations. In contrast, epoxies, although pricier, find extensive use in aerospace applications within polymer matrix composites (PMCs). They outperform polyesters and vinyl esters in terms of mechanical properties and resistance to moisture. For applications demanding elevated temperatures, polyimide resins are the material of choice, boasting a continuous-use upper-temperature limit of approximately 230°C (450°F). Looking ahead, high-temperature thermoplastic resins, such as polyetheretherketone (PEEK), poly(phenylene sulfide) (PPS), and polyetherimide (PEI), hold promise for future aerospace applications. These advanced materials offer the potential to address high-temperature challenges while expanding the range of possibilities in composite design and performance [4].

- Ceramic-Matrix composites

Ceramic materials possess inherent resistance to oxidation and degradation when exposed to elevated temperatures. Despite this advantageous quality, their susceptibility to brittle fracture has limited their widespread use in high-temperature and high-stress applications, particularly in components for automobile and aircraft gas turbine engines. The brittle nature of ceramics has been a hindrance to their ideal candidacy in such demanding environments. To address the challenge of brittle fracture, significant advancements have been made through the development of a new generation of ceramic-matrix composites (CMCs). These CMCs involve the incorporation of particulates, fibers, or whiskers of one ceramic material into a matrix composed of another ceramic. This innovative approach enhances the fracture toughness of ceramics, making them more

resilient and durable, thereby expanding their potential applications in high-temperature and stress-inducing scenarios. The evolution of ceramic-matrix composites represents a promising stride towards unlocking the full potential of ceramics in demanding engineering applications [4].

3.3 Particle- reinforced composites

Particle-reinforced composites are categorized into two subtypes: large-particle and dispersion-strengthened composites, distinguished by their respective reinforcement mechanisms. The term "large" indicates that interactions between particles and matrix cannot be addressed at the atomic or molecular level, instead, continuum mechanics is applied. In the majority of these composites, the particulate phase exhibits greater hardness and stiffness compared to the matrix. These reinforcing particles play a role in constraining the movement of the matrix phase near each particle, effectively transferring a portion of the applied stress to the particles, which then bear a fraction of the load. The extent of reinforcement and improvement in mechanical behavior is contingent upon a robust bond at the interface between the matrix and particles. Additionally, it's important to note that large-particle and dispersion-strengthened composites employ distinct approaches to reinforce the material. In large-particle composites, the emphasis lies on continuum mechanics due to the relatively sizable particles, while dispersion-strengthened composites involve a finer distribution of particles, often at the nanoscale, contributing to enhanced mechanical properties. The success of these composite materials hinges on achieving a strong bond between the matrix and particles, thereby optimizing their overall performance. For dispersion-strengthened composites the matrix bears the major portion of an applied load, the small, dispersed particles hinder or impede the motion of dislocations. Thus, plastic deformation is restricted such that yield and tensile strengths, as well as hardness, improve [4].

3.4 Nano-composite materials

The materials world is experiencing a revolution with the development of a new class of composite materials, nanocomposites. These materials are characterized by the inclusion of nanosized particles, commonly referred to as nanoparticles, embedded within a matrix material. Nanocomposites exhibit the potential to surpass conventional filler materials in various aspects, including mechanical, electrical, magnetic, optical, thermal, biological, and transport properties. Moreover, these properties can be precisely tailored to meet the specific requirements of diverse applications. For instance, metal ship hulls are strong, but without frequent painting will corrode. Ceramics are corrosion resistant but are very brittle to serve in ship hulls. Polymers are wonderfully corrosion resistant and light, unfortunately, polymers absorb small quantities of moisture that can decrease the strength of the material and cause layer of the hull to separate after some years in the service. The addition of 2% nanoceramic mica or clay, flake ceramics, will decrease water permeability by up to 50% [26].

Nanoparticles have those chemical and physical properties that makes them very different from that of the corresponding bulk materials due to their small size and large surface to volume ratio [27].

The versatility and superior performance of nanocomposites have led to their integration into a myriad of modern technologies. Their unique characteristics and customizable nature make them increasingly indispensable in various industries, contributing to advancements in fields ranging from electronics and medicine to energy and aerospace. The ongoing development and application of nanocomposites signify a profound shift in materials science, opening up new frontiers for innovation and technological progress.

In the present postgraduate thesis nickel matrix nanocomposite coatings, using zirconia nanoparticle as reinforcements have been produced.

CHAPTER IV:
A Comprehensive Review in
Electrolysis

4. The process of electrolysis

Introduction

Electrolysis is an electrochemical process in which electrical energy is the driving force of chemical reactions. Substances are decomposed by passing a current through them. The first observation of this phenomenon was recorded in 1789. Nicholson and Carlisle were the first who developed this technique back in 1800 and by the beginning of the 20th century there were already 400 industrial water electrolysis units in use [28].

The significance of electrolysis lies in its ability to exert precise control over chemical transformations, enabling the synthesis of valuable materials, purification of metals, etc.

In industrial applications, electrolysis is pivotal to produce metals like aluminum and copper, where it allows for the extraction and refinement of these materials with high purity. Moreover, it finds extensive use in electroplating, water treatment, and the synthesis of chemicals with wide-ranging industrial applications.

4.1 Connection between Chemistry and Electricity

The connection between chemistry and electricity is a very old one, going back to Alessandro Volta's discovery, in 1793, that electricity could be produced by placing two dissimilar metals on opposite sides of a moistened paper. In 1800, Nicholson and Carlisle, using Volta's primitive battery as a source, showed that an electric current could decompose water into oxygen and hydrogen. In 1812, the Swedish scientist Berzelius suggested the idea that every atom possesses an electrical charge, with hydrogen and metals carrying a positive charge, while nonmetals carry a negative charge. According to this concept, in electrolysis, the applied voltage was believed to overcome the attraction between these opposing charges, causing electrified atoms to separate into ions, term coined by William Whewell from the Greek word for "travelers" [29].

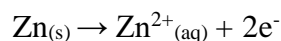
During this time, the utilization of electricity to induce chemical transformations remained a pivotal factor in the progress of chemistry. Humphrey Davey successfully produced the first elemental sodium through the electrolysis of sodium hydroxide. It was left to Davey's former assistant, Michael Faraday, to demonstrate a direct correlation between the amount of electric charge applied to a solution and the quantity of electrolysis products obtained [29].

4.2 Electroneutrality and Oxidation-Reduction process

Electroneutrality refers to the condition in which an atom, molecule, or an entire system has an equal number of positively charged protons and negatively charged electrons. In other words, it has an electrical charge of zero. This balance between positive and negative charges ensures that the overall charge of the system is neutral or electrically stable.

The electroneutrality approximation assumes that charge separation is impossible in electrolytic solutions [30].

For instance, when zinc metal is immersed in pure water, a small number of zinc atoms go into solution as zinc ions, while the electrons are left behind in the metal:



As this process continues, the electrons that remain in the zinc create a negative charge within the metal, making it progressively more challenging for additional positive ions to exit the metallic phase, due to strong attraction forces. As positively charged ions enter the solution, a corresponding accumulation of positive charge in the liquid phase contributes to this inhibitory effect.

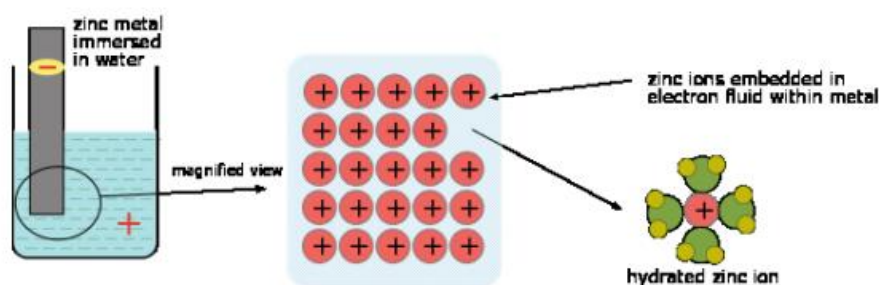


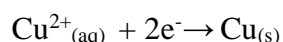
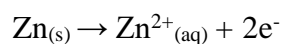
Figure 24: Oxidation of metallic zinc in contact with water [29].

Oxidation is the chemical reaction in which a substance loses electrons. This process involves the transfer of electrons from one substance to another. The substance that loses electrons is said to be oxidized.

Oxidation process coupled with Reduction, a process that restores the electroneutrality between the two phases [29].

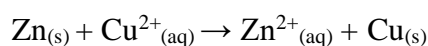
In contrast with oxidation, Reduction is the chemical reaction in which a substance gains electrons. The substance that gains electrons is to be reduced.

For example, when zinc is immersed in a solution of copper sulfate instead of pure water, the zinc metal quickly becomes covered with a black coating of finely-divided metallic copper. The reaction is a simple oxidation-reduction process, a transfer of two electrons from the zinc to the copper:



The explanation of the phenomenon is as follows: the Zinc, initially in solid form, when immersed in a copper solution, donates two electrons to the copper, transforming into a Zn^{2+} solution. The copper, in turn, accepts the two electrons and undergoes a conversion from a Cu^{2+} solution to solid copper. That's the reasons why the zinc metal been covered with metallic copper.

The Ox-Red reaction is:



4.3 Electrical double layer

The concept of the existence of the double layer at the surface of a metal being in contact with an electrolyte appeared in 1879 (Helmholtz) [31].

The electrical double layer is the array of charged particles and oriented dipoles which is thought to exist at every interface. Very often the term is used in a narrower sense to mean the array of charges and dipoles between two immiscible media when one is a salt solution [32].

The double layer was thought to consist of two layers of charge, one positive and one negative, situated at the interface. Briefly, the electrical double layer typically comprises an electron layer (in the case of a non-electrolytic phase like a metal or electronic conductor), an adsorbed ion layer, and a diffuse double layer containing an ionic atmosphere. In this atmosphere, ions of one charge exceed their usual concentrations, while those of the opposite charge are in lower quantities. Finally, at the interface, there might be a thin layer of neutral molecules, often monomolecular. Regardless of their orientation, these molecules can impact the thermodynamic properties of the interface. [32].

The formation of the double layer at a metal-electrolyte surface involves the interaction between the charged metal surface and the surrounding electrolyte solution. When a metal surface is placed in an electrolyte solution, it can acquire a charge. Ions from the electrolyte solution are attracted to the charged metal surface. For example, if the metal surface becomes negatively charged, cations (positively charged ions) from the solution will be attracted to it, in contrast, if the metal surface becomes positively charged, anions will be attracted to it. The Helmholtz layer is the innermost part of the electrical double layer, directly adjacent to the charged metal surface. It consists of ions that are tightly bound or specifically absorbed to the metal surface.

Simultaneously, the presence of the charged metal surface causes the water molecules near the surface to align themselves in a specific orientation, due to the fact that water molecules are polar. The positive end of water molecules is attracted to the negatively charged metal surface, and the negative end is repelled. This “sheath” is extending from the Helmholtz layer into the solution. Beyond this region, ions from the solution are present in a more diffuse manner, creating the diffuse layer, the outer part of the electrical double layer.

A classic, simplified model of the double layer formed at the metal electrode surface is presented in Figure 25.

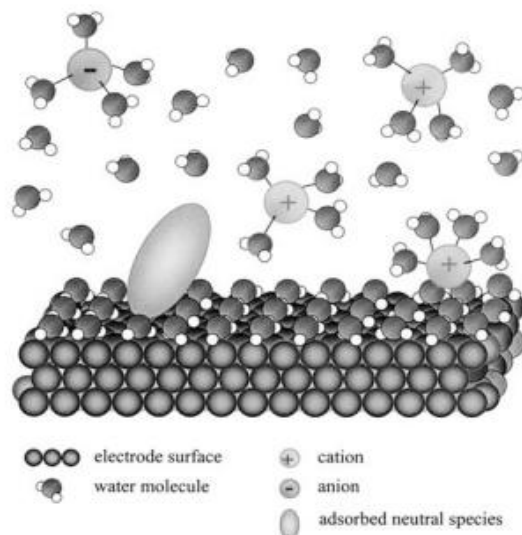


Figure 25: General representation of the double layer formed at the metal–electrolyte interface [31].

As described before, there is a layer of adsorbed water molecules on the electrode surface. In dipolar solvents, such as water, the dipoles must interact with the charged metal surface. Since it has been assumed that there is excess of negative charge at the metal phase, the hydrogen atoms of adsorbed water molecules are oriented toward the metal surface. For excess of positive charge at the metal surface, the dipoles of water will have a different orientation, the oxygen atoms of adsorbed water molecules will be oriented toward the metal surface. The inner Helmholtz plane (IHP) passes through the centers of specifically adsorbed ions (compact layer in the Helmholtz model), or is simply located just behind the layer of adsorbed water. The second plane is called the outer Helmholtz plane (OHP) and passes through the centers of the hydrated ions that are in contact with the metal surface. The diffuse layer develops outside the OHP [31].

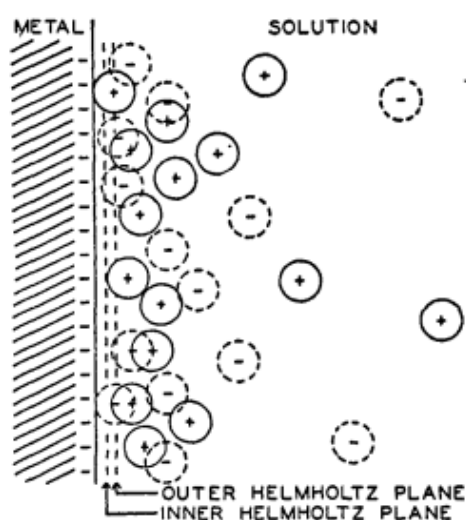


Figure 26: Schematic representation of the electrical double layer with negative polarization. Large circles represent solvated ions. Dotted circles represent “ghosts”, ions which would be present if the double layer were not there [32].

4.4 Potential differences at interfaces

Electrochemistry is the study of reactions in which charged particles (ions or electrons) cross the interface between two phases of matter, typically a metallic phase (the electrode) and a conductive solution, or electrolyte. A process of this kind can always be represented as a chemical reaction and is known generally as an electrode process. Electrode processes take place within the double layer and produce a slight unbalance in the electric charges of the electrode and the solution. The significance of electrochemistry lies in its capacity to correlate these potential differences with the thermodynamics and kinetics of electrode reactions. Notably, manipulating the interfacial potential difference provides a crucial means of externally controlling electrode reactions.

The typical method for measuring a potential difference between two points involves using a voltmeter with its leads in contact with those points. While it's straightforward to connect one lead of the meter to a metallic electrode, it becomes challenging to connect the other lead to the solution side of the interfacial region without introducing a second electrode, each with its own interfacial potential. Consequently, measuring single electrode potentials, commonly referred to as such, is not directly observable since it entails measuring the sum of two potential differences [29]. While it's physically impossible to directly measure the potential difference between a piece of metal and the solution it's immersed in, it's easy to measure the potential difference between two such electrodes when both are immersed in a solution.

4.5 Electrochemical Cell

An electrochemical cell is a device capable of either generating electrical energy from chemical reactions or using electrical energy to cause chemical reactions. This versatile device serves the dual purpose of harnessing the potential energy stored in chemical compounds to generate electricity, or conversely, utilizing external electrical energy to drive chemical transformations within its structure. Such cells capable of generating an electric current from the chemical reactions occurring in them are called Galvanic cells or Voltaic cells. Alternatively, the cells which cause chemical reactions to occur in them when an electric current is passed through them are called electrolytic cells [33].

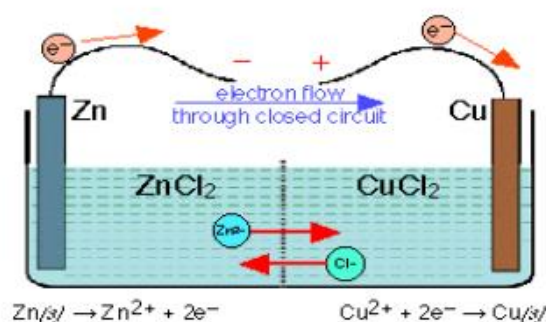
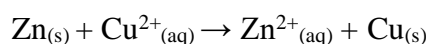


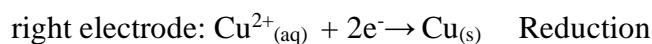
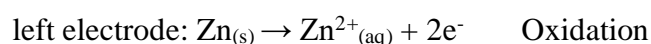
Figure 27: A simple Galvanic Cell [29].

Figure 27 represent a galvanic cell. A standard galvanic cell setup consists of two distinct metal pieces, here zinc and copper, that are employed. Each metal is immersed in a solution containing a dissolved salt specific to the respective metal. A porous barrier separates the two solutions, preventing rapid mixing while allowing ions to diffuse through. Left in that condition, no significant amount of reaction would take place. However, by establishing a connection between the zinc and copper through a metallic conductor, a transformative process ensues. As Zn^{2+} ions enter the solution in the left cell, surplus electrons are generated. These excess electrons can then flow through the external circuit, ultimately reaching the right electrode. At this point, the electrons can be transferred to the Cu^{2+} ions, inducing their discharge or conversion into Cu atoms at the surface of the copper electrode. This interconnected system thus enables a continuous flow of electrons, facilitating the electrochemical reactions.

The net reaction is the same as before, the oxidation of zinc by copper ions:



but this time, the oxidation and reduction steps take place in separate locations:



Electrochemical cells generally consist of a cathode (working electrode) and an anode (counter electrode). Anode serves as the site of oxidation, where a metal undergoes a process releasing electrons into the external circuit. On the other hand, the cathode, the electrode where reduction occurs, becomes the locus where electrons from the external circuit combine with ions, facilitating a reduction reaction. Typically associated with metal ions in the solution, the cathode causes these ions to undergo reduction, resulting in the formation of solid metal at the electrode surface.

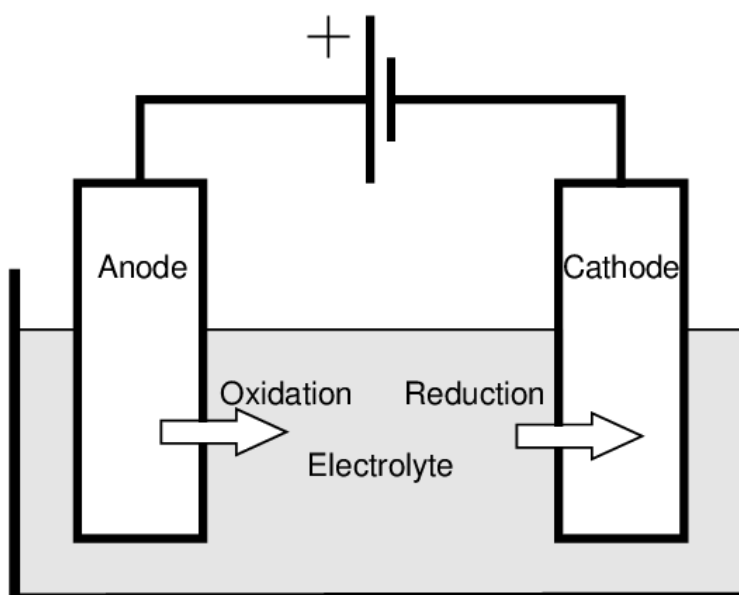


Figure 28: A simple Electrolytic Cell [34].

Figure 28 represents an electrolytic cell. An electrolytic cell utilizes electrical energy to drive a non-spontaneous chemical reaction. Unlike a galvanic cell (or voltaic cell), which spontaneously converts chemical energy into electrical energy, an electrolytic cell requires an external power source to induce a chemical change. Electrolysis occurs in an electrolytic cell.

Electrolysis is a process by which electric current is passed through a substance to effect a chemical change. The chemical change is one in which the substance loses or gains an electron (oxidation or reduction). The process is carried out in an electrolytic cell, an apparatus consisting of positive and negative electrodes held apart and dipped into a solution containing positively and negatively charged ions.

4.6 Faradaic and non-Faradaic current

When an analyte undergoes oxidation or reduction at the electrode in one half-cell, the resulting electrons pass through the potentiometer to reach the electrode in the other half-cell, where a corresponding reduction or oxidation reaction occurs. In either case, the current from the redox reactions at the two electrodes is called a faradaic current. Specifically, a cathodic current arises from the reduction of an analyte and carries a positive sign, while an anodic current results from the analyte's oxidation and carries a negative sign. In addition to the faradaic current from a redox reaction, the current in an electrochemical cell includes non-faradaic sources. For instance, the charge of an electrode is initially zero, and its potential is altered, leading the electrode's surface to acquire a positive charge. In response, cations near the electrode's surface migrate away, while anions move toward the electrode. This ion migration persists until equilibrium is established between the positive surface charge of the electrode and the excess negative charge in the vicinity of the electrode's surface. This phenomenon gives rise to a brief, minor non-faradaic current known as the charging current. Whenever the potential of the electrode is altered, a transient charging current is observed. Even in the absence of analyte, a small, measurable current flows through an electrochemical cell. This residual current has two components: a faradaic current due to the oxidation or reduction of trace impurities and a non-faradaic charging current [35].

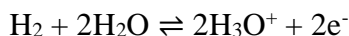
4.7 The standard hydrogen electrode and reference electrodes

The direct quantification of the absolute potential of an anode or cathode proves to be an intricate challenge. To circumvent this complexity, hydrogen electrode has been established as a reference electrode, assigning it a standard potential of zero volts under specific standard conditions (25°C, 1atm pressure, 1M concentration of ions) [2]. Since hydrogen ions gain electrons to form hydrogen gas during reduction, assigning a standard potential of zero volts to this half-reaction simplifies the comparison of reduction potentials for other substances. Consequently, the potential of the anode or cathode in a given electrochemical cell is measured in relation to the standard hydrogen electrode.

Stronger oxidizing agent ↑	$F_2(g) + 2 e^-$	$\longrightarrow 2 F^-(aq)$	2.87	Weaker reducing agent ↓
	$H_2O_2(aq) + 2 H^+(aq) + 2 e^-$	$\longrightarrow 2 H_2O(l)$	1.78	
	$MnO_4^-(aq) + 8 H^+(aq) + 5 e^-$	$\longrightarrow Mn^{2+}(aq) + 4 H_2O(l)$	1.51	
	$Cl_2(g) + 2 e^-$	$\longrightarrow 2 Cl^-(aq)$	1.36	
	$Cr_2O_7^{2-}(aq) + 14 H^+(aq) + 6 e^-$	$\longrightarrow 2 Cr^{3+}(aq) + 7 H_2O(l)$	1.33	
	$O_2(g) + 4 H^+(aq) + 4 e^-$	$\longrightarrow 2 H_2O(l)$	1.23	
	$Br_2(l) + 2 e^-$	$\longrightarrow 2 Br^-(aq)$	1.09	
	$Ag^+(aq) + e^-$	$\longrightarrow Ag(s)$	0.80	
	$Fe^{3+}(aq) + e^-$	$\longrightarrow Fe^{2+}(aq)$	0.77	
	$O_2(g) + 2 H^+(aq) + 2 e^-$	$\longrightarrow H_2O_2(aq)$	0.70	
	$I_2(s) + 2 e^-$	$\longrightarrow 2 I^-(aq)$	0.54	
	$O_2(g) + 2 H_2O(l) + 4 e^-$	$\longrightarrow 4 OH^-(aq)$	0.40	
	$Cu^{2+}(aq) + 2 e^-$	$\longrightarrow Cu(s)$	0.34	
	$Sn^{4+}(aq) + 2 e^-$	$\longrightarrow Sn^{2+}(aq)$	0.15	
	$2 H^+(aq) + 2 e^-$	$\longrightarrow H_2(g)$	0	
	$Pb^{2+}(aq) + 2 e^-$	$\longrightarrow Pb(s)$	-0.13	
	$Ni^{2+}(aq) + 2 e^-$	$\longrightarrow Ni(s)$	-0.26	
$Cd^{2+}(aq) + 2 e^-$	$\longrightarrow Cd(s)$	-0.40		
$Fe^{2+}(aq) + 2 e^-$	$\longrightarrow Fe(s)$	-0.45		
$Zn^{2+}(aq) + 2 e^-$	$\longrightarrow Zn(s)$	-0.76		
$2 H_2O(l) + 2 e^-$	$\longrightarrow H_2(g) + 2 OH^-(aq)$	-0.83		
$Al^{3+}(aq) + 3 e^-$	$\longrightarrow Al(s)$	-1.66		
$Mg^{2+}(aq) + 2 e^-$	$\longrightarrow Mg(s)$	-2.37		
$Na^+(aq) + e^-$	$\longrightarrow Na(s)$	-2.71		
$Li^+(aq) + e^-$	$\longrightarrow Li(s)$	-3.04		

Figure 29: Standard reduction potentials [36].

The standard hydrogen electrode is the primary standard in electrochemistry. It is based on the following reversible equilibrium:

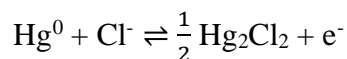


The standard hydrogen electrode consists of a platinum wire or a platinum sheet covered with platinum black (i.e. platinised) and an electrolyte solution containing hydronium ions. The hydrogen gas is usually continuously supplied [37].

4.7.1 The calomel electrode

The calomel electrode was introduced by Ostwald in 1890. As a reference electrode of fixed, well-known and very reproducible potential, it is still important today. In the simplest case, a single drop of mercury is placed in a small tube and is covered by mercury(I) chloride (calomel Hg_2Cl_2). Another possibility is to fill a small glass tube with a paste of mercury, mercury(I) chloride and potassium chloride solution. The paste is in contact with a potassium chloride solution of constant activity. Mostly, a saturated potassium chloride solution is used and the paste additionally contains solid potassium chloride [37].

The electrode net reaction can be formulated in the following way:



Under standard conditions, the standard potential for this reaction is approximately 0.241V.

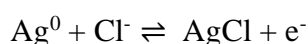
The Nernst equation can be applied to calculate the potential of the calomel electrode under non-standard conditions:

$$E_{cell} = E_{Hg_2Cl_2|Hg_2^{2+},Cl^-}^0 - \frac{RT}{nf} \ln \frac{1}{[Hg_2^{2+}] \cdot [Cl^-]^2} \quad (4)$$

4.7.2 The Silver/Silver chloride electrode

This electrode the most frequently used reference electrode in practical measurements, because the construction is very simple, the potential is very well reproducible, and last, but not least, this electrode is free of mercury. Normally, a silver wire is covered with silver chloride, which can be achieved electrochemically or thermally. The construction of a commercially available silver/silver chloride electrode is similar to the calomel electrode [37].

The electrolyte solution in these reference systems is normally a potassium chloride solution (mostly saturated or 3 M), and only seldom sodium or lithium chloride. The electrode net reaction is



In this thesis, the electrochemical processes were conducted utilizing a calomel electrode as reference electrode.

4.8 Cell potential

The cell potential, E_{cell} , is the measure of the potential difference between the anode and the cathode. The potential difference is caused by the ability of electrons to flow from one half cell to the other. Electrons are able to move between electrodes because the chemical reaction is a redox reaction. A redox reaction occurs when a certain substance is oxidized, while another is reduced. During oxidation, the substance loses one or more electrons, and thus becomes positively charged. Conversely, during reduction, the substance gains electrons and becomes negatively charged. This relates to the measurement of the cell potential because the difference between the potential for the reducing agent to become oxidized and the oxidizing agent to become reduced will determine the cell potential. So, it represents the driving force or voltage generated by the electrochemical reactions occurring within the cell. The cell potential (E_{cell}) is measured in voltage (V) [38]. The standard hydrogen electrode serves as a benchmark against which the cell potential is measured.

The overall cell potential is a sum of two half-cell potentials, and the cell potential is given by:

$$E^0_{\text{cell}} = E^0_{\text{cathode}} - E^0_{\text{anode}} \quad (5)$$

Both potentials used in this equation are standard reduction potentials.

If the cell potential is positive, the cell reaction is spontaneous under the given conditions (galvanic cell). Conversely, if the cell potential is negative, the cell reaction is non-spontaneous (electrolytic cell).

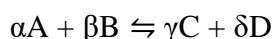
The standard cell potential, typically measured under well-defined conditions, serves as a reference point. However, in the real-world, the electrochemical processes conducted under other conditions, and this is where the Nernst equation emerges as a crucial tool.

The Nernst equation expressed as,

$$E_{Cell} = E_{Cell}^0 - \frac{RT}{nF} \ln(Q) \quad (6)$$

Where E_{Cell} is the cell potential under non-standard conditions, E_{Cell}^0 is the standard cell potential, R is the gas constant (8.314 J/mol·K), T is the temperature in Kelvin, n is the number of electrons which transferred, F is the Faraday constant (96485.3321 s·A/mol), and Q is the reaction quotient.

A general chemical reaction in which a moles of a reactant A and b moles of a reactant B react to give c moles of a product C and d moles of a product D can be written as,



Mathematically, the reaction quotient is expressed as ,

$$Q = \frac{[C]^\gamma [D]^\delta}{[A]^\alpha [B]^\beta} \quad (7)$$

4.9 The Laws of Electolysis

It is important to consider the quantitative relationship between the degree of chemical change and the electrical charge involved. This relationship was first stated by Michael Faraday in 1834 following a series of classical electrolysis experiments. Faraday's Laws of Electrolysis provide one of the most elegant and important mathematical statements in electrochemistry [39].

The laws state that (1) the amount of chemical change produced by current at an electrode-electrolyte boundary is proportional to the quantity of electricity used and (2) the amounts of chemical changes produced by the same quantity of electricity in different substances are proportional to their equivalent weights. In electrolytic reactions, the equivalent weight of a substance is the formula weight in grams associated with a gain or loss of an electron [40].

$$m = \frac{M \cdot I \cdot t}{n \cdot F} \quad (8)$$

Where, m is the weight (g_r), M is the Molar mass(g_r/mol), I is the current intensity (A), t is the time of electrolysis (sec), n the amount of electrons which are transferred and F is the Faraday constant.

4.10 Mass tranfer in electorlytic cell

Mass transfer analysis of an electrolytic bath includes the study of parameters like bath ionic conductivity, transference number, mobility, and diffusivity of different ions [41].

There are three basic mechanisms of mass transport:

- Diffusion, defined as the spontaneous movement of any material from where it is to where it is not
- Migration, the movement of charged particles in an electric field
- Convection, movement of material contained within a volume element of stirred (hydrodynamic) solution

Diffusion occurs whenever the concentration of an ion or a molecule at the surface of the electrode is different from that in bulk solution. Convection occurs when there is a mix of the solution, which carries reactants toward the electrode and removes products from the electrode. The most common form of convection is stirring the solution with a stir bar. Other methods include rotating the electrode and incorporating the electrode into a flow-cell. The final mode of mass transport is migration, which occurs when a charged particle in solution is attracted to or repelled from an electrode that carries a surface charge. If the electrode carries a positive charge, for example, an anion will move toward the electrode and a cation will move toward the bulk solution. Unlike diffusion and convection, migration affects only the mass transport of charged particles [35].

4.11 Energy losses in electrochemical cell

Processes in an electrochemical cell, such as the conduction of ions in the electrolyte and electron transfer reactions, contribute to losses in cell efficiency.

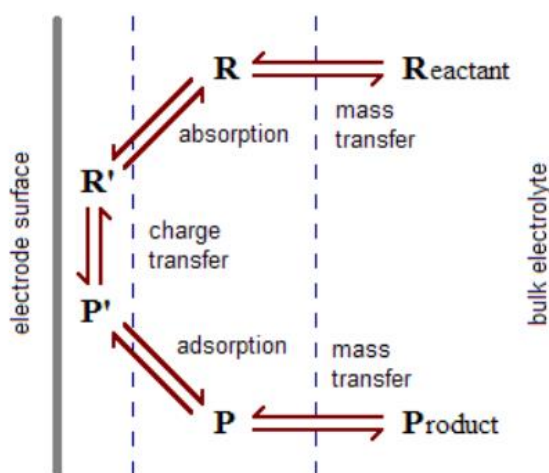


Figure 30: Chemical processes involved in an electrochemical cell [42].

These chemical processes contribute resistances that increase the voltage required to drive electrolysis cells and decrease the voltage produced in fuel cells. Energy losses in an electrochemical cell are due to mass transfer resistance, solution resistance, charge transfer resistance, and circuit resistance. Circuit resistance encompasses the resistances caused by the electrical wires and connections. The transfer of mass between electrodes that is faster than the mass's rate of diffusional flux causes mass transfer resistance. The conduction of protons through electrolyte and the bubbles of molecular H_2 and O_2 cause mass transfer resistance in electrolysis and fuel cells. The electrolyte conductivity, including membranes and salt bridges, spacing between electrodes, and void fractions caused by bubbles affect mass transfer resistance. Both the anodic and cathodic reactions have their own charge transfer resistances and solution resistances. Reactions at the interface between the electrode surface and the electrolyte cause solution resistances. [42].

4.12 Ohmic Voltage Drop

In a three-electrode system, at the open circuit potential (OCP), the current that flows between RE (reference electrode) and WE (working electrode, cathode) is usually in the range of nA or even lower. However, when the current passes at WE (i.e., during operation), there is a significant current flow between WE and the tip of the RE. Hence, the electrolytic conductivity and the distance between RE and WE are the major contributors to the potential drop. This infers that an inevitable drop in the potential is witnessed in all cases of Direct Current (DC) operations in electrochemistry [43]. As a result, any activity evidenced as a function of the applied potential often has a slightly lower potential at the interface than the applied potential. This drop in potential is also known as ohmic potential drop.

In electrolysis, ohmic potential drop refers to the voltage decrease across the electrolyte or the internal resistance of the electrolytic cell due to the resistance encountered by the electric current.

It is possible to calculate the ohmic voltage drop by applying Ohm's Law. Ohm's Law suggests that,

$$\Delta V = I \cdot R_{\omega} \quad (9)$$

Where ΔV is the ohmic potential drop, I is the applying current, R_{ω} is the resistance.

4.12.1 Factors that influence ohmic potential drop

1. Electrolytic conductivity

A lower conductivity of the electrolyte is apparently a prime contributor to the overall internal resistance. The most common way to improve the electrolytic conductivity is to add redox inactive salts. If adding a supporting electrolyte is not an option, the alternative options to improve the electrolytic conductivity to a notable extent are stirring the solution, rotating the electrode, heating the solution, and applying ultrasonic waves [43].

2. The distance between RE and WE

The optimal distance between RE and WE should be determined by one's own discretion depending on the reaction, cell design, and the nature of the catalyst. At all costs, one should avoid touching the WE with the tip of the RE as it would

cause the potential difference to cease to 0.0 V and mislead measurements [43].

3. Electronic conductivity of electrode

A poor electronic conductivity can add up its own resistance to the overall internal resistance. Carbonization is the most commonly used strategy to improve electrode's electronic conductivity. This works well with batteries and supercapacitors and even in some sensors too. However, carbon is not stable enough at high anodic potentials [43].

4. The roughness of WE and double-layer thickness

The thickness of the double-layer can vary from a few nanometers to a few millimeters depending on the

cell dimensions, the quantity of electrolyte, and A/V (area to volume ratio) values. The factors governing the thickness of the doublelayer are not only the surface roughness and active area but also the cell dimensions, the quantity of electrolyte, and A/V [43].

4.13 Polarization of electrodes

Polarization denotes the alteration in electrical potential from a stabilized condition, exemplified by the open-circuit electrode potential, due to the flow of current. This transformation is especially relevant in electrolysis, where the electrode potentials shift, causing the anode to attain a more noble potential and the cathode to become more active than their respective reversible potentials. This shift is frequently induced by the formation of a film on the electrode surface. As a consequence of polarization, the anode experiences an elevation in nobility, while the cathode becomes more active. These potential shifts at the anode and cathode contribute to the establishment of poles in a galvanic cell [44].

The polarization curve displays the voltage output of the fuel cell for a given current density loading. Polarization curves are usually obtained with a potentiostat/galvanostat, which draws a fixed current from the fuel cell and measures the fuel cell output voltage [45].

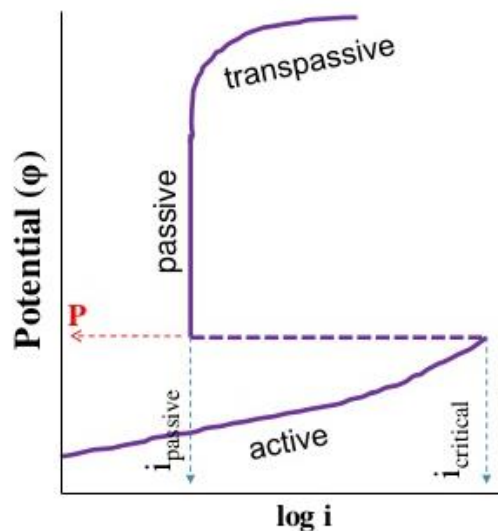


Figure 31: Potentiostatic polarization curve of active-passive metal (Fe) [45].

**CHAPTER V:
Electrolytic deposition
(Electroplating) of Metals**

5. The process of electroplating

Introduction

The process of electrodepositing metals and alloys holds widespread significance and is applied across various fields, including electroplating, electrowinning, and electrorefining. This method plays a pivotal role in enhancing the aesthetic appeal, providing specific surface engineering properties, and protecting against corrosion for a diverse range of items, from everyday domestic components to cutting-edge technological devices.

From a historic point of view, electrodeposition is one of the oldest coating processes in industrial use. The basic principles were developed and applied in the early nineteenth century. Batteries supplied the electrical energy required for electrochemical conversion of dissolved metals. However, this source of energy was far from sufficient. By the mid-nineteenth century, development of the dynamo allowed enough electrical energy to be produced for electrochemical deposition from electrolytes on an industrial scale. Electrodeposition is one of the most common techniques of coating many different materials for aesthetic or technical reasons [46].

Electrodeposition involves the application of a metal or alloy coating onto a conductive surface through electrolysis. This is achieved by utilizing a well-formulated electrolyte, commonly referred to as a bath. The bath can take the form of an aqueous solution containing either a simple salt or a complex salt type. The discharge of a metal during this process is contingent upon its placement in the electrochemical series and the chemical composition of the solution employed for deposition. This technique offers a versatile and controlled means of modifying surfaces to meet specific requirements [47].

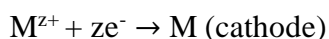
5.1 Fundamentals of electrodeposition

As mentioned in chapter IV, an electrolytic cell consists of an anode (the positive electrode), a cathode (the negative electrode), an electrolytic bath and a current source.

At the cathode and anode, reduction and oxidation take place, respectively, facilitated by the exchange of metal ions and electrons across the interface between the electrode and electrolyte. The cathode is the conducting substrate on which electrodeposition is to be done and the anode can be either soluble or inert.

The deposition process involves applying electrical potential by means of a pulsed or direct current source between an anode with a positive pole and a cathode (metal matrix) with a negative pole, which results in an electric current between anode and cathode and the transfer of the ions in electrolyte, completes the circuit [48].

The overall reactions taking place during electrolysis are [47]:



As, in this process, electrons flow from one side to the other across the external circuit, the overall process would represent a separation of charges. Consequently, the difference in potential between the electrodes would have to rise constantly with time in order to sustain electron flow. The flow of ions from one electrode to the other balances the separation of charges. Ion mobility can either be realized by connecting the two electrolyte volumes with an ion-permeable membrane, or by immersing both electrodes in the same solution volume. In nickel electroplating, both the anode and the cathode are usually within a single solution [46].

Ideally, every ion deposited from the solution is replaced by an additional ion entering the solution, and thus, the composition of the solution, which is referred to as the electrolyte, is unchanged. Unfortunately, nature is more complicated. In addition to metal deposition, other side reactions occur at the electrodes, as in every chemical process. In this case, additionally, water decomposes at the cathode:

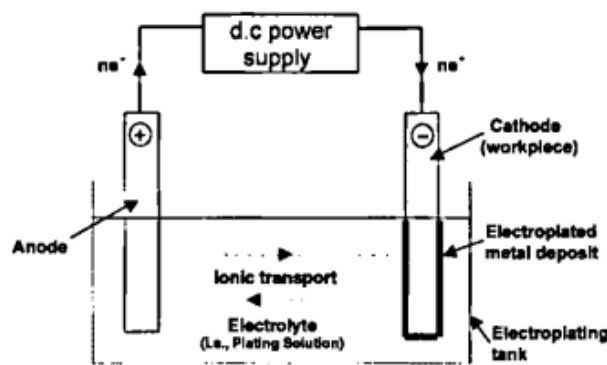
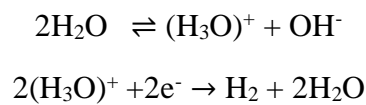


Figure 32: Schematic representation of an electrolytic cell [49].

At the cathode, alongside the metal deposition, the generation of hydrogen gas is also detected. The extent of electrical energy dissipated through hydrogen formation varies based on the electrolysis method employed, typically ranging from 2% to 6% of the total energy utilized. However, in specific processes, this proportion can escalate to as high as 95%. In contrast, the loss of electrical energy in reactions occurring at the anode is generally less than 1% [46].

The obvious consequence of this for the process is that nickel ion concentration increases so that, ideally, regular electrolyte dilution is necessary. In practice, however, a certain electrolyte proportion is lost during the process. The loss is compensated by adding fully demineralized water, so that the added nickel due to unequal current efficiency can even be beneficial.

Moreover, the pH of the electrolyte, which inversely signifies the concentration of H_3O^+ ions, increases as a consequence of the depletion of H_3O^+ ions at the cathode. To counterbalance this reduction in ion concentration, acid is introduced. Furthermore, the hydrogen generated tends to accumulate on the surface of the deposited material, leading to defects in the coating. The presence of gas bubbles acts

as insulators, causing a cessation in nickel deposition in the nearby area. Consequently, this interruption results in the formation of pores within the coating.

Consumption of H_3O^+ ions lead to increased pH around the electrode. This increase, however, promotes formation of metal hydroxide, which precipitates from the solution directly onto the electrode surface.

This effect produces a dull, unaesthetic precipitate. A buffer is added into the electrolyte to neutralize and capture protons in the event of a pH decrease, while also liberating protons in the case of a pH increase. In the process of electrolytic nickel deposition, boric acid is frequently employed to prevent the precipitation of nickel hydroxide [46].

To prevent localized variations in ion concentration, whether they be reduced or increased, it is essential to facilitate adequate exchange of electrolyte at the electrode surface. This can be achieved through continuous operation of circulation pumps or by introducing air into the system. Additionally, the components to be coated are set in motion within the electrolyte to ensure relative movement between the parts and the electrolyte [46].

Effective electrolytes must exhibit strong electrical conductivity, necessitating the incorporation of ions that are particularly adept at conducting electrical energy. For instance, in nickel plating, chloride ions are introduced into the electrolyte to enhance conductivity.

Maintaining uninterrupted ion exchange requires meticulous control of the electrolyte temperature, and the application of a wetting agent ensures proper wetting of the components to be coated.

5.2 Deposition mechanism

The general mechanism consists of two stages of nucleation and growth, comprising of three stages [48]:

1. Transfer of ion from the solution to the surface of the cathode
2. Transfer of the charge and conversion of the ion to the metal atom
3. The diffusion of the metal atom into the crystalline lattice of the metal and grain growth

During the deposition process, a metal ion undergoes initial discharge and is deposited onto the surface as a loosely bound metal atom. The very first atom deposited on the surface must initiate the formation of an entirely new nucleus, given the absence of pre-existing nucleation sites (a process known as nucleation).

A second metal atom, deposited in close proximity to the first, has a choice between forming an additional nucleus or attaching itself to the existing nucleus, thereby contributing to its growth in volume (referred to as nucleus growth) [46]. This intricate process underscores the dynamic nature of metal deposition, involving the sequential phases of nucleation and nucleus growth for the establishment of a stable coating on the surface.

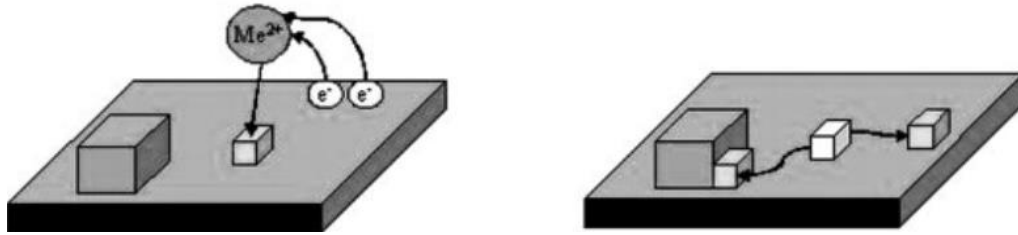


Figure 33: Nickel deposition: initially, the nickel discharges at the surface (left), and subsequently diffuses to the final position (right) [46].

While a combination of high nuclei growth rate with reduced nucleation rate yields a few large crystallites, high rates of nucleation combined with low nucleation growth rates lead to the formation of many small crystals. Coatings with many small, rather than a few large, crystallites typically show considerably less porosity, resulting in increased corrosion protection. The coating is easier to deform and has a brighter surface.

5.3 Type of current

Direct current electrochemical deposition (DC) pulsed electrochemical deposition (PC) and pulse reverse current electrochemical deposition (PRC) which are depicted in Figure 34 are various categories of electrochemical deposition.

In the case of DC current, a continuous flow of electricity facilitates the migration of metal ions from the electrolyte solution to the substrate, resulting in the deposition of a uniform metal coating.

Pulse current (PC) and pulse reverse current (PRC) electrodeposition techniques have recently attracted many researchers for the synthesis of coatings in comparison to the conventional DC electrodeposition techniques.

As compared with the DC electrodeposition, the pulsed electrodeposition offers more process controllable parameters which can be adjusted independently. Moreover, a high pulse current density will accelerate the nucleation rate resulting in fine grains [50]. Pulse electrodeposition, when applied to metal electroplating, yields deposits with a finer grain size compared to those obtained through direct current (DC) electrodeposition [51].

In pulse electroplating, the electrodeposition of nanostructures relies on two primary processes: nucleation rate and the growth of existing grains. Favorable conditions involve factors that increase nucleation rate (such as current density) and hinder grain growth (via inhibiting molecules). In conventional DC plating, the only adjustable parameter is the current density. However, in pulse electroplating, there are at least three parameters to consider: pulse height (current amplitude), relaxation time (t_{off}), and pulse time (t_{on}), all of which can be optimized effectively. Each pulse comprises a t_{on} period during which potential or current is applied, followed by a t_{off} period during which zero current is applied [52].

When a current pulse is applied to the electroplating bath, a negatively charged layer develops around the cathode as the process progresses. In direct current (DC)

electroplating, this layer reaches a certain thickness and impedes ions from reaching the substrate. In pulse electrodeposition, the current output is intermittently turned off, causing this layer to partially discharge. This discharge process facilitates the passage of ions through the layer and onto the substrate more effectively [52].

PC electroplating may be preferred over direct current (DC) because of reduced residual stress, improved wear and corrosion resistance of the film. Alternatively, pulse-reverse current (PRC) plating is a bipolar electrodeposition method where DC is continuously reversing its polarity, with which the pre-deposited film is partially stripped by anodic current [53].

In order to characterize a direct current, it is sufficient to know the current density.

The characterization of a train of current pulses requires three parameters to be known. These are the cathodic peak pulse current density, j_f , the cathodic pulse length, t_{on} ; and the interval between the pulses, t_{off} .

The period and frequency of pulses are expressed as follows:

$$T = t_{on} + t_{off} \quad (10)$$

$$v = \frac{1}{T} \quad (11)$$

In practice average current j_{AV} is measured, and it is expressed in the case of PC as follows:

$$J_{AV} = \frac{j_f \cdot t_{on}}{t_{on} + t_{off}} = \frac{j_f \cdot t_{on}}{T} \quad (12)$$

A quantity frequently encountered is the duty cycle, **d.c.**, representing the portion of time in each cycle when the current is on. It is defined by the following equation:

$$d.c. = \frac{t_{on}}{t_{on} + t_{off}} = \frac{t_{on}}{T} \quad (13)$$

The product of the duty cycle and the peak pulse current density gives the PC average current density.

$$J_{AV} = j_f \cdot d.c. \quad (14)$$

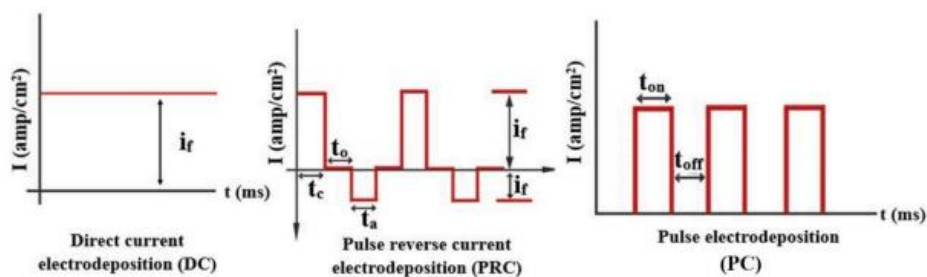


Figure 34: Different types of electrodepositions [54].

Trains of pulses can be programmed to give very complex waveforms. Square waves are the easiest waveforms to produce because this requires only a switching

arrangement rather than a specialized waveform generator. Current waveforms can be divided into two major groups: These are unipolar pulses, where all the pulses are in one direction (PC), and bipolar pulses, where anodic and cathodic pulses are mixed (PRC) [55].

Unipolar pulsed current justified its practical application mainly through its ability to affect the mechanisms of electro-crystallization, which in turn, controls the physical and mechanical properties of the electrodeposited metal. Given that the nucleation rate of a developing electrodeposit is directly proportional to the applied current density, employing high current density pulses has the potential to yield deposits characterized by reduced porosity and, in most instances, a finer grain size. The effects obtained in practice are also dependent on the specific electrochemical system to which a particular set of the current pulses is applied [55].

Considering the effect of t_{on} and t_{off} intervals, during the t_{off} interval, the depleted surface concentration of metal ions on the cathode may be restored through the diffusion of metal ions from the bulk electrolyte, while any by-products formed during the reaction would diffuse away from the cathode surface. During the t_{on} interval, new nuclei are more likely to form due to the elevated surface concentration of nickel ions. Too short t_{off} can lead to insufficient replenish of metal ions to the surface from the bulk, and therefore the low-surface metal ion concentration led to large grain growth. Furthermore, short t_{off} helps the continuous growth of the already-existing grains. Therefore, the electrodeposition condition is similar to the DC. The t_{on} also should be short enough. If the t_{on} duration is large, the electrodeposition conditions would approximate those of constant current electrolysis (DC), potentially resulting in the formation of large grains and the occurrence of side reactions. On the other hand, the t_{on} duration cannot be excessively short. It must be sufficiently long to permit the complete charging of the electrical double layer. Otherwise, the reduction reaction may not initiate properly. Also, the nucleation rate is much lower when too short t_{on} is used [52].

Comparing to DC and PC, PRC plating has several unique advantages, such as reducing concentration polarization, lowering crack density, and eliminating the sealing concern during plating through holes [53].

This method of metal deposition often enables an acceleration of electroplating rates, achieved by employing higher working current densities compared to DC current. Initially, this acceleration is attributed to preventing the depletion of metal ions in the cathode double layer, which is influenced by the anodic dissolution of the deposit. The upper limit of working current densities during metal deposition depends on the parameters of the reversed current (t_a and j_f) and the total period length. Typically, the limiting cathodic current density increases with a rise in the ratio t_a/t_c and a decrease in total time [55].

The higher working current density during Pulse Reverse Current (PRC) deposition, in contrast to DC plating, results from the periodic depolarization of the electrodes. This effect of current reversal on electrode processes, combined with the electropolishing action of the anodic current on the deposit, facilitates subsequent

electro-crystallization on the cathode surface in a preferred direction (resulting in smaller crystal grains) under a higher working (practical) current density. During the cathodic period, this leads to grain refinement typically associated with unipolar pulse current plating, a phenomenon further supported by the disturbance of growth steps due to the periodic inversion of the current [55].

5.4 Additives

Additives are compounds incorporated into the electrolytic bath to influence the properties of coatings. These additives, categorized as organic and inorganic, exhibit distinct functions and fall into the following categories [2], [56]:

1. Carriers: Substances added to the electrolytic bath to facilitate the smooth and uniform deposition of metal onto the substrate. They play a role in improving the leveling and distribution of the metal ions during the plating process. Some commercially available carriers are Sodium methanesulfonate, Octane-1-sulfonic acid sodium salt
2. Brighteners: Substances are introduced into the electrolytic bath to enhance the appearance and quality of the deposited metal coating. Some commercially available brighteners are 2-Butyne-1,4-diol, Ethylene sulfonic acid.
3. Wetting Agents: Additives used to promote a more uniform distribution of metal ions and enhance the overall smoothness of the deposited coating. Wetting agents possess tensioactive properties, aiding in the separation of gas bubbles produced during the hydrogen evolution reaction. Some commercially available wetting agents are Alkyl or lauryl ether sulfate sodium salt

Additives are typically employed in small quantities, with their concentration in the bath ranging between 10^{-4} and 10^{-2} M.

5.4.1 Brightener: 2-butyne-1,4-diol

One of the most commercially available addition agents in Watts type bath for producing bright and levelling nickel deposits is 2-butyne-1,4-diol [57].

2-Butyne-1,4-diol (I), a crystalline solid with a white appearance and a melting point of 57.5°C , was initially synthesized in 1906 through the reaction of acetylenedimagnesium bromide with formaldehyde. It didn't attract much attention until approximately 1940 when a method for its direct synthesis from acetylene and aqueous formaldehyde was disclosed. Following this discovery, butynediol gained significant significance as a valuable product in the German chemical industry during the period of World War II [58].

It is commonly used in the manufacturing of pesticides, corrosion inhibitors, , synthetic resins and polyurethanes. The Boiling point of 2-Butyne-1,4-diol is at 238°C [59].

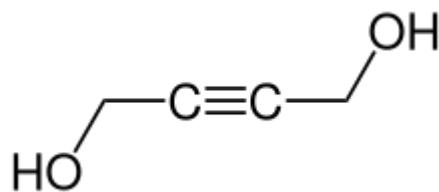


Figure 35: Structural formula of 2-butyne-1,4-diol [60].

It is valued for its ability to influence the electrodeposition of certain metals, such as nickel, by impacting the kinetics of the electrocrystallization process.

Electrochemical investigations into the kinetics of nickel electrocrystallization have demonstrated that 2-butyne-1,4-diol significantly hinders the reduction reactions of nickel when compared to other additives like saccharin and sodium benzene sulfonate [57], [61].

Furthermore, 2-butyne-1,4-diol has shown to affect the preferred orientation of the crystal and the grain size [57].

5.5 Nickel Electrodeposition

The initial account of nickel electrodeposition dates back to G. Bird in 1837, who conducted electrolysis on a solution of nickel chloride/sulfate, resulting in the formation of a metallic nickel crust on a platinum electrode. Subsequently, in 1840, J. Shore of England successfully accomplished commercial nickel plating using a nickel nitrate solution. Nickel plating has proven to be significantly valuable in engineering applications, where its functional performance holds greater importance than its aesthetic qualities [62].

Nickel (Ni) and its alloys offer numerous advantages, including corrosion resistance, wear resistance, and hardness, surpassing other alloys. Consequently, the industrial and scientific communities are drawn to producing nickel into coatings to enhance magnetic properties, improve wear and corrosion resistance, and facilitate part repair of the substrate. For instance, nickel-based coatings are utilized to upgrade the surface quality of various engineering components, including cutting tools, turbine blades, rollers, plungers, rolling mill rolls, extruders, piston heads and rods, as well as wearing plates [63].

5.5.1 Different types of Ni electrolytic baths

1. Sulfate solutions

The most common nickel-plating bath is the sulphate bath known as Watts bath. Watts formulation, which was developed in 1916 by Professor Oliver P. Watts is the basis of the majority of the nickel-plating solutions. This electrolyte is made up of nickel sulphate, nickel chloride and boric acid.

Nickel sulfate serves as the primary source of nickel ions in the electroplating process. The quality of the deposited nickel is influenced by the nickel metal content, which, in turn, determines the limiting current density for achieving desirable deposits. Nickel

chloride contributes to anodic corrosion, enhancing the diffusion coefficient of nickel ions. This effect enables a higher limiting current density. Additionally, boric acid acts as a pH buffer in the electroplating solution. The presence of H₃BO₃ in the Watts electrolyte can impact the nucleation and grain growth of nickel electrodeposits. An adequate concentration of H₃BO₃ enhances the nucleation process of nickel, leading to the formation of a fine and bright nickel coating [64].

The Watts bath has four major advantages compared to the other available baths:

1. Simple and easy to use.
2. Obtained in high purity grades and relatively inexpensive.
3. Less aggressive to equipment (container) than nickel chloride solutions.
4. Deposits plated from these solutions are less brittle and possess lower internal stress than plated from nickel chloride electrolytes.

Details for the bath composition and the operating parameters represented in **Error! Reference source not found.**

Bath composition	Nickel sulfate (NiSO ₄ ·6H ₂ O)	240 – 330 gr/L
	Nickel chloride (NiCl ₂ ·6H ₂ O)	35 - 45gr/L
	Boric acid (H ₃ BO ₃)	30 – 40 gr/L
Operating parameters	Temperature	40-60 °C
	pH	3.5-4.5
	Current density	2-11 A/dm ²
	Deposition rate	25-85 μm / h

Table 3: Details of Watts Ni electroplating solutions.

2. All chloride solutions

Chloride baths offer advantages over sulfate baths in terms of deposition speed and their ability to function efficiently at elevated cathode current densities. Electrodeposits obtained from chloride electrolytes exhibit smoother surfaces, finer grain structures, increased hardness and strength compared to deposits from Watts solutions, and they tend to be more highly stressed [64].

3. Fluoroborate solutions

The fluoroborate solution is versatile, allowing operation across a broad spectrum of nickel concentrations, temperatures, and current densities, and it is relatively straightforward to manage. However, it's important to note that the fluoroborate anion, while providing these advantages, can be corrosive and may corrode materials in contact with the solution [64].

4. Hard Nickel

Developed for functional purposes, this electroplating process is applied in case of demanding regulated hardness, enhanced resistance to abrasion, increased tensile strength, and satisfactory ductility, all achieved without the use of sulfur-containing organic additives. While deposits from this process exhibit slightly higher internal stress compared to those from Watts solutions, there are

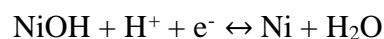
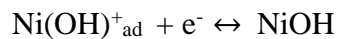
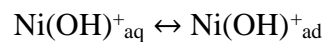
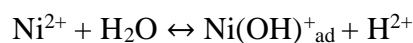
drawbacks, including a tendency to form nodules along edges and a relatively low annealing temperature for the deposits.

5.5.2 Nickel electrodeposition mechanism

In the process of nickel electrodeposition, the application of an external electric field prompts the transfer of electrons along the cathode surface, leading to the reduction of nickel ions into their metallic state. This method can be delineated into three consecutive stages:

1. Nickel ions are transported from the bulk electrolyte to the cathode through mass transport mechanisms encompassing diffusion, convection, and electromigration.
2. Charge transfer occurs at the cathode, resulting in the partial reduction of nickel atoms, which subsequently adsorb onto the surface.
3. Loosely bound nickel atoms then diffuse across the electrode surface to reach active growth sites, where they are integrated into the crystal lattice at kink sites or atomic steps.

Passing electric current to the electrolyte is the primary function of nickel anodes in electroplating. Replacement of nickel ions that have been discharged at the cathode and distribution of current are also major functions of the Ni anode. The following reactions are most probable in the course of Ni deposition, where $\text{Ni(OH)}^+_{\text{ad}}$ denotes an active intermediate.



5.5.3 Current Efficiency

In practice, there is a possibility of secondary electrochemical reactions taking place during electroplating process, which consume a small fraction of the current. Typically, a portion of the current is utilized in the discharge of hydrogen ions from water, leading to the formation of hydrogen gas bubbles at the cathode surface.

The cathode current efficiency is a measure expressed as a percentage, indicating the proportion of current effectively depositing nickel at the cathode relative to the total applied current. Similarly, anode current efficiency refers to the percentage of current contributing to the generation of nickel ions at the anode.

The efficiency of the cathode can vary between 90% and 97% for different nickel solutions, while the anode efficiency for nickel dissolution is consistently close to 100%. Since the cathode efficiency tends to be lower than the anode efficiency, the concentration of nickel ions and the pH of the solution may gradually increase during the operational process [65].

5.5.4 Nickel eclectic orientations

Electron diffraction research has clearly demonstrated that there are several phases in the electro-deposition growth process, with each phase marked by distinct crystal orientations. In the initial or epitaxial phase, the substrate significantly influences the size, shape, and orientation of the deposited crystals. This influence gradually diminishes during the transition phase and becomes negligible in the final growth stage, where a preferred orientation of the deposit crystals takes precedence [66].

In the epitaxial phase, the initial electrodeposited layer inherits the structure or orientation of the substrate when the misfit strain between electrodeposited layer and substrate is less than 12%. This layer is called epitaxial [67].

The main growth pattern of nickel is epitaxial growth and fiber texture growth. Nickel atoms with power field have priorities over the existing lattice locations on cathode surface in the initial stage of electrodeposition, and form film of nickel completely consistent with crystal orientation on cathode surface (epitaxial growth region). The epitaxial growth region of electrodeposited coatings is about 100 nm [68].

After the layer reaches critical thickness, however, fine columnar grains extending along the growth direction are formed, and the deposited crystallographic texture becomes independent of the substrate structure. These microstructures are strongly dependent on the various deposition conditions (the composition of the electrodeposition bath, current density, deposition temperature, orientation or surface morphology of substrate, etc.) [67]. For instance, Ambrard et al. [69] reported that the texture of electrodeposited Ni layer changes greatly from [110] fiber to [100] fiber, and to [210] fiber with an increase in current density.

Nickel s crystallized in a face-centered cubic structure where the most densely packed planes are (111) followed by (200) and then (220). It has been reported that the surface energy of the (111) crystal growth orientation is the lowest when compared with the other crystal orientation for FCC metals, such as the (100) and the (110) planes [52].

Generally, the metal atoms are absorbed on electrode surface, and new crystal can be formed when crystal nucleus is larger than critical nucleation radius. The metal electro-crystallization is a special crystallization process. Newly-generated the metal atoms generated with reduction reaction diffused to crystal lattice or aggregated nucleation on surface of crystal nucleus and then kept on growing in electro-crystallization process [68]

Based on the texture theory of metal electrodeposition, the epitaxial growth and lateral growth models can coexist, and preferential orientation is (111) and (200) crystal planes in the initial stages of nickel electro-crystallization [68].

In these textured deposits, the crystal grains are oriented in a way that a specific crystal direction, known as the preferred orientation axis or texture axis, is perpendicular to the substrate. This alignment is also parallel to both the direction of current flow and the thickness direction of the deposit. While all other atom rows in the deposit crystals have random orientations, exhibiting rotational symmetry about

the texture axis, it is important to note that, in reality, the atom row corresponding to the texture axis does not stand perfectly perpendicular to the cathode surface in all crystallites. Instead, there is a certain degree of deviation from the ideal orientation, resulting in a spread around the mean and only a partial preferred orientation [66].

The specific preferred orientation depends on the conditions of electrodeposition. Factors such as temperature, pH, bath composition, etc., are relevant aspects of the conditions of electrodeposition.

Experimental results have shown the quantitative modification of four different textures, [110], [211], [100], [210], versus the pH of the bath and the current density J .

The [100] orientation is regarded as being characteristic of a rather free growth, where the deposition is considered to occur on a substrate-surface free of adsorbed hydrogen atoms, the three other textures are associated with definite chemical species (H_{ads} , $Ni(OH)_2$, gaseous H_2) which disturb Nickel electrocrystallization [66], [70].

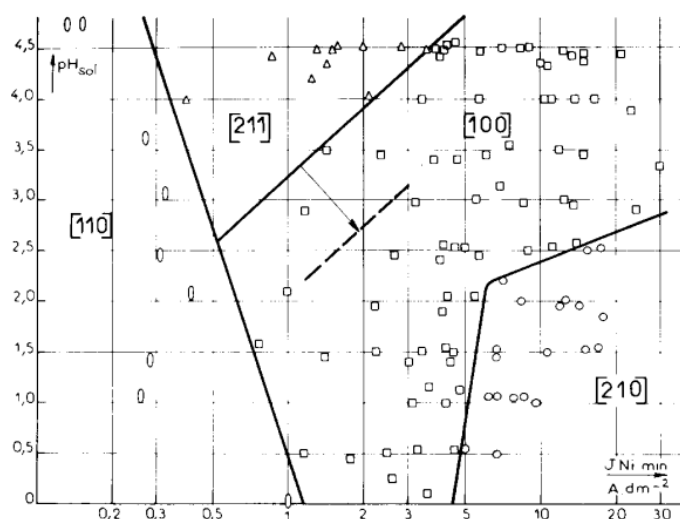


Figure 36: Diagram of textures versus pH and J [70].

According to Pangarov, the texture of a thick deposit results solely from the nucleation step, during which two-dimensional nuclei are formed. The orientation $[hkl]$ of these nuclei corresponds to the minimum formation energy in the specific electrochemical overvoltage domain under consideration. On the contrary, the fundamental assumption of geometric selection theories is that the same texture arises from a competition in growth among various crystallites based on their initial orientation on the cathodic substrate. The selection occurs due to the anisotropy in the growth rates of different crystal planes. According to Reddy and collaborators, this anisotropy depends on the varying extent of coverage of these planes by atomic hydrogen co-deposited at the cathode [70].

Naturally, these two theories consider variations in textures solely based on these parameters. For all face-centered cubic (fcc) metals, the two-dimensional nucleation theory predicts the following sequence:

$$[111] \rightarrow [100] \rightarrow [110] \rightarrow [311] \rightarrow [210]$$

With increasing cathodic overvoltage, the two-dimensional nucleation theory anticipates changes in texture. On the other hand, geometric selection (adapted by Reddy for the case of nickel) predicts texture changes for increasingly unrestricted growth, meaning growth less disturbed by adsorbed atomic hydrogen (H_{ads}) [70].

The favored alignment of grains is determined not only by the velocity and direction of crystal growth but also by the competition among different growth models during electro-crystallization. The "epitaxial growth mode" involves a preference for the orientation of the (110) crystal plane, while the "lateral growth mode" in electrodeposition coatings results in a preference for the orientation of the (100) or (111) crystal plane with face-centered cubic structures [68].

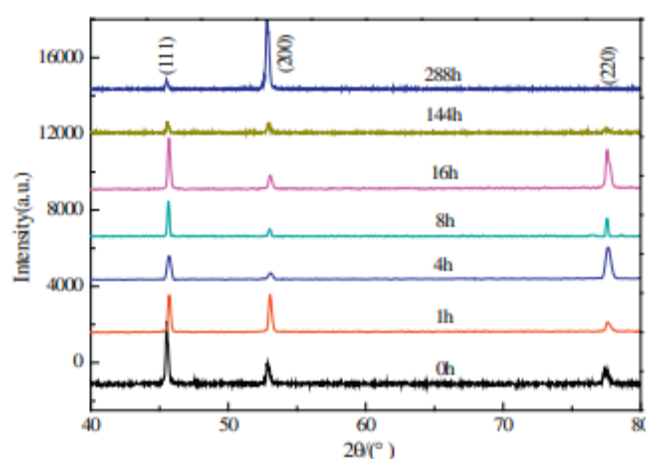


Figure 37: XRD diffraction patterns of electrodeposited coatings of nickel at different deposition time [68].

As shown in **Figure 37** when the electrodeposition time increases, the preferentially growing directions are gradually transformed from (111) and (200) crystal planes to (111) and (220) crystal planes in nickel electro-crystallization. The changes of growing direction are relevant to surface energy and chemical adsorption/desorption of metal crystallization plane [68].

While the electrodeposition time increases, nickel electro-crystallization undergoes a transitional growth phase. Different crystal planes exhibit distinct electrochemical activities and atomic arrangements, leading to varied growth rates. Typically, the atomic density of a crystal plane rises as its electrochemical activity diminishes.

The average grain size of different crystal planes increases with the increase of electrodeposition time, and grain sizes are also different from growth directions [68].

5.6 Composite and nano-composite coatings

In recent times, there has been a significant global interest in the synthesis of composite coatings through electrochemical deposition. This interest stems from the numerous advantages offered by this age-old technique in comparison to other traditional deposition processes. Some of these advantages include [71]:

- Inexpensive technique
- Easy setup installation

- Industrial applicability
- High purity
- Easy to control coating composition
- Higher deposition rates
- Porosity free coatings
- Promising technique to overcome the shape limitations or can deposit on to the complex shapes
- Different substrates can be coated successfully
- Effective to prepare structural features with different sizes ranging from micrometer to nanometer coatings

A coating in which the combination of two or more substances is used to offer protection of substrate is termed as composite coating. This unique type of coating relies on reinforcing particles embedded within the coating matrix. It is manufactured using various techniques to meet the specific needs of industries. These composite coatings provide extra protection against corrosion, wear, and enhance mechanical properties [63]. The electrodeposition involves or allows the reinforcing of a second phase, generally the particles, in the metallic matrix that is electrodeposited from a depositing bath with those dispersed particles, leading to the development of composite coatings and thus to surface protective coatings having enhanced or sometimes totally novel properties.

Dardavila et al., [72] carried out the work on Ni with and without micro ZrO₂ by electrodeposition process direct and pulse current and evaluate the behavior of coatings. The presence of ZrO₂ enhance the overall properties of the coating and the eclectic orientations.

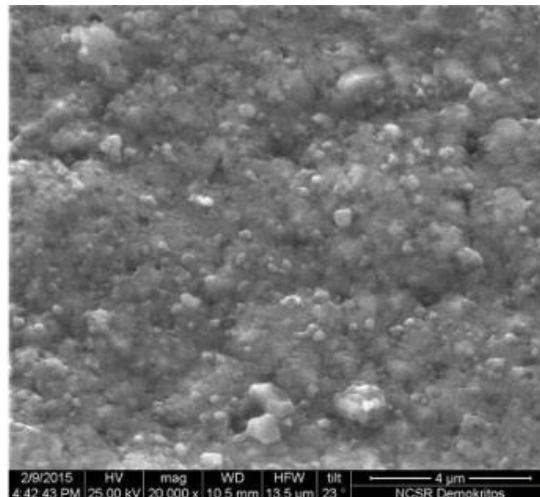


Figure 38: SEM image from Ni- micro ZrO₂ coating. [72]

One of the common mechanisms of co-deposition process have five sequential steps [73] , [74] which are:

1. Initially, the adsorption of ionic species and different molecules happens on the particles surface that are suspended or dispersed in the bath solution.

2. In the next step, the particles are transported toward the hydrodynamic boundary layer through convection process.
3. In the third step, the diffusion of these particles is occurred by a cathode diffusion layer.
4. Subsequently, the particles are adsorbed on the deposit surface.
5. Finally, the solid particles are stuck in the deposit layer through the reduction mechanism of the adsorbed ionic species on their surface, and thus, the particles are incorporated into the metallic matrix as its growth and development begins.

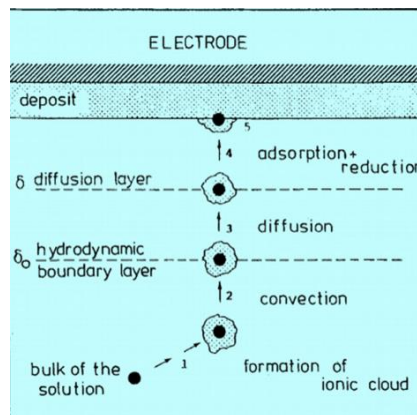


Figure 39: Mechanisms of particle codeposition into a metal deposit [73].

In the process of electrodeposition of nanocomposites, reinforcement particle type, and size and metal -matrix are chosen in order to achieve coatings with the best performance. The distinctive characteristics of nanocomposite coatings are exemplified by a matrix material reinforced by another material in a homogeneous manner. In this arrangement, both components, or at least one of them, exhibit a specific length scale typically in the nanometer range, approximately ranging from 1 to 100 nanometers (nm) [71]. The process parameters are carefully tailored to enhance the strengthening effects conferred by the crystal structure. For example, adjustments to key process parameters such as current density, agitation type, and electrolyte composition are employed with the specific goal of modifying the grain size of the matrix. The composite coating property depends on the size, nature, and type of particles incorporated. This can enhance the basic properties of substrate metal/alloys.

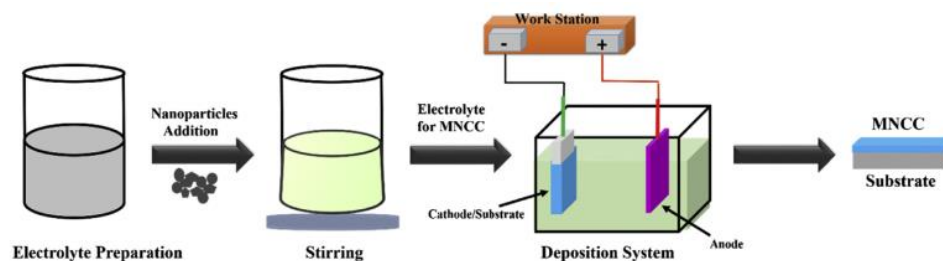


Figure 40: Electrodeposition process of composite coatings [73]

Nickel nanocomposite coatings can incorporate a variety of particles, including oxides, carbides, nitrides, two-dimensional layered materials, and diamond-like carbon (DLC).

The primary challenges associated with the production of nano-particle reinforced composites (nanocomposites) involve the formation of clusters, characterized by the agglomeration of particles, and the non-uniform or inhomogeneous distribution of these nanoparticles within the metal matrix.

The suspension of secondary particles in the bath for nickel nanocomposite coatings can be achieved through agitation or stirring, cathode movement, and the addition of surfactants. Within the bath, these particles will acquire a natural surface charge and zeta potential. The modification of the surface charge, both in terms of its sign and magnitude, can be accomplished through the adsorption of metallic ions and the introduction of surfactants [54].

5.7 Electrodeposition Parameters

The quality and characteristics of the deposited metal layer are intricately linked to various key parameters, including electric current, voltage, electrolyte composition, stirring, pH, current density, type of current, temperature, and plating time.

Moreover, the appearance and properties of the metallic composite coatings can be tailored by adding various additives and also by varying the operating parameters, such as current density, pH, and temperature during the electrodeposition. Further, in the electrodeposition technique, by changing the type of electrodeposition current, different composite coatings can be synthesized with a more uniform distribution of the reinforcing elements in the metal matrix.

5.7.1 Effect of pH

One of the effective factors in the electroplating process is pH.

pH is a determination of a bath's acidity/ alkalinity and is measured on a scale of 1-14 where 1 is acidic, 11 is alkaline and 7 is neutral. The scale is based on the hydrogen ion concentration of the electrolyte by the following expression shown in the following equation :

$$\text{pH} = -\log_{10}[H^+] \quad (15)$$

The value of pH is an important parameter that ensures quality control in electroplating. pH must be held within well-defined limits to guarantee optimum deposition rate. For instance, pH of a nickel Watts bath must be closely around 4.2–4.5 to maintain optimum current efficiency, brightness and levelling properties. The pH value depends upon the composition of the electrolytic bath [54].

Electrolyte pH has a marked effect on cathode and anode current efficiency, i.e., influences the potential at which hydrogen evolves (acidic solutions) or the level and extent of hydroxide precipitation (alkaline baths) [75].

Furthermore, the increased pH leads to metal ion deposition, increased impurities, and residual stress. At lower pHs, the current efficiency is reduced, and the residual stress

also increases, and due to hydrogen attack, the coating becomes prone to pitting. Therefore, at an optimal pH a coating with high-quality and fine grain matrix is formed [48]. Low pH values, less than 5 are selected to obtain the acceptable stress levels [76].

5.7.2 Effect of Temperature

The deposition or solution temperature is considered one of the most important process parameters of Electrodeposition, since it is directly involved in the microstructure, composition, and functional properties of coatings [73].

Generally, in electrodeposition, increasing the bath temperature increases the solubility of metal ions and therefore the transport number which subsequently contributes to an increase in the conductivity of the solution. It also reduces viscosity of the solution rebuilding the double layer comparatively quicker [64]

The temperature of the bath significantly affects the rate at which ions diffuse into the cathode. Maintaining an appropriate temperature is essential for facilitating the delivery of brightener additives to the cathode film and preventing undesirable burning. Simultaneously, the temperature range of the electrolyte bath plays a major role in influencing the physical properties, facilitating mixing, and affecting the response of the additive in the bath components. Higher temperatures lead to higher consumption of the additive, increasing operational costs and potentially causing plating issues. Conversely, lower temperatures result in the precipitation of boric acid, essential component of Nickel electroplating, reducing the efficiency of brighteners. Temperature increases diffusion rate of ions into the cathode film. The volume percentage of reinforced particles within the matrix and the microhardness of the composite coating both rise with increasing temperature, exerting a significant impact on microhardness. [77].

During Nickel electrodeposition, it has been suggested that an increase in bath temperature leads to a decrease in the average surface concentration of adsorbed hydrogen atoms, and thus to changes of textures towards free growth, i.e., ([210]→[100]→[110]). This conclusion is completely in agreement with experiments conducted at a pH less than 5 [78].

5.7.3 Effect of Stirring/Agitation rate

Agitating or stirring the solution enhances the transfer and diffusion rate of metal ions from the bulk solution to the electrode surface. This gradual reduction in the thickness of the diffusion layer helps decrease the formation of gas bubbles, which could potentially lead to pit formation. Consequently, employing bath agitation or stirring is a common practice to achieve a stable and uniformly suspended solution [64].

In the process of composite deposition, the presence and transportation of particles within the bath to the electrode surface are crucially managed through electrolyte mixing. This mixing plays a vital role in determining the solution flow by facilitating the migration and adsorption processes of charged particles. Typically, an increase in agitation leads to a proportional increase in particle deposition. However, excessive agitation can hinder particle co-deposition as the particles are moved away before

forming a stable layer on the cathode surface. Bath agitation gives rise to three distinct flow regimes: laminar, transition, and turbulent [64].

In the laminar regime, rotation speed does not influence the process. In the transition regime, an initial decrease followed by an increase in particle content is observed with increasing agitation, while a continuous decrease occurs in the turbulent regime. When other conditions remain constant, the degree of agitation should vary in proportion to the current density to maintain consistency.

To address coarse-grain defects resulting from impurities in the bath, agitation is followed by filtration in this procedure. Non-uniform dispersion of conductive particles in the bath may contribute to increased coating porosity, introducing porosities from large particle agglomerates and accelerating protrusion growth.

It is noteworthy that ultrasonic-assisted agitation proves beneficial not only in reducing porosity but also in achieving a uniform distribution of nano particles. This improvement enhances the co-deposition rate, resulting in the formation of protective and highly refined coatings. Consequently, the efficiency of the plating process is influenced by the agitation system [64].

5.7.4 Effect of type of current

Electrodeposition of pure metals, alloys, and their composites' coatings are generally carried out using direct current (DC).

In the Direct Current (DC) method, a constant and specific current is employed throughout the coating process. However, a drawback of this approach is the development of residual tensile stresses, leading to the formation of cracks within the deposited layer. To address this issue and enhance current distribution and mass transfer processes, the pulse technique proves to be an effective means of controlling the microstructure and chemical composition of plated coatings. Additionally, this technique resolves various issues such as hydrogen evolution, metallic hydride formation, uneven deposits, and local pH fluctuations. By introducing an anodic current in the form of a reverse pulse during nickel electrodeposition, the pulse reverse method distinctly influences the quality, properties, and chemical composition of the resulting coatings.

As compared with DC electrodeposition, the pulsed electrodeposition offers more process controllable parameters which can be adjusted independently. Moreover, a high pulse current density will accelerate the nucleation rate resulting in fine grains [50].

In PC and PRC electrodeposition techniques, the adjustment of the applied potential, duty cycle, cathodic/anodic pulses, and pulse waveform can alter the surface morphology, elemental composition, and microstructure of the resulting composite coatings. The charging and discharging of the electric double layer around the cathode occur due to the periodic alteration of the current between zero to positive values in the PC mode, and from positive to negative values in the PRC mode. The electric double layer becomes discharged during the zero current in the PC mode and the reverse current in the PRC mode, which reduces the negative ion or solvent

obstructions to the incoming positive ions and allows the positive ions to easily reach the cathode (hence increasing the deposition rate). In addition, the zero current in the PC mode and the reverse current for the PRC mode allow the better penetration and entrapment of the reinforcements in the growing coating [79].

One notable characteristic of pulse electrolysis is its capability to produce high instantaneous current densities, and hence very positive potentials at the anode. The significant increase in overvoltage alters the rate relationship of reactions. Consequently, the application of pulse current has the potential to introduce a novel deposition mechanism [80].

5.7.5 Effect of current density

In general electrodeposition, current density has a prominent influence in determining the rate of deposition. It also regulates the thickness of composite coatings.

The current density plays an important role on the grain size of electrodeposited coatings. In general, high current densities promote the grain refinement. An increase in the current density results in a higher overpotential that increases the nucleation rate. Moreover, when the current density increases, the cluster density can be increased [81].

The quality of the ultimate deposit is dictated by both current density and distribution. In the context of composite deposition, the current density plays a pivotal role in shaping the composition and morphology of secondary-phase reinforced particles within the coatings. The integration of particles into composite coatings is directly contingent on the prevailing conditions within a deposition system. This factor significantly influences the quantity of reinforcement provided by nanosized particles within the metallic matrix, thereby impacting the functional properties of the resulting coatings [73]. Higher electrodeposition overvoltage in composite systems promotes greater grain nucleation and subsequent refinement, leading to the formation of sub-micron and potentially nano-crystalline coatings. Higher current density intensifies nucleation, resulting in smaller grain sizes during composite electrodeposition [64].

5.7.6 Effect of Surfactant

The use of surfactants such as sodiumdodecyl sulphate (SDS), cetyltrimethylammonium bromide (CTAB) and saccharine can enhance the properties and durability of electrodeposited coatings. The key benefit of surfactant addition is their dispersing effect of particles.

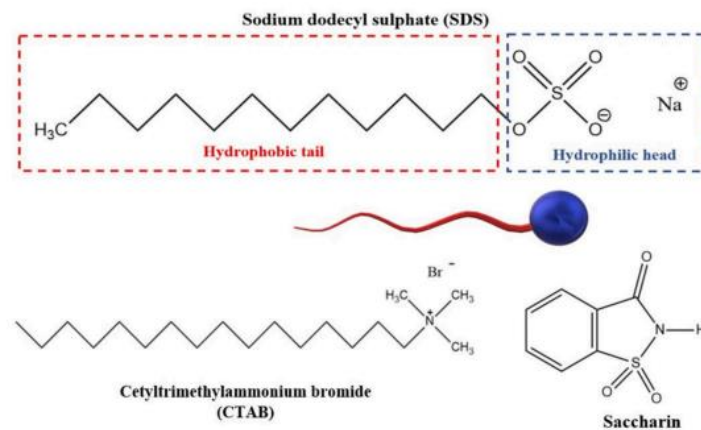


Figure 41: Common Surfactants [64].

Surfactant gets absorbed to the particles and helps in the particle distribution. The surface characteristics of the electrodeposited nanocrystalline nickel are influenced by the surfactants in the Watts bath. By controlling pulse parameters, the grain refinement in a Ni watts bath without saccharin will be about 100 nm whereas in the presence of saccharine it can be around 30 nm [64].

Surfactants can change the surface charge of particles and decrease the agglomeration tendency. Through the adsorption of the surfactant on the surface of the nanoparticles, the surface energy of the nanoparticles can be reduced, and the dispersion of the nanoparticles in the plating solution and plating layer can be effectively improved. The aggregation of nanoparticles is reduced. The concentration of the surfactant in the bath can also affect the composite amount of the particles in the coating [82].

Choosing appropriate surfactant and surfactant concentration can increase the number of nano particles in composite coatings and obtain high quality composite coatings.

5.7.7 Effect of Electrolyte and incorporated particles

Bath concentration influences plating efficiency. An escalation in bath concentration leads to a higher metal ion concentration in the solution during standard plating conditions, consequently boosting the deposition rate of the plating system. Alongside bath concentration, the type of particles involved is a crucial factor. Both conductive and non-conductive particles offer distinct advantages. Conductive particles like molybdenum disulphide, chromium carbide, zirconium diboride, and graphite tend to create rough deposits. It appears that composite coatings constructed with conductive particles that seamlessly integrate into the metallic matrix tend to display an uneven, coarser, and dendritic-like morphology in the deposited structure [73]. These particles are conveyed towards the cathode, serving as points for dendritic growth. On the other hand, non-conductive particles yield smoother and less porous deposits. Smaller particles are easily agitated, and there is a proportional relationship between the concentration of particles and the rate and quantity of their incorporation, up to a certain threshold. In certain instances, the corrosion behavior of electrodeposited

coatings is influenced by factors such as particle content, size, and the homogeneity of the microstructure [64].

5.7.8 Effect of additives and brighteners

Commonly, the presence of additives in metal plating solutions results in an improved leveling effect on the electrodeposited surface. These additives play a crucial role in changing the electrodeposition rate specifically at protrusions and recesses. Additionally, they influence the diffusion of reactants from the solution's bulk to the reaction front by modifying both the properties of the plating solution and the surface diffusion of metal ad-ions or ad-atoms to stable lattice sites. Furthermore, the electrodeposition rate may be heightened by the preferential adsorption of additives or their derivatives onto surfaces with varying curvature [83].

The impact of additives on the physical and mechanical properties of coatings is well-established. The precise mechanisms through which these additives exert their influence is unclear and may involve various interactions at the molecular level. The functioning of additives involves a complex mechanism, and the impact of each additive on deposit properties extends beyond what one might infer from the terminology outlined earlier. It is not rare for a particular characteristic of a coating to arise from the synergistic interaction among two or more additives within a bath of intricate composition. One of the most plausible ways in which additives affect the properties is through adsorption onto the surface [2], [56].

5.7.9 Effect of substrate

The quality of a deposited surface is determined not only by the operational conditions during the electrodeposition process but also by the characteristics of the substrate. Metallic substrates, after manufacturing and grinding, often retain residues such as oxides and oils on their surfaces. If these residues are not adequately removed prior to electrodeposition, they can become trapped between the metallic substrate and the anode. This interference can negatively impact the adhesion of the deposited metal to the substrate, resulting in suboptimal bonding and potentially compromising the overall quality of the coating. Therefore, thorough cleaning and preparation of the substrate surface are essential to ensure effective metal adhesion during the electrodeposition process [2].

EXPERIMENTAL PART

CHAPTER VI: Experimental procedure: Production of Nickel- Matrix nanocomposite coatings

6. Nickel-Matrix nanocomposite coatings

Introduction

In the experimental part of this master's thesis, the electrodeposition process for producing Ni-matrix nanocomposite coatings is comprehensively examined. The selected methodology involves a Ni-Watts electrolyte, with the incorporation of nano-ZrO₂ as reinforcing nanoparticles and the inclusion of 2-butyne-1,4-diol as a brightener-additive. Throughout these experiments, the effects of both direct and pulse currents, at different d.c. , are explored, maintaining consistent conditions of constant current density (J), temperature, stirring rate and pH.

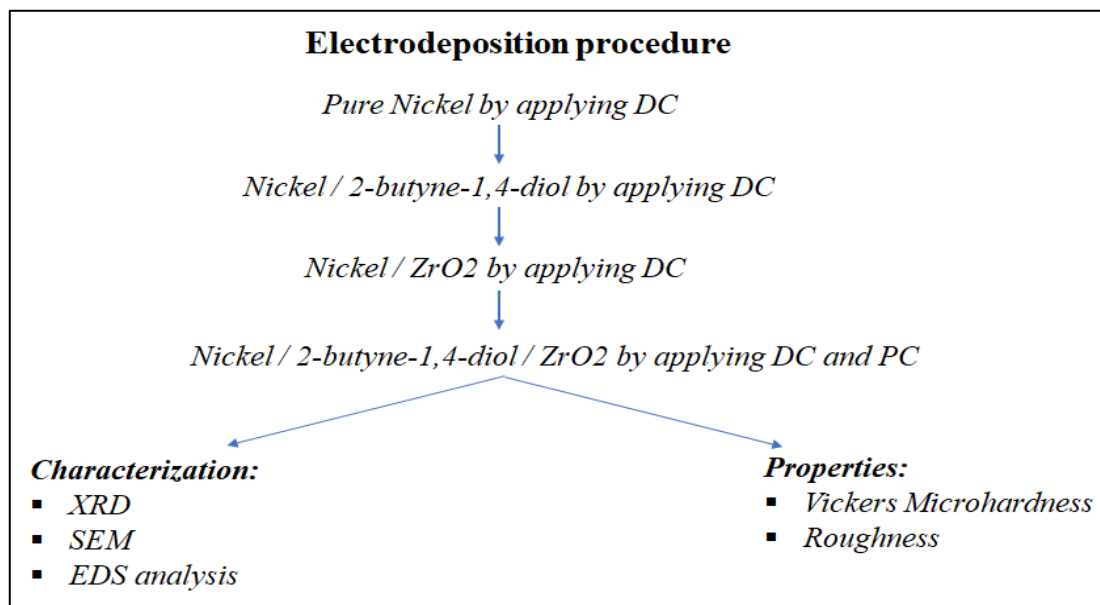


Figure 42: Experimental scheme.

6.1 Experimental Setup

Figure 43 illustrates the experimental setup employed for the production of the nickel matrix coatings.

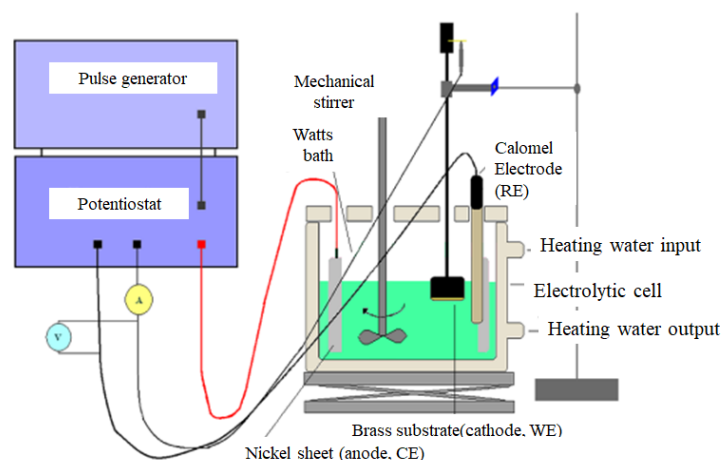


Figure 43: Experimental Setup

The experimental setup consists of:

- **Electrolytic cell:** The electrolytic cell is made of glass with a capacity of one liter and features a double-walled structure for water circulation, ensuring uniform and constant heating. The cell is temperature-controlled using an external water bath circuit with a thermostat set to 50°C ($\pm 0.2^\circ\text{C}$). At this temperature, the entire set of specimens, under study, was prepared. The surface of the electrolytic cell container is covered with a Plexiglas lid, equipped with suitable openings for the introduction of electrodes, serving both to limit the evaporation of the electrolytic bath and to protect against the inadvertent introduction of impurities. The pH of the bath was monitored at the beginning and end of each deposition, consistently adjusted to a value of 4.5 by adding the corresponding solutions of ammonia or sulfuric acid. The pH control of the electrolytic bath was conducted using a digital pH meter.

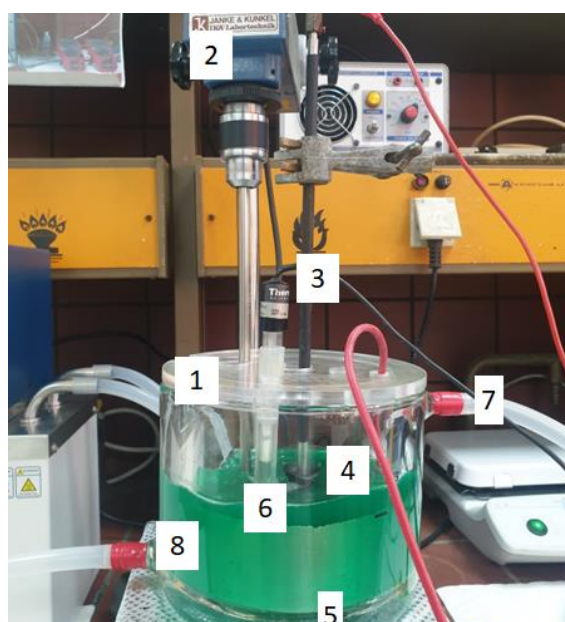


Figure 44: Electroplating setup: (1): electrochemical cell, (2): mechanical stirrer, (3): Calomel (RE), (4): Cathode (WE), (5): anode (CE), (6): Watts Bath, (7): Thermic water input, (8) Thermic water output.

- **Potentiostat:** The potentiostat used for applying potential in the circuit is from BANK Elektronik, model Wenking ST88. It comes equipped with a built-in analog ammeter with a scale ranging from 0.1mA to 3mA. The applied potential and the current intensity flowing through the electrolytic cell are monitored, respectively, by a voltmeter, connected in parallel to the circuit, and an ammeter, connected in series with the circuit.
- **Pulse generator:** During electrolytic deposition under pulsed current conditions, the pulse generator of BANK Elektronik, model Wenking DPC 72, is activated and connected to the potentiostat. This generator has the capability to produce single or double square pulses, the characteristics of which (height, width, frequency, and polarity) are manually adjustable. Each imposed pulse is superimposed on an adjustable continuous potential (offset) of specific height, width, and polarity. The imposed values for the constant potential offset, as well

as the superimposed pulses, can be varied from 0V - ± 10 V. The width of the square pulses can take values within the range of 1ms-100ms, consequently allowing the duty cycle of the pulse current to fluctuate from 0 to 99%. The time duration of the potential offset can be adjusted between 10ms and 1000ms, thereby enabling the applied pulsed current frequency to range from 0.01Hz to 100Hz.



Figure 45: Potentiostat (down), Pulse generator(up)

6.2 Pre-treatment of samples

The substrates utilized in this study were brass cylindrical samples with a diameter of 25mm and a height of 15mm.

- Smoothing and Polishing:

Initially, the free deposition surface of the specimens is not smooth due to machining processes in the workshop. Therefore, it is essential to smooth and polish this surface to achieve optimal adhesion of nickel electroplated coatings and, at the same time, to limit the substrate's adhesive action during the initial phases of deposit development. Smoothing is initially carried out using abrasives of decreasing grit size on a sanding device. In this way, the substrate for metallization attains controlled roughness, bearing oriented striations. Subsequently, it is polished with specialized cloth brushes on a polishing machine, thereby eliminating any irregularities and protrusions. Finally, using velvet brushes, the specimen is polished, and its surface for coating becomes smooth as a mirror. Before each smoothing and polishing stage, the brushes of the polishing machine are lubricated with a suitable lubricant.

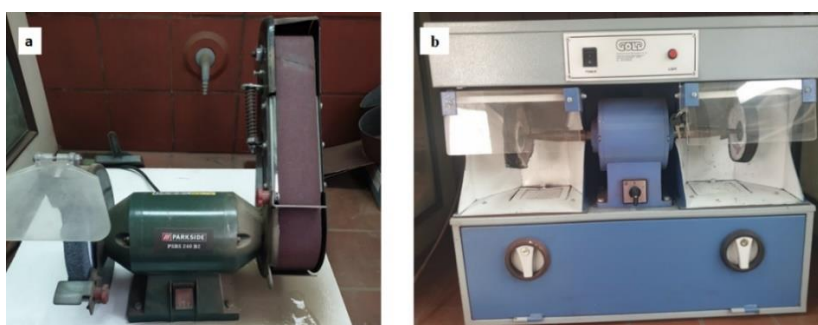


Figure 46: (a) Grinding tool, (b) polishing machine.

- Ultrasonic Bath Cleaning:

It is essential to remove impurities accumulated on the surface of the specimens due to the overall processing that has taken place. This cleaning procedure takes place in an ultrasonic bath for approximately 5-7 minutes, starting with acetone and concluding with deionized water.



Figure 47: Ultrasonication bath.

- Insulation:

Before utilizing each specimen as a substrate, it is necessary to insulate its lateral surface to prevent metallization. For this purpose, a thermoplastic polymer with a circular cross-section, having a diameter approximately equal to that of the specimen, is employed. The material from which it is composed is resistant to the conditions under which nickel plating is performed.



Figure 48: Samples before (left) the pre-treatment , after (middle) the pre-treatment, after (right) the electrodeposition

6.3 Produced coatings

During the present master's thesis, Table 5 presents the electrolyte that was used. The electrolyte was a Nickel Watts bath with the usual amounts of Nickel salts ($\text{NiSO}_4, \text{NiCl}_2$) and boric acid (H_3BO_3).

Ni-Watts Electrolyte	
NiSO ₄ ·6H ₂ O	300gr/L
NiCl ₂ ·6H ₂ O	35gr/L
H ₃ BO ₃	40gr/L

Table 4: Ni-Watts electrolyte that was used for the production of coatings.

Table 5 presents the experiments of the electrolytic deposition of Nickel that were carried out, for the production of simple, composite, and nanocomposite coatings. It should be noted that all coatings produced at $J=5 A/dm^2$, pH=4.5, stirring rate=600rpm and T=50°C. These conditions have been found to yield beneficial results and produce dense, compact, and high-quality coatings [72], [57], [2].

Sample	C ₂ butyne-1,4diol (mmol/L)	ZrO ₂ (gr/L)	Type of current	d.c.(%)	Frequency (Hz)
Ni1	0	0	DC	100	-
Ni_0.5BD	0.5	0	DC	100	-
Ni_1BD	1	0	DC	100	-
Ni_2BD	2	0	DC	100	-
Ni_0.5Z	0	0.5	DC	100	-
Ni_1Z	0	1	DC	100	-
Ni_2Z	0	2	DC	100	-
Ni_4Z	0	4	DC	100	-
Ni_6Z	0	6	DC	100	-
Ni_8Z	0	8	DC	100	-
Ni1_0.5BD_8Z	0.5	8	DC	100	-
Ni2_0.5BD_8Z	0.5	8	PC	90	0.01
Ni3_0.5BD_8Z	0.5	8	PC	70	0.01
Ni4_0.5BD_8Z	0.5	8	PC	50	0.01
Ni5_0.5BD_8Z	0.5	8	PC	30	0.01
Ni1_1BD_8Z	1	8	DC	100	-
Ni2_1BD_8Z	1	8	PC	90	0.01
Ni3_1BD_8Z	1	8	PC	70	0.01
Ni4_1BD_8Z	1	8	PC	50	0.01
Ni5_1BD_8Z	1	8	PC	30	0.01
Ni1_2BD_8Z	2	8	DC	100	-
Ni2_2BD_8Z	2	8	PC	90	0.01
Ni3_2BD_8Z	2	8	PC	70	0.01
Ni4_2BD_8Z	2	8	PC	50	0.01
Ni5_2BD_8Z	2	8	PC	30	0.01

Table 5: Conditions of simple, composite and nanocomposite coatings.

In this master's thesis, the experimental process commenced with the preparation of Nickel Watts electrolyte, with a total volume of 700mL, as described in **Table 4**.



Figure 49: Ni-Watts electrolyte components: (a) Nickel sulfate ($\text{NiSO}_4 \cdot 6\text{H}_2\text{O}$), (b) Nickel chloride ($\text{NiCl}_2 \cdot 6\text{H}_2\text{O}$), (c) Boric acid (H_3BO_3)

Then, the Ni-only electrodeposition took place, serving as the baseline sample. Subsequently, 2-butyne-1,4-diol was introduced at three distinct concentrations to act as a brightener, aimed at enhancing the appearance and overall properties of the coating. Following this, a composite Watts electrolyte, with a total volume of 700mL, was formulated, varying in nano-ZrO₂ concentrations (0.5, 1, 2, 4, 6, and 8 gr/L), with the primary objective of investigating the coating properties and Zr content. Additionally, it is important to note that with the introduction of Zr, the surfactant SDS was incorporated at a ratio of SDS:ZrO₂ 2:1. This adjustment was made to facilitate improved dispersion of the nanoparticles, contributing to a more homogeneous and stable electrolyte solution.

Upon identifying the most promising sample with an optimal Zr content, the nano-ZrO₂ concentration was maintained at a constant level (8gr/L). Subsequently, 2-butyne-1,4-diol was incorporated into the electrolyte. Each of these samples underwent a comprehensive study under both direct current (DC) and pulse current (PC) conditions. This systematic approach allowed for a detailed examination of the impact of each 2-butyne-1,4-diol and ZrO₂ on the coating properties, and the impact of their combination.

CHAPTER VII: Characterization and analysis techniques

7. Methods of characterization and analysis

Introduction

The characterization of coatings includes various advanced techniques for understanding surface properties, structural composition, morphology, and mechanical properties. This comprehensive analysis employs diverse methods such as X-ray Diffraction (XRD), Scanning Electron Microscopy (SEM), and Energy Dispersive X-ray Spectroscopy (EDS) to scrutinize the surface, structure, and morphology of the coatings. Additionally, mechanical properties are assessed using Vickers microhardness and surface roughness tester.

7.1 Scanning Electron Microscopy (SEM)

Scanning Electron Microscope is an advanced microscopy technique that uses electron beams to create high-resolution images of the surface morphology of samples. These high-energy electrons interact with the sample, producing signals like secondary electrons, backscattered electrons, and X-rays. Detectors capture these signals, generating detailed images and data.

The SEM apparatus is comprised of the following elements [84]:

- An electron gun, responsible for producing high-energy electrons.
- A downward column that guides the electrons through two or more electromagnetic lenses.
- A deflection system comprising scan coils.
- An electron detector is designed for both backscattered and secondary electrons.
- A dedicated chamber for accommodating the sample.
- A computer system equipped with a viewing screen for presenting scanned images and a keyboard for managing electron beam control.

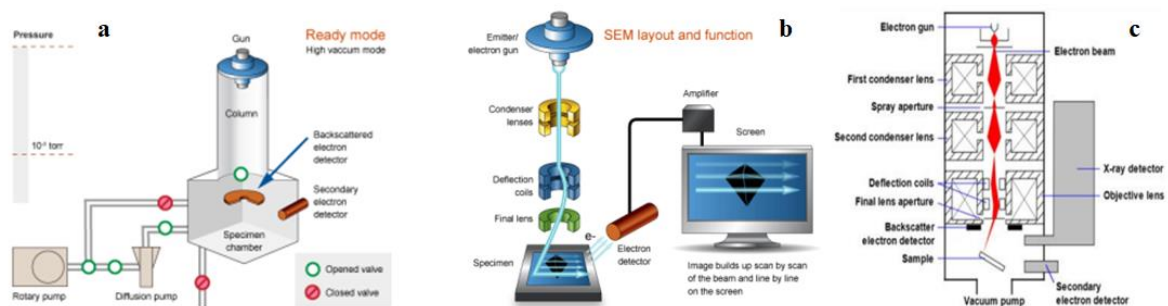


Figure 50: SEM system: (a) Electron detectors in the SEM system, (b) . All SEM components, (c) Schematic of scanning electron microscope (SEM) [84].

SEM serves as a tool to unveil the hidden worlds of microspace and nanospace, exposing intricate details and complexities beyond the reach of light microscopy. This is achieved through the following steps [84]:

a. Electron Beam Application:

The analysis involves applying a high-energy electron beam in the range of 100 to 30,000 electron volts, typically emitted from a thermal source.

b. Spot Size Refinement:

To generate a sharp image, the SEM is equipped with lenses that compress the electron beam spot. Most SEMs have a spot size of less than 10 nm, with electrons interacting with the specimen and penetrating to a depth of 1 μm , generating signals for image production.

c. Image Formation:

The specimen's image is formed point by point as the electron beam moves to discrete locations in straight lines, creating a rectangular raster on the specimen's surface. The entire process depends on the required magnification, with scan coils adjusting the beam for higher magnification.

d. Electron Detection:

Electron detectors are employed to detect emitted electrons (signals) from the scanned sample. Both secondary electrons (SE) and backscattered electrons (BSE) are utilized in SEM image production, collected based on the voltage applied to the collector screen.

e. Signal Display and Control:

Signals are displayed on the viewing screen, allowing the operator to control brightness and intensity until a clear image is obtained. For small details, magnification beyond 10,000x may be applied.

f. Electron Voltage Mode:

The emitted electron voltage mode influences the provided details. Low accelerating voltages (less than 5 kV) result in a surface-rich image, while high accelerating voltages (15-30 kV) penetrate beneath the surface, revealing interior details.

g. Three-Dimensional Image and Topography:

The partly three-dimensional image from SEM depends on visualizing the sample's topography in terms of shape, size, and surface texture. The number of BSE and SE, influenced by the angle of inclination or tilt angle of the sample surface, directly impacts topographic contrast. An inclination beyond 50° to 70° enhances both BSE and SE signals to their peak.

7.2 Energy Dispersive X-ray Spectroscopy (EDS)

Energy Dispersive X-ray (EDX) is a valuable nondestructive tool for characterizing material composition, widely employed in tandem with Electron Microscopy to analyze the elemental composition and microstructure. It is often employed in conjunction with scanning electron microscopy (SEM) or transmission electron microscopy (TEM). Its applications extend to investigating nanometal oxides and play a central role in materials science, connecting with disciplines such as physics, biology, geology, and mineralogy. EDX's versatility is evident in its integration with various analytical tools, making it crucial in chemical industries for manufacturing fertilizers, acids, polymers, drugs, metals, and nanomaterials. Technological advancements enable the effective analysis of diverse nanomaterials and lightweight elements through Energy Dispersive X-ray Spectroscopy (EDS) or EDX [85].

EDS serves as a tool for determining elemental composition and conducting X-ray mapping. Each atom's distinctive electronic configuration is a key factor. When a sample is bombarded with high-energy electrons (X-ray or gamma-ray), inner-shell electrons being knocked out create electron vacancies. Subsequently, electrons transition from higher to lower energy levels, releasing energy in the form of X-rays. EDS detects these characteristic X-rays, and by measuring their energy and intensity, the elemental composition of the sample can be estimated. If incident photons carry an exciton, the resulting X-rays are identified as fluorescent X-rays [85].

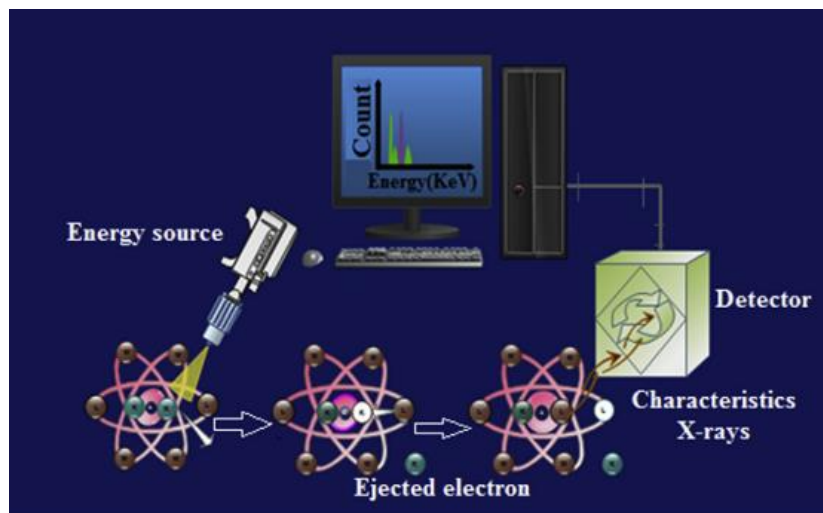


Figure 51: Description of energy-dispersive X-ray spectroscopy principle. An incoming X-ray Description of energy removes an inner shell electron, generates a vacancy, and fills this vacancy by an outer shell electron, delivering a photon [85].

7.3 X-ray Diffraction (XRD)

In 1912, Max von Laue and his colleagues made the discovery that crystalline substances can serve as three-dimensional diffraction gratings for X-ray wavelengths, mirroring the spacing of planes within a crystal lattice. X-ray diffraction (XRD) stands out as a potent and nondestructive technique for characterizing crystalline materials. This method yields crucial insights into structures, phases, crystal orientations (texture), and various structural parameters, including average grain size, crystallinity, strain, and crystal defects. The appearance of X-ray diffraction peaks results from the constructive interference of a monochromatic X-ray beam scattered at specific angles by each set of lattice planes in a sample. The intensities of these peaks are influenced by the distribution of atoms within the lattice, making the X-ray diffraction pattern a distinctive identifier of the periodic atomic arrangements in a given material [86].

The interaction between incident rays and the sample results in constructive interference, leading to the generation of diffracted rays, adhering to Bragg's law:

$$n\lambda = 2d\sin\theta \quad (16)$$

In this equation, n represents an integer, λ is the X-ray wavelength, d is the interplanar spacing causing diffraction, and θ is the diffraction angle. This law establishes a

connection between the wavelength of electromagnetic radiation, the diffraction angle, and the lattice spacing in a crystalline sample. The diffracted X-rays are then captured, processed, and quantified.

To cover all potential diffraction directions of the lattice due to the random orientation of powdered material, the sample is scanned through a range of 2θ angles. Conversion of diffraction peaks into d-spacings facilitates the identification of compounds, as each compound possesses a distinct set of d-spacings. Typically, this identification is achieved by comparing d-spacings with standard reference patterns.

X-ray diffractometers consist of three essential components: an X-ray tube, a sample holder, and an X-ray detector. X-rays are generated in a cathode ray tube by heating a filament to produce electrons, accelerating these electrons toward a target by applying voltage, and bombarding the target material. Characteristic X-ray spectra, including $K\alpha$ and $K\beta$ components, are produced when electrons dislodge inner shell electrons of the target material. Filtering, using foils or crystal monochromators, is necessary to generate monochromatic X-rays for diffraction.

The common target materials include Cu, Fe, Mo, and Cr, each with characteristic wavelengths. Copper (Cu) is frequently used for single-crystal diffraction, with $CuK\alpha$ radiation at 1.5418 Angstrom. Collimated and directed onto the sample, these X-rays are reflected, and their intensity is recorded as the sample and detector undergo rotation. When the geometry aligns with Bragg's law, causing constructive interference, a peak in intensity emerges. A goniometer, an instrument for maintaining the angle and rotating the sample, is crucial for the geometry of X-ray diffractometers. The X-ray detector, mounted on an arm, collects the diffracted X-rays and rotates at an angle of 2θ . The recorded X-ray signal is processed, converted to a count rate, and then output to devices like printers or computer monitors [86].

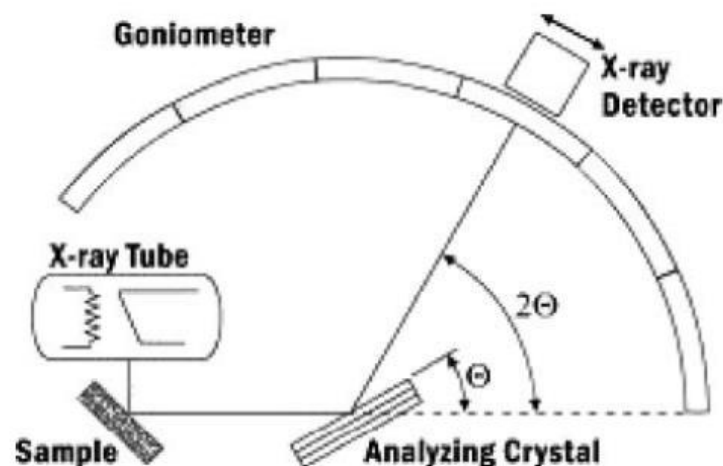


Figure 52: Schematic diagram of a diffractometer system [86].

For the determination of the deposits preferred crystalline orientation, as well as for the evaluation of the quality of this orientation the term Relative Texture Coefficient ($RTC_{(hkl)}$) is used, defined as:

$$RCT_{(hkl)} = \frac{I_{s(hkl)}/I_{p(hkl)}}{\sum_{i=1}^6 I_{s(hkl)}/I_{p(hkl)}} \times 100\% \quad (17)$$

Where, the $I_{s(hkl)}$, $I_{p(hkl)}$ are the diffraction intensities of the (hkl) plane measured in the diffractogram for the deposit and the standard Ni powder sample, respectively.

The grain size was calculated by Scherrer's formula:

$$D = \frac{K \cdot l}{B \cdot \cos q} \quad (18)$$

where D is the average thickness of the grain perpendicular to the crystal plane, B is the width of the half peak height of the diffraction peak of the measured sample, q is the Bragg angle, l is the X-ray wavelength (1.5406 Å) and K is the Scherrer constant.

7.4 Vickers Microhardness

The Vickers indentation test is a widely employed technique for assessing material hardness. This method is straightforward to conduct, requiring a small quantity of material, and is typically non-destructive, allowing for repeated testing. This technique involves creating an indentation on the material's surface using a precisely shaped diamond indenter, and the hardness value is determined based on the size of the resulting indentation [87].

Microhardness testing involves creating an indentation on a specimen using a diamond indenter and applying a load (P) as illustrated in **Figure 53**. The size (d) of the resulting indentation is measured using a calibrated optical microscope, and hardness is determined as the mean stress beneath the indenter. This method, dating back over 50 years, was initially used for small components and has since been extended to study various properties in metallic and ceramic materials, even at temperatures up to 1000°C [88].

In Europe, the pyramidal Vickers-type indenter with an interfacial angle of 136 degrees is commonly preferred, producing a square impression. While general engineering uses test loads of 5-100 kgf, microhardness testing typically employs loads in the range of 1-100 gf (1 gf = 9.81 mN). Rigorous control and replication of microhardness tests are essential, necessitating a strain-free, electropolished specimen surface that is flat and perpendicular to the indenter axis [88].

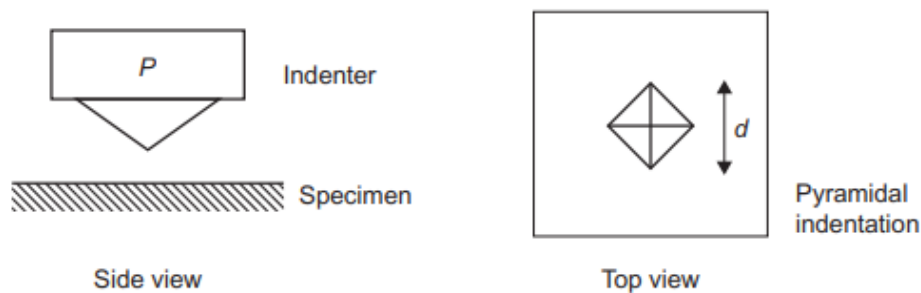


Figure 53: Schematic of indentation [88].

The indenter is slowly lowered at a rate of less than 1 mm/min under vibration-free conditions, causing deformation on the test surface akin to steady-state creep. This condition is achieved within 15 seconds, a commonly used test period. The Vickers hardness (HV) is calculated using the following equation:

$$H_V = 1854.4 (P/d^2) \text{ kgf mm}^{-1} \quad (19)$$

7.5 Surface Roughness Tester

Surfaces exhibit irregularities of different magnitudes, spanning from deviations in shape to irregularities comparable to interatomic distances. Despite the precision of machining methods, it is impossible to achieve a surface that is molecularly flat using conventional materials. Even exceptionally smooth surfaces, like those achieved by cleaving certain crystals, harbor irregularities whose heights surpass the interatomic distances. In technological applications, the surface texture, encompassing both macro- and micro/ nanotopography, holds significance [89].

Nano- and microroughness arise from surface fluctuations with short wavelengths, featuring hills (asperities or local maxima) and valleys (local minima) of varying amplitudes and spacings, which are significantly larger than molecular dimensions. Asperities are termed peaks in a two-dimensional profile and summits in a three-dimensional surface map. Inherent to the production process, nano- and microroughness encompass features like traverse feed marks and other irregularities within the limits of the roughness sampling length.

Waviness represents surface irregularities with longer wavelengths and is known as macroroughness. Factors such as machine or workpiece deflections, vibration, chatter, heat treatment, or warping strains can contribute to waviness. It encompasses irregularities with spacings greater than the roughness sampling length but less than the waviness sampling length.

The principal direction of the predominant surface pattern, typically determined by the production method, is referred to as the lay. Flaws are unintended interruptions in the texture, considered unexpected and undesirable. Moreover, the surface may exhibit substantial deviations from the nominal shape with very long wavelengths, termed errors of form, which are not typically regarded as part of the surface texture.

The assessment of surface roughness is commonly performed in two-dimensional sections and is quantified using parameters like RZ, Rt, and Ra. Ra is considered the most dependable among these values, and as a result, surface roughness is typically expressed using this parameter. When the total length covered by the roughness detector's stylus on the metallic surface is denoted as l_m , it is subdivided into a finite number of potentially equal segments called steps, I_c , typically set at 5.

Surface roughness is characterized and quantified using several parameters, including R_a , R_z , and R_t .

- R_a (Total Average Roughness): R_a is the arithmetic average of the absolute values of the deviations of the surface profile from the mean line within a specified sampling length. R_a represents the average roughness of the surface, providing an

indication of the overall height variations. Smaller R_a values indicate a smoother surface.

$$R_a = \frac{1}{l_m} \int_0^l |y(x)| \cdot dx \quad (20)$$

- R_z (Average height): R_z measures the average of the five highest peaks and the five deepest valleys within a sampling length. R_z focuses on the extreme height variations on the surface, offering insights into the most significant irregularities.

$$R_z = \frac{1}{l_c} (\sum_{i=1}^5 R_{zi}) \quad (21)$$

- R_t (Total maximum roughness): R_t represents the total height difference between the highest peak and the deepest valley within the entire measuring length.

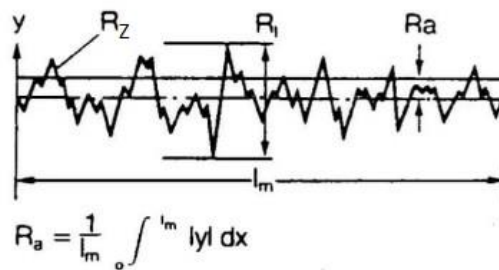


Figure 54: Arithmetic mean roughness value R_a [90].

The roughness value of each specimen represents the average R_a values where the corresponding R_z and R_t do not exhibit significant deviation.

CHAPTER VIII:
Experimental Results-
Characterization of coatings

8. Presentation of experimental results

Introduction

The experimental results presented in this chapter focus on the production of composite and nanocomposite coatings, of 25 μ m thickness, using the brightener 2-butyne-1,4-diol and nano-ZrO₂ as reinforcing means. The coatings were produced by applying both direct and pulse current at various duty cycles (30%, 50%, 70%, 90%). Throughout the experimental procedure, the current density (J), the temperature, pH, and stirring rate were maintained at 5 A/dm², 50°C, 4.5, and 600 rpm, respectively. The frequency during pulse current was set at 0.01 Hz.

First, the current efficiency is a technique for characterizing electroplating processes. It measures the effectiveness of the electrochemical process in depositing metal onto a substrate concerning the amount of electrical current applied. Current efficiency is defined as the ratio of the actual amount of metal deposited at the cathode (the surface being plated) to the theoretical amount of metal that should be deposited according to Faraday's law of electrolysis.

The X-ray diffraction (XRD) analysis revealed a noticeable change in the Ni-Matrix crystal growth with the addition of 2-butyne-1,4-diol. This suggests that this additive has an impact on the crystal structure of the composite and nanocomposite coatings. Also, the change in the Ni-Matrix crystal growth is obvious by adding nano-ZrO₂.

Scanning Electron Microscopy (SEM) was employed to further investigate the morphological changes in the crystallites. The results from SEM clearly illustrate the alterations in the crystalline structure induced by the presence of 2-butyne-1,4-diol and nano-ZrO₂.

Furthermore, Energy Dispersive X-ray Spectroscopy (EDS) was employed to analyze the elemental composition of the coatings. The EDS results provide evidence of the presence of nano-ZrO₂ incorporated into the coating. The elemental mapping and analysis confirmed the successful incorporation of ZrO₂ at the nanoscale within the composite and nanocomposite coatings.

Additionally, the microhardness values obtained from the experiments indicate an enhancement in the mechanical properties of the coatings. This improvement in microhardness suggests that the addition of 2-butyne-1,4-diol and the incorporation of nano-ZrO₂ contributes positively to the overall mechanical strength of the composite and nanocomposite coatings.

In summary, the experimental results provide compelling evidence of the impact of 2-butyne-1,4-diol and nano-ZrO₂ on the crystal growth, morphology, and mechanical properties of the Ni-Matrix coatings. The combination of direct and pulse current at different duty cycles also plays a significant role in influencing these properties.

8.1 Current efficiency

Current efficiency is calculated using the following formula:

$$\text{Current Efficiency (\%)} = \frac{\text{Actual Weight of Deposited Metal}}{\text{Theoretical Weight of Deposited Metal}} \times 100$$

The actual weight of the deposited metal is usually determined by weighing the plated object after the electroplating process. The theoretical weight is calculated using Faraday's law (Eq. 8) and the molar mass of the metal being deposited.

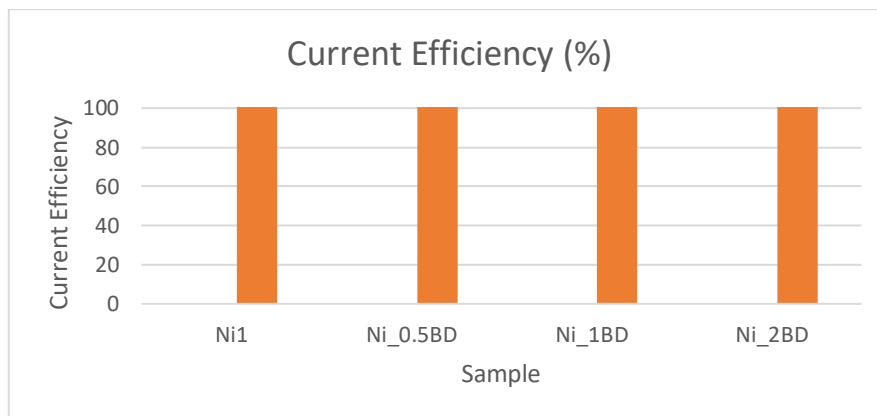


Figure 55: Current Efficiency for Nickel only coating and for composite coatings with three different concentrations of the brightener.

It's clear from Figure 55 that the electrodeposition had been successful. Current efficiency is steady with the introduction of the brightener in the electrolyte and remained in the highest value of 100%. This observation suggests that the applied electrical currents were utilized with utmost efficiency, resulting in a uniform deposition of metal ions onto the substrate.

Continuing with Figure 56, of nanocomposite coatings, the current efficiency remains high, again achieving its maximum value of 100%. While a slight reduction is noted in coatings with concentrations of 2, 4, and 6 g/L of nano-zirconia, all observed values indicate a successful electrodeposition process.

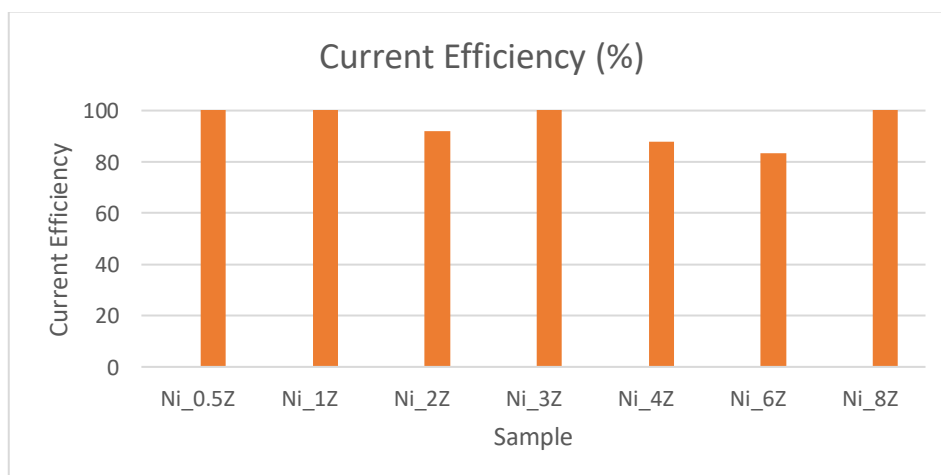


Figure 56: Current Efficiency for Nickel-Matrix nanocomposite coatings using nano-ZrO₂ as reinforcing means.

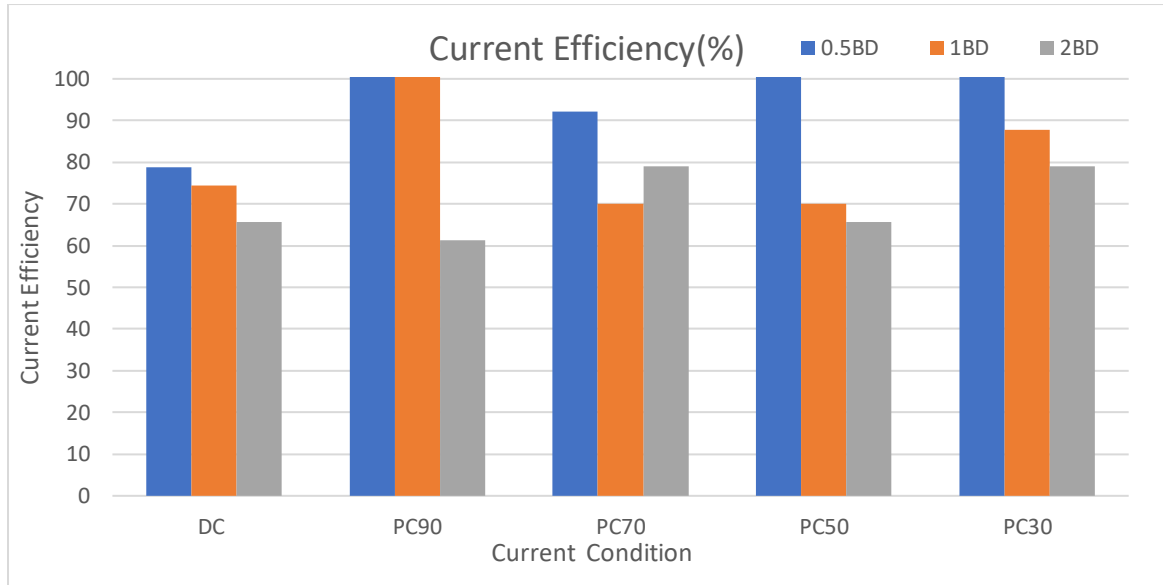


Figure 57: Current Efficiency for Ni-Matrix nanocomposite coatings, under DC and PC condition.

8.2 XRD analysis of composite and nanocomposite coatings

The samples under investigation were analyzed using the X-ray diffraction (XRD) technique with the XRD 5000 SIEMENS instrument. The anticathode employed in this analysis was composed of copper (Cu, $K\alpha$)

First, the XRD pattern for the pure Nickel coating is presented as a baseline. The preferred orientation observed is Ni(200), that aligns with literature suggestions [72], [91] [92].

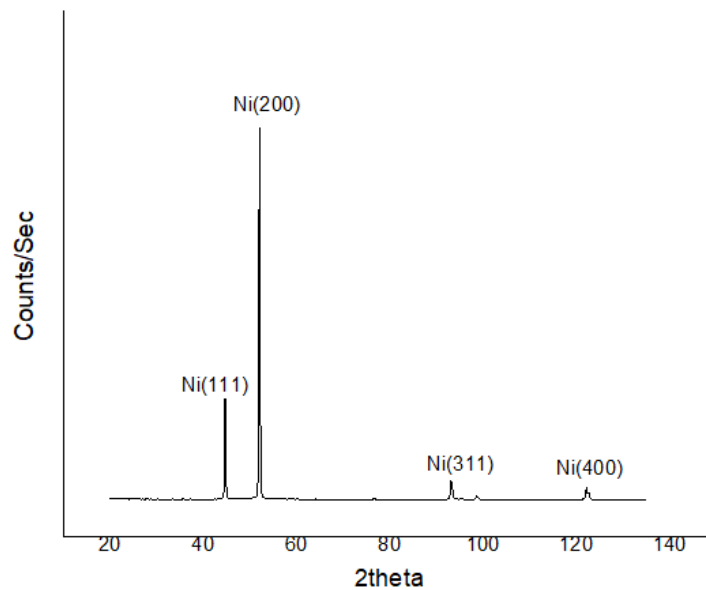


Figure 58: XRD pattern for pure Nickel coating.

With the addition of 2-butyne-1,4-diol, there is a noticeable shift in the preferred orientation to Ni(111).

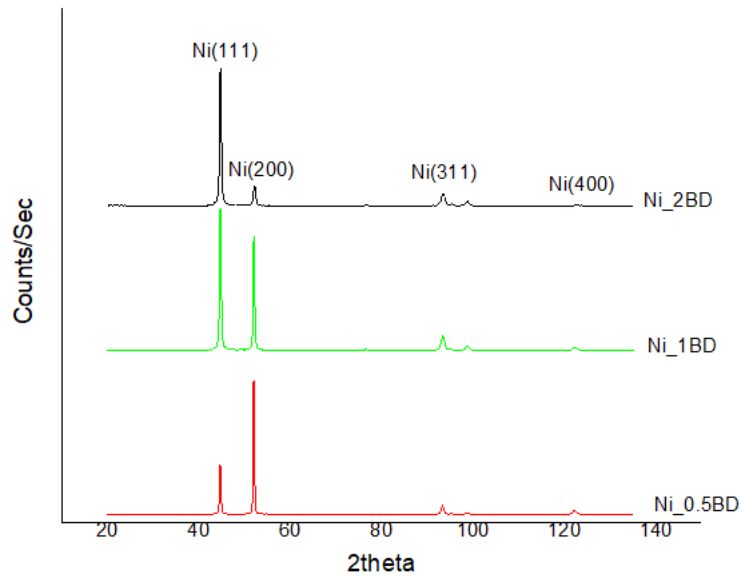


Figure 59: XRD patterns for three different concentration of 2-butyne-1,4-diol.

It is evident that the presence of the brightener has impacted the crystal growth of the Ni-Matrix. Generally, Ni(111) orientation tends to result in coatings with improved microhardness and mechanical properties [93], [94]. So, 2-butyne-1,4-diol not only contributes to the development of bright coatings but also imparts enhanced mechanical properties to the coatings.

Continuing with the experimental process, a subsequent Ni-Watts electrolyte was prepared, with a total volume of 700 mL. Notably, this iteration incorporated nano-ZrO₂ particles. Nano-ZrO₂ particles serve as reinforcing agents in the experimental setup, enhancing the structural and mechanical properties of the materials. The X-ray Diffraction (XRD) patterns corresponding to varying concentrations of nano-ZrO₂ are presented below.

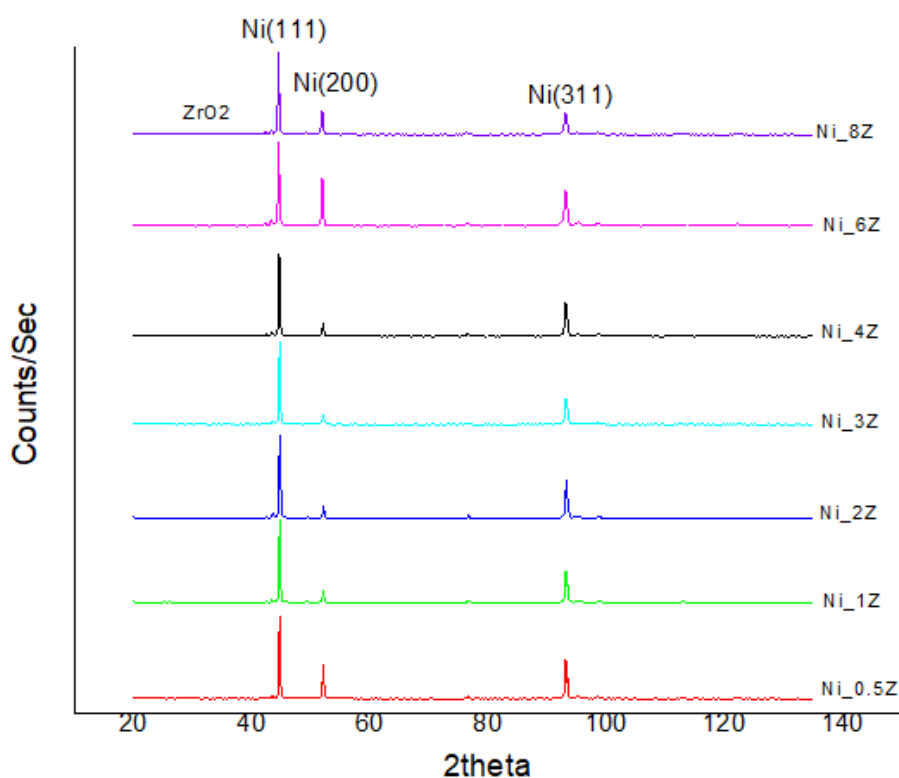


Figure 60: XRD pattern for all the different amounts of nano-ZrO₂.

Figure 60 illustrates the XRD patterns of the nanocomposite coatings, with no discernible ZrO₂ peak observed. This absence can be attributed to the notably high intensities of the Ni peaks in comparison to those of Zr.

Compared to pure nickel (**Figure 58**), discernible changes in the preferred orientation and the overall XRD pattern indicate the influence of Zr. The presence of Zr has induced alterations in the structural characteristics of the material, as evidenced by the observed shifts in peak intensities. These variations underscore the impact of Zr on the crystalline structure of the nanocomposite, implying potential modifications in its physical and mechanical properties.

Furthermore, in all tested concentrations of nano-ZrO₂ within the electrolyte, a consistent observation is the preferred orientation being Ni(111). This finding suggests that the addition of nano-ZrO₂ alter the predominant crystallographic orientation of the nickel matrix.

Continuing with the new nanocomposite electrolyte, which maintains a steady concentration of nano-ZrO₂ at 8 g/L, where the point of optimal results is occurred. Introducing three different concentrations of 2-butyne-1,4-diol, we examined the impact of the brightener under both Direct and pulse current conditions, across four distinct duty cycles. This exploration is designed to reveal the nuanced effects of the combined variables on the electrochemical performance of the system. The XRD patterns are as follows,

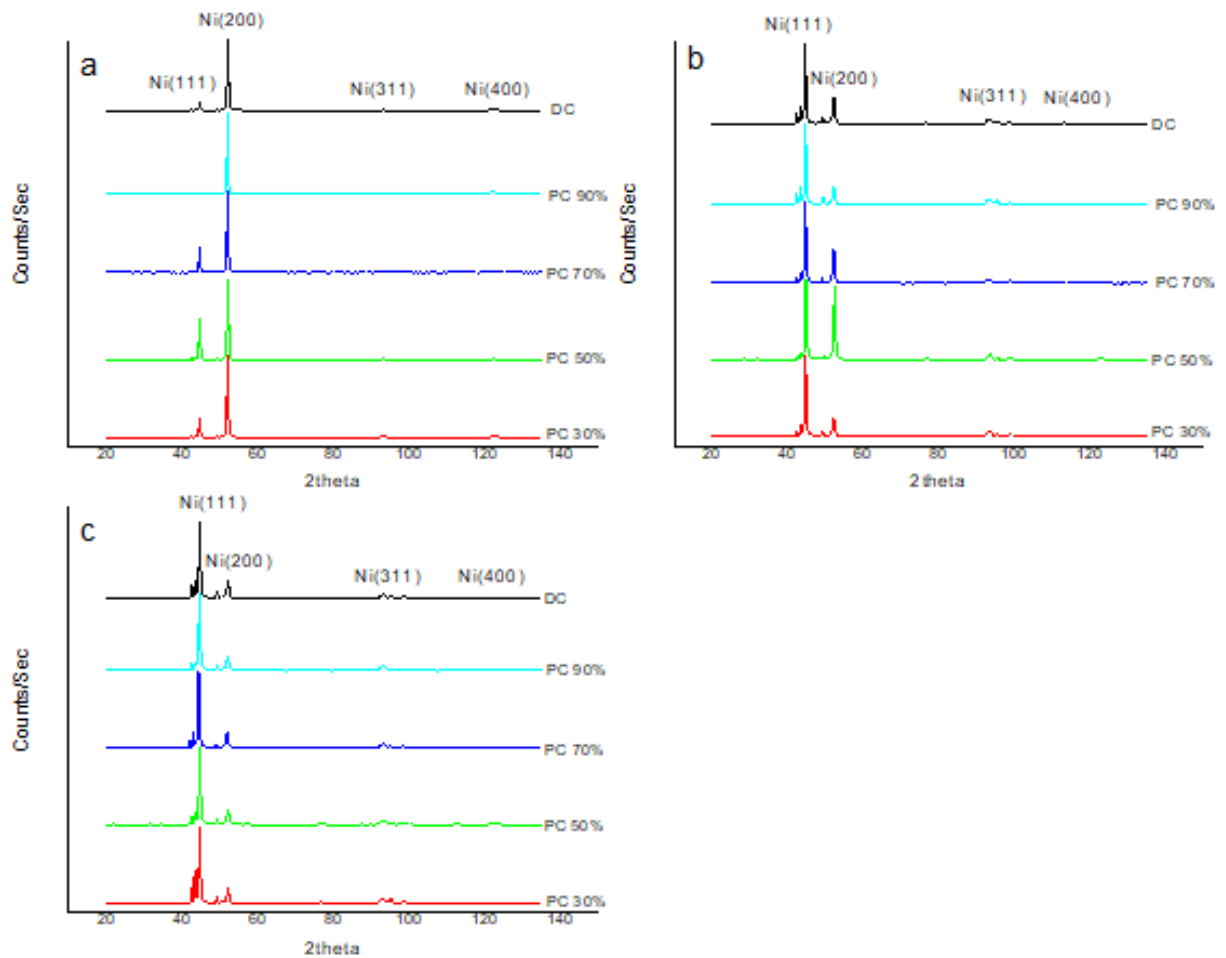


Figure 61: XRD patterns for nanocomposite coatings produced by applying Direct and Pulse current at four different duty cycles, containing 8gr/L nano-ZrO₂ at three different 2-butyne-1,4-diol concentrations: (a) 0.5mmol/L, (b) 1mmol/L, (c) 2mmol/L.

Figure 61 (a) presents the XRD patterns under both direct and pulse current conditions at four distinct duty cycles for nanocomposite coatings with 8 g/L ZrO₂ and 0.5 mmol/L 2-butyne-1,4-diol. Across all duty cycles, the consistent observation is the preferred orientation being Ni(200). Notably, as the duty cycle decreases, there is a notable increase in the intensity of Ni(111). However, it remains at a lower intensity compared to Ni(200). This trend suggests an influence of duty cycles on the crystalline orientation, with a particular impact on the intensity of specific crystallographic planes.

Subsequently, with an increased concentration of the brightener at 1 mmol/L (Figure 61 (b)), the impact becomes more evident. The preferred orientation undergoes a notable shift from Ni(200) to Ni(111). Across all duty cycles, Ni(111) emerges as the dominant orientation. Interestingly, at a duty cycle of 50%, there is an observed increase in the Ni(200) orientation. However, it still maintains a lower intensity compared to Ni(111). This shift underscores the influence of the brightener concentration on the crystalline orientation. According to research findings, composite coatings featuring a predominantly oriented crystal plane of (200) typically exhibit reduced hardness and increased ductility compared to those with a (111) orientation, as demonstrated in the literature [95].

Finally, the XRD patterns with a brightener concentration of 2 mmol/L (Figure 61 (c)), are presented. Ni(111) emerges as the exclusive preferred orientation across all conditions. This observation suggests a dominant and stabilizing effect of the higher brightener concentration.

8.3 SEM and EDS analysis of composite and nanocomposite coatings

The morphology of the samples and the elemental mapping, aimed at determining the Zirconium (Zr) content incorporated in the coatings, were investigated using Scanning Electron Microscopy (SEM) and Energy-Dispersive X-ray Spectroscopy (EDS).

The scanning electron microscopy (SEM) was conducted using a JEOL instrument, model IT500LV, while energy-dispersive X-ray spectroscopy (EDS) analysis was performed using an Oxford Instruments instrument, model X-Max Extreme.

SEM was employed to examine the surface topography and morphology of the samples at a micro/nano scale level and EDS, on the other hand, facilitated the elemental analysis by detecting and quantifying the elemental composition present in the samples.

First, SEM images are presented for three distinct concentrations of nano-ZrO₂: 4 g/L, 6 g/L and 8 g/L. These nanocomposite coatings produced under direct current, without the addition of 2-butyne-1,4-diol. These images provide a detailed view of the morphology and structure of the coatings at the nanoscale for each concentration.

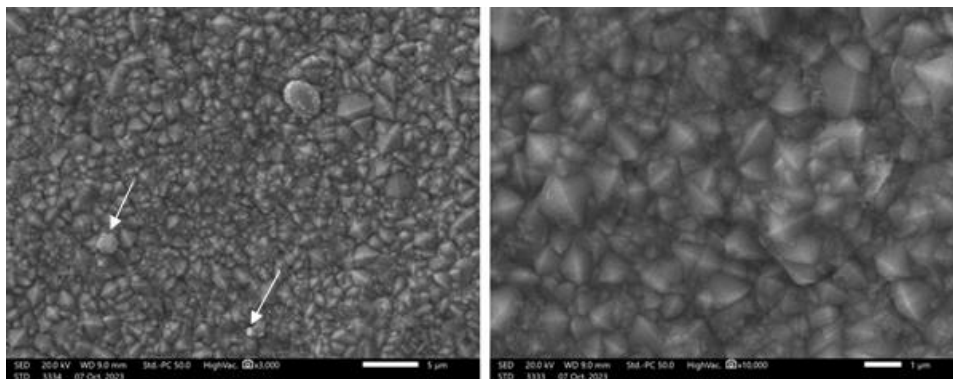


Figure 62: SEM images for Ni_4Z sample at two different magnifications (The scale left is 5 μm and right 1 μm).

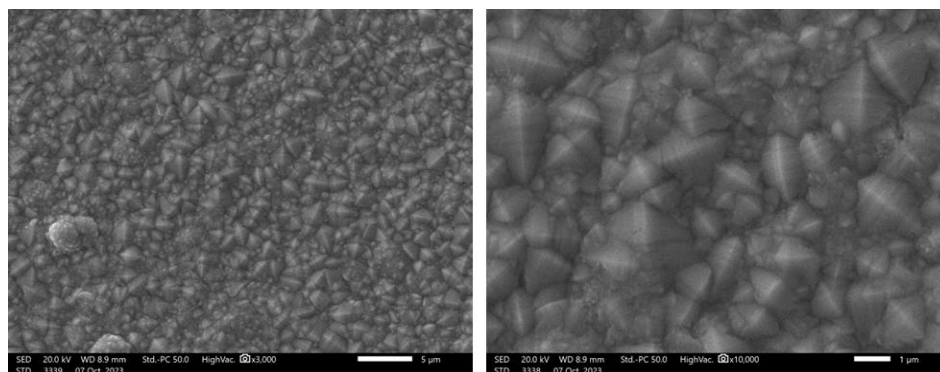


Figure 63: SEM images for Ni_6Z sample at two different magnifications (The scale left is 5 μm and right 1 μm).

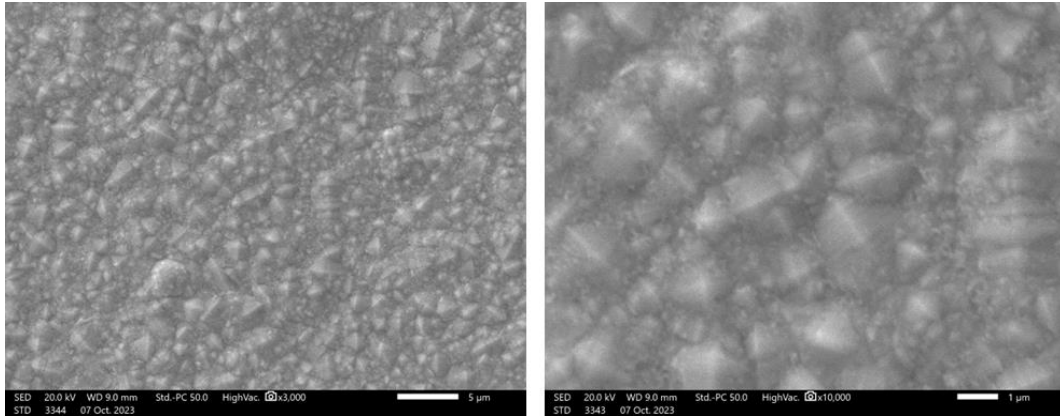


Figure 64: SEM images for Ni_8Z sample at two different magnifications (The scale left is 5μm and right 1μm).

The analysis reveals that the nanocomposite nickel deposits exhibit exceptional texture perfection, characterized by very well-formed, micron-sized [100] crystallites. The highly ordered arrangement of [100] crystallites in the microstructure signifies a specific crystallographic orientation, suggesting a uniform and organized growth pattern. The nickel nanocomposite coatings exhibit distinctive pyramidal and polyhedral crystal structures, contributing to a visually intriguing and complex morphology. The SEM images reveal a surface characterized by irregularities, resulting in an uneven topography. These features suggest a heterogeneous distribution of nickel and nano-ZrO₂ constituents [72], [91], [96].

The specimens containing 4, 6, and 8 g/L nano-ZrO₂ were subjected to analysis using scanning electron microscopy (SEM) and energy-dispersive X-ray spectroscopy (EDS). Through elemental mapping, the weight percentage of Zr was determined.

Sample	Zr(wt%)
Ni_4Z	1.6
Ni_6Z	3.1
Ni_8Z	3

Table 6: Estimation of the weight percentage content of zirconia in the nanocomposite coatings.

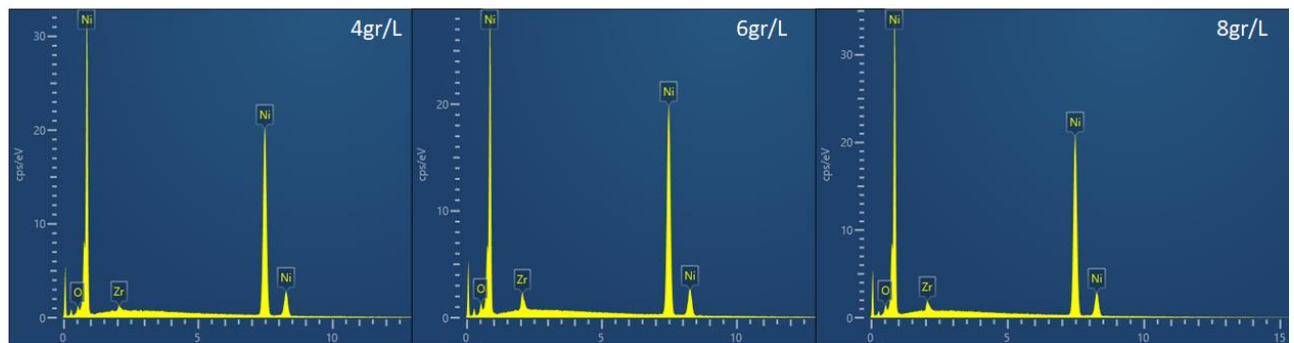


Figure 65: EDS spectra for the nanocomposite coatings, under DC without the brightener.

Focusing on the coating with 8g/L nanoZrO₂, it was possible to detect a nanocrystal of ZrO₂.

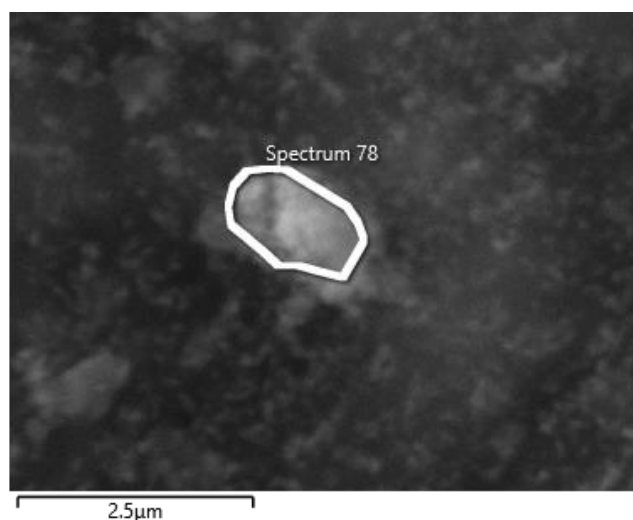


Figure 66: Nanocrystal of ZrO₂, detected in the sample Ni_8Z.

Through elemental mapping, the weight percentage of Zirconium (Zr) is determined to be 25%. Presents the EDS spectrum of the above area (Figure 66), where nano-ZrO₂ has been incorporated in the coating.

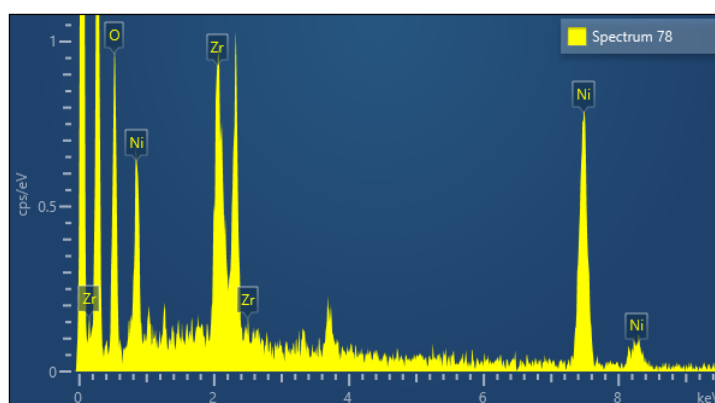


Figure 67: EDS spectrum indicating the incorporation of nano-ZrO₂ in the coating.

Following that, nanocomposite coatings containing 8g/L nano-ZrO₂ and three distinct concentrations of the brightener were also analyzed using SEM and EDS techniques. These coatings were synthesized employing both DS and PC currents.

For nanocomposite coatings with 0.5mmol/L 2-butyne-1,4-diol, the SEM and EDS analysis results are as follows,

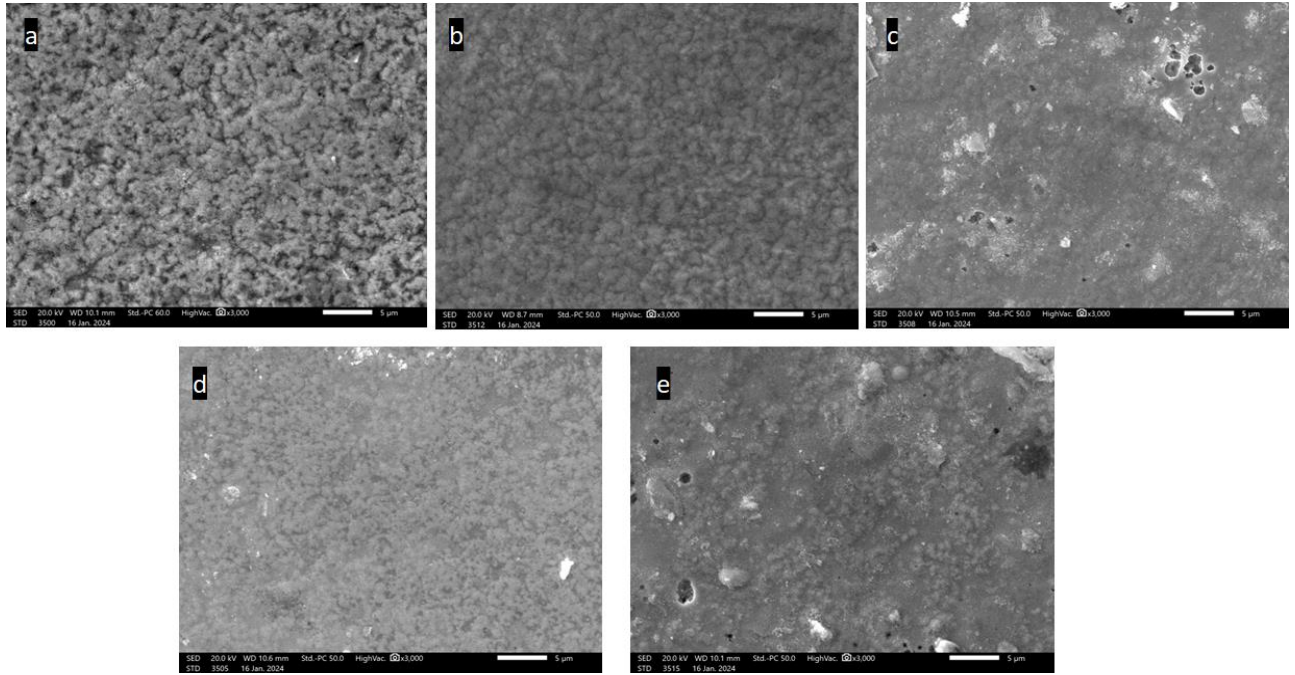


Figure 68: SEM images for the samples: a) Ni1_0.5B_8Z (DC), b)Ni2_0.5BD_8Z(PC d.c.=90%), c)Ni3_0.5BD_8Z(PC d.c.=70%), d)Ni4_0.5BD_8Z(PC d.c.=50%), e)Ni5_0.5BD_8Z(PC d.c.=30%), at a scale of 5µm.

Figure 68 depicts the morphological characteristics of samples featuring 0.5 mmol/L 2-butyne-1,4-diol and 8 g/L nano-ZrO₂, subjected to varying current conditions (DC, PC) and duty cycles. Notably, under pulse current application, the surface becomes more compact. This enhanced compact correlates with improved mechanical properties, particularly microhardness, and makes the structure more resistant to deformations, which can be spread within the surface. Generally, pulse current conditions consistently yield coatings characterized by greater uniformity and compactness. Furthermore, compared to Figure 64, it is obvious that the presence of the brightener has affected the structure by making it more uniform.

Additionally, it is evident that the duty cycle of 90% has a negligible impact on the structure compared to direct current. This outcome is expected, because as the duty cycle increases, the exerted pulse by the pulse current condition has large t_{on} , so the electrodeposition conditions would approximate those of constant current electrolysis (DC), potentially resulting in the formation of large grains and the occurrence of side reactions.

At duty cycles of 30% and 70% in pulse current, it's evident that the surface has attained a notably compact structure. Despite the generally compact and uniform surface observed, the presence of pitting marks is noted. These marks, indicative of localized corrosion or surface imperfections or the adsorption of hydrogen atoms and the non-sufficient electrodeposition of the metal ions, suggesting potential areas of vulnerability within the coating structure.

Through elemental mapping, the weight percentage of Zr was determined.

Sample	Zr(wt%) (scale:25μm)
Ni1_0.5BD_8Z	0.2
Ni2_0.5BD_8Z	0.2
Ni3_0.5BD_8Z	2.3
Ni4_0.5BD_8Z	1.7
Ni5_0.5BD_8Z	4.2

Table 7: Estimation of the weight percentage content of zirconia in the nanocomposite coatings, with different current conditions.

The samples subjected to a 30% and 70% duty cycle demonstrated the highest weight percentage of Zr. At a larger scale of 10μm, the presence of nanocrystals of ZrO₂ incorporated within the coating Ni5_0.5BD_8Z becomes more evident, as presented in Figure 69 . Moreover, when a measurement with EDS conducted on a single point, the zirconium content reached as high as 70% .

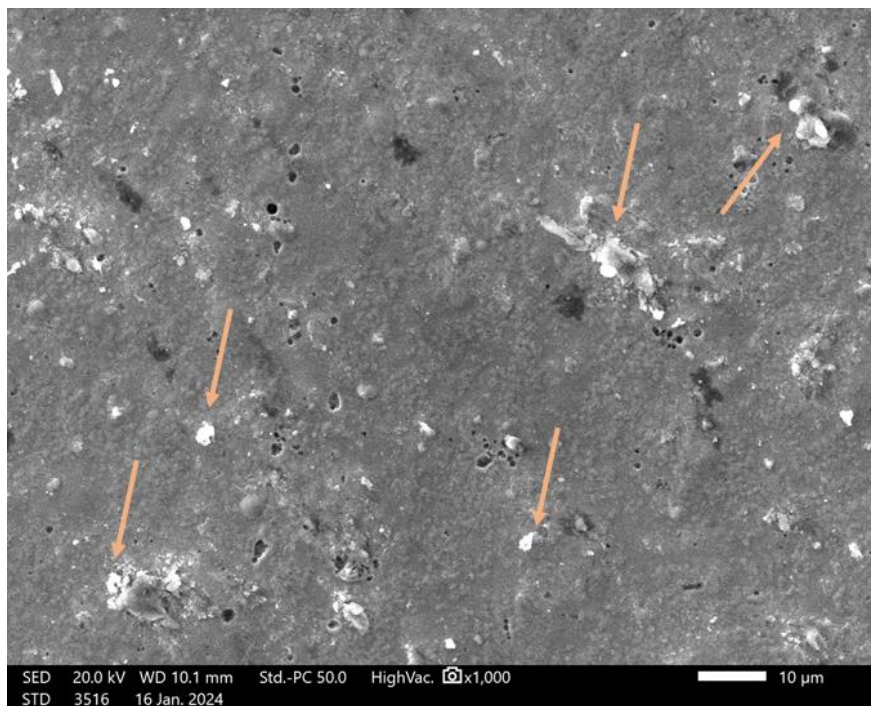


Figure 69: SEM image of the Ni5_0.5BD_8Z (PC d.c.=30%), at a scale of 10μm.

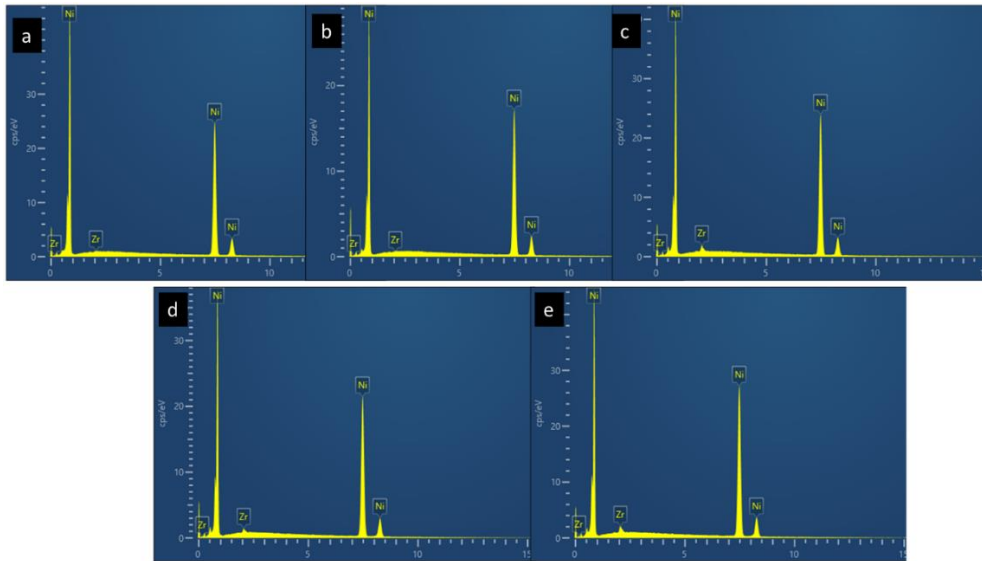


Figure 70: EDS spectra for the nanocomposite coatings: a) Ni1_0.5B_8Z (DC), b) Ni2_0.5BD_8Z(PC d.c.=90%), c) Ni3_0.5BD_8Z(PC d.c.=70%), d) Ni4_0.5BD_8Z(PC d.c.=50%), e) Ni5_0.5BD_8Z(PC d.c.=30%).

For nanocomposite coatings with 1mmol/L 2-butyne-1,4-diol, the SEM and EDS analysis results are as follows,

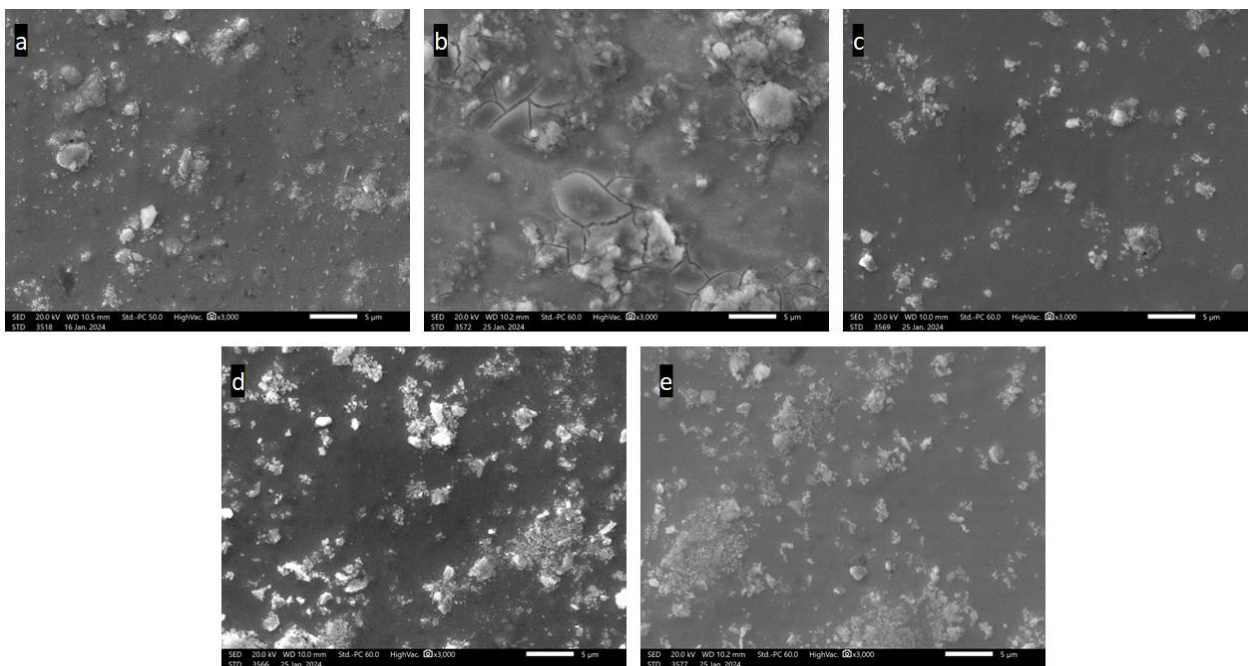


Figure 71: SEM images for the samples: a) Ni1_1B_8Z (DC), b) Ni2_1BD_8Z(PC d.c.=90%), c) Ni3_1BD_8Z(PC d.c.=70%), d) Ni4_1BD_8Z(PC d.c.=50%), e) Ni5_1BD_8Z(PC d.c.=30%), at a scale of 5 μ m.

In contrast to Figure 64, it is evident that a higher concentration of the brightener results in a more compact surface. Across all current conditions, the surface demonstrates uniformity, although some cracks are detected for the sample Ni2_1BD_8Z (d.c.=90%). This phenomenon may stem from various factors, including uneven deposition, inadequate cleaning and substrate preparation prior to electroplating, and potential hydrogen embrittlement [97].

For samples subjected to duty cycles of 70%, 50%, and 30%, a highly compact surface is observable, accompanied by the presence of ZrO₂ nanocrystals.

Through elemental mapping, the weight percentage of Zr was determined.

Sample	Zr(wt%) (scale 25µm)
Ni1_1BD_8Z	3
Ni2_1BD_8Z	3.2
Ni3_1BD_8Z	3.7
Ni4_1BD_8Z	4.7
Ni5_1BD_8Z	6.1

Table 8: Estimation of the weight percentage content of zirconia in the nanocomposite coatings, with different current conditions.

In this case, coatings generated through direct current and pulse current application, with a duty cycle of 30%, demonstrated the highest percentage of zirconia.

At a larger scale of 10µm, the presence of nanocrystals of ZrO₂ incorporated within the coating Ni4_1BD_8Z becomes more evident, as presented in Figure 72.

It should be noted that, when a measurement with EDS conducted on a single point, the zirconium content of Ni4_1BD_8Z reached as high as 17.4%.

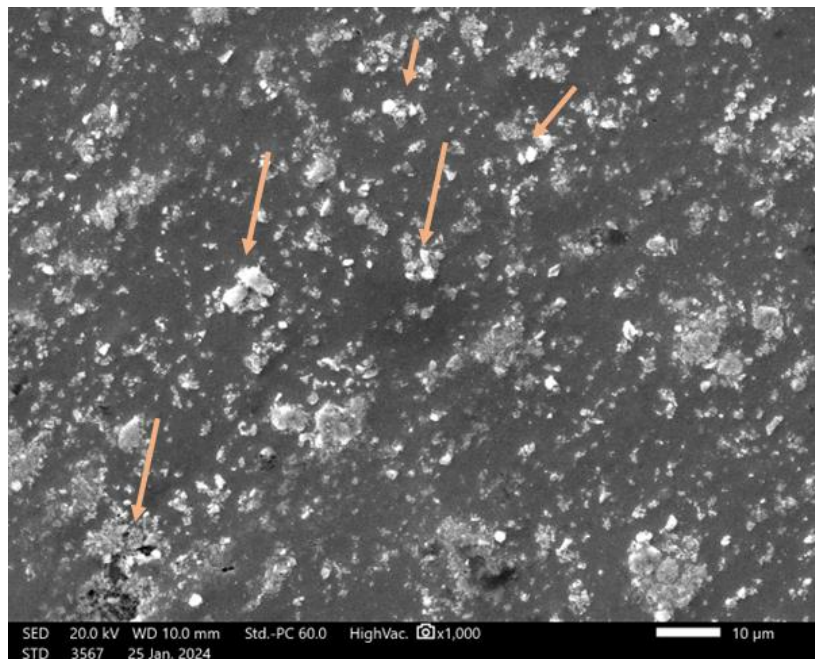


Figure 72: SEM image of the Ni4_1BD_8Z (PC d.c.=50%), at a scale of 10µm.

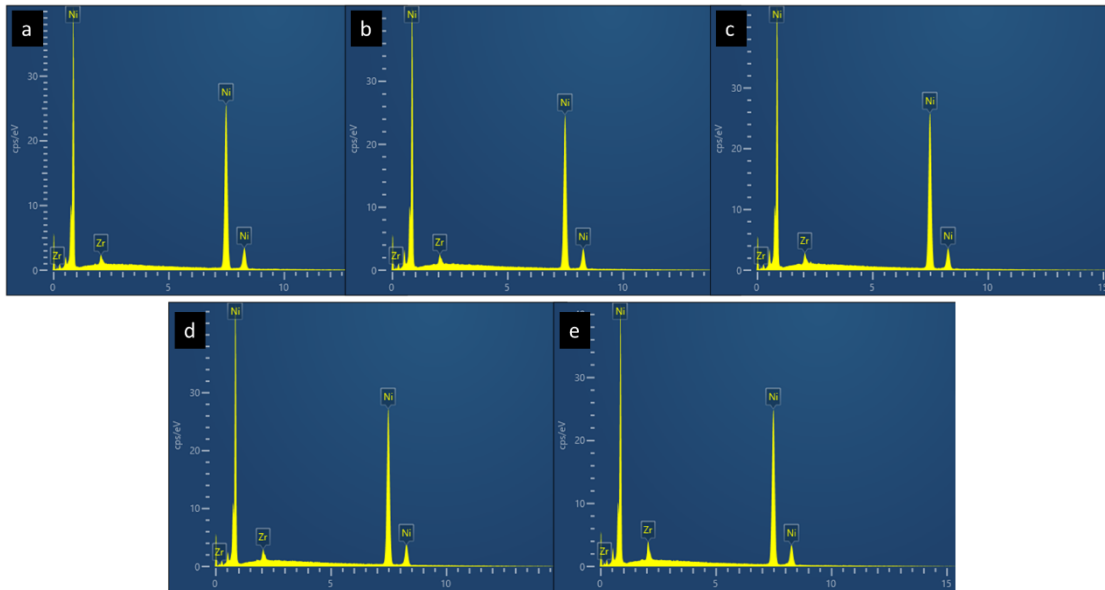


Figure 73: EDS spectra for the nanocomposite coatings: a) Ni1_1B_8Z (DC), b)Ni2_1BD_8Z(PC d.c.=90%), c)Ni3_1BD_8Z(PC d.c.=70%), d)Ni4_1BD_8Z(PC d.c.=50%), e)Ni5_1BD_8Z(PC d.c.=30%).

Finally, for nanocomposite coatings with 2mmol/L 2-butyne-1,4-diol, the SEM and EDS analysis results are as follows,

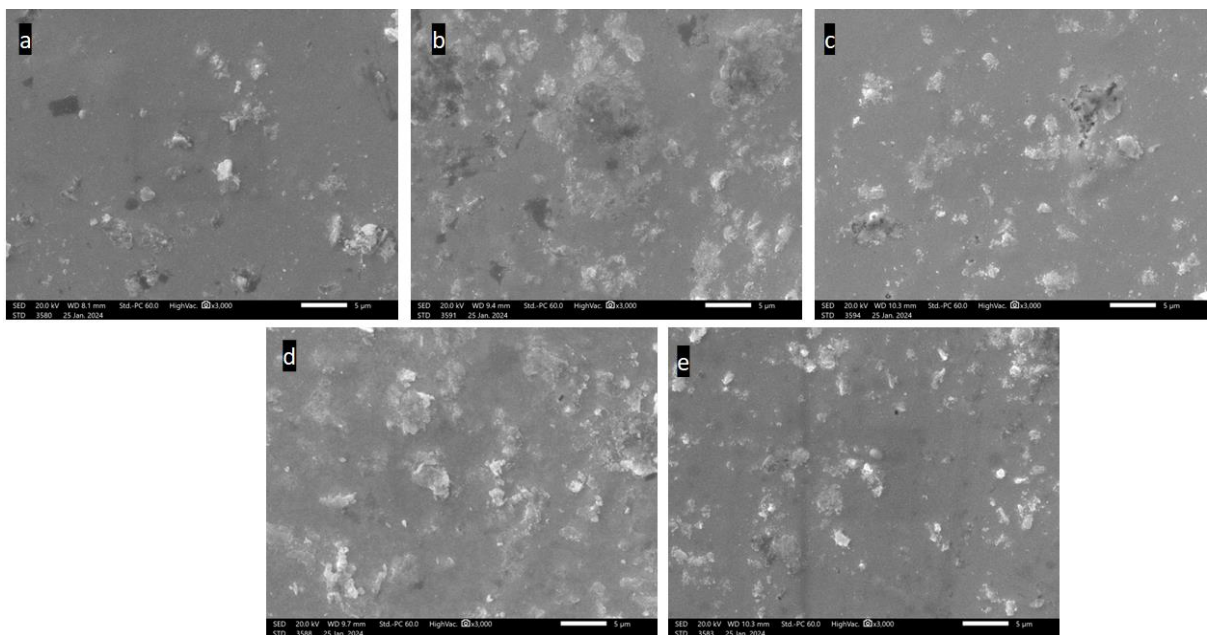


Figure 74: SEM images for the samples: a) Ni1_2B_8Z (DC), b)Ni2_2BD_8Z(PC d.c.=90%), c)Ni3_2BD_8Z(PC d.c.=70%), d)Ni4_2BD_8Z(PC d.c.=50%), e)Ni5_2BD_8Z(PC d.c.=30%), at a scale of 5 μ m.

The inclusion of 2-butyne-1,4-diol is evidently correlated with a notable enhancement in the morphology and structural integrity of the coatings. The granularity of the grains is markedly finer in comparison to samples devoid of or containing lower concentrations of the brightener. Moreover, across all current conditions, the surface is characterized by the presence of fine grains.

Sample	Zr(wt%) (scale:25μm)
Ni1_2BD_8Z	3.2
Ni2_2BD_8Z	4.2
Ni3_2BD_8Z	1.7
Ni4_2BD_8Z	4.7
Ni5_2BD_8Z	3.2

Table 9: : Estimation of the weight percentage content of zirconia in the nanocomposite coatings, with different current conditions.

Here, coatings generated through direct current and pulse current application, with a duty cycle of 50%, demonstrated the highest percentage of zirconia.

Coating with duty cycle of 70% exhibited low weight percentages of zirconia content.

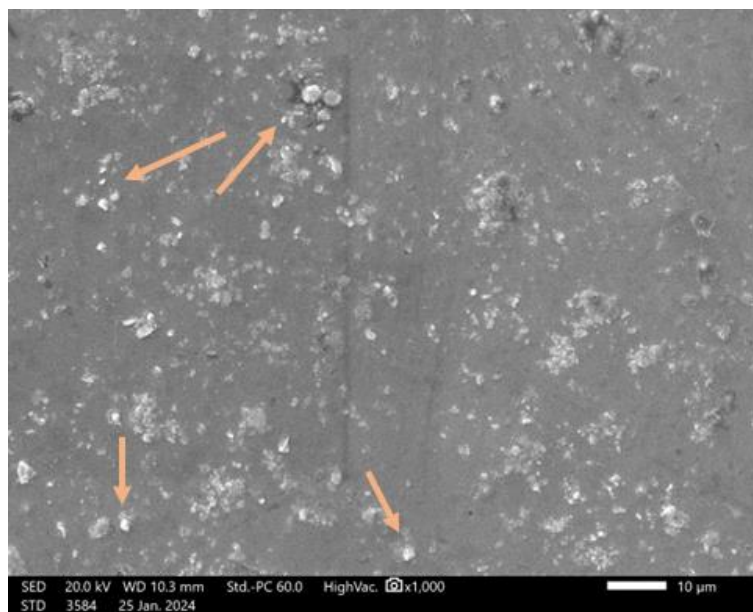


Figure 75:SEM image of the Ni4_2BD_8Z (PC d.c.=50%), at a scale of 10μm.

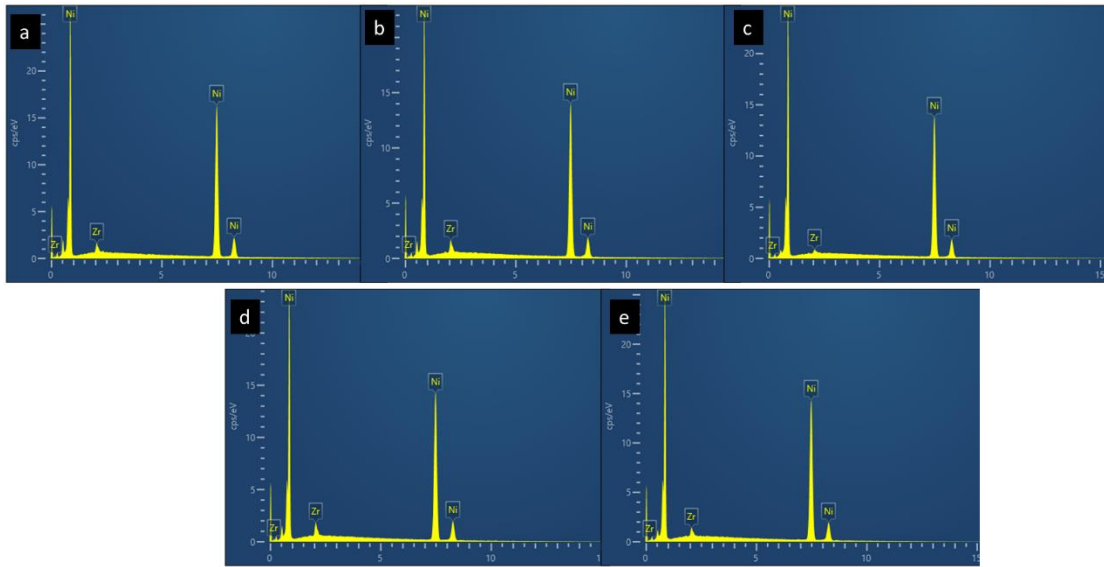


Figure 76: : EDS spectra for the nanocomposite coatings: a) Ni1_2B_8Z (DC), b) Ni2_2BD_8Z(PC d.c.=90%), c) Ni3_2BD_8Z(PC d.c.=70%), d) Ni4_2BD_8Z(PC d.c.=50%), e) Ni5_2BD_8Z(PC d.c.=30%).

8.4 Vickers Microhardness

The Vickers method was utilized to assess the microhardness of the entire range of generated coatings, employing the assistance of the 402 MVD Microhardness Tester manufactured by Wolpert Wilson Instruments. This specific apparatus is capable of applying loads ranging from 10 g to 2 kg. For the measurements, a load of 50–250 g, an application time of 15 s, and a penetration speed of 0.3 mm/s were chosen.

Firstly, the microhardness results for pure nickel, serving as a baseline, are presented. Subsequently, the microhardness values for samples containing additions of 0.5, 1, and 2 mmol/L of 2-butyne-1,4-diol are provided.

In the microhardness assessments, values ranging from 170HV to 320HV were recorded, with the highest observed value reaching 321.92HV. Notably, this peak hardness was achieved upon the addition of 1mmol/L of the brightener.

The introduction of the brightener evidently enhances the microhardness of the coating, more than doubling the microhardness compared to the baseline.

The results are presented in Table 10,

Sample	Vickers Microhardness (HV)
Ni1	177.42±11.69
Ni_0.5BD	297.54±24.77
Ni_1BD	321.92±19.11
Ni_2BD	315.19±22.69

Table 10: Vickers Microhardness for pure Ni coating and composite coatings with 2-butyne-1,4-diol.

It has been reported that the addition of 2-butyne-1,4-diol refine the grains within the coating. Typically, it is anticipated that as the quantity of BD increases, there will be a

consistent reduction in grain size, consequently leading to elevated hardness values in the deposits. This correlation between grain refinement and hardness enhancement suggests that higher concentrations of BD yield coatings with superior mechanical properties [57]. Also, from **Figure 59**, as the concentration of the brightener increases, the intensity of Ni (111) orientation is increasing, which tends to result in coatings with improved microhardness and mechanical properties.

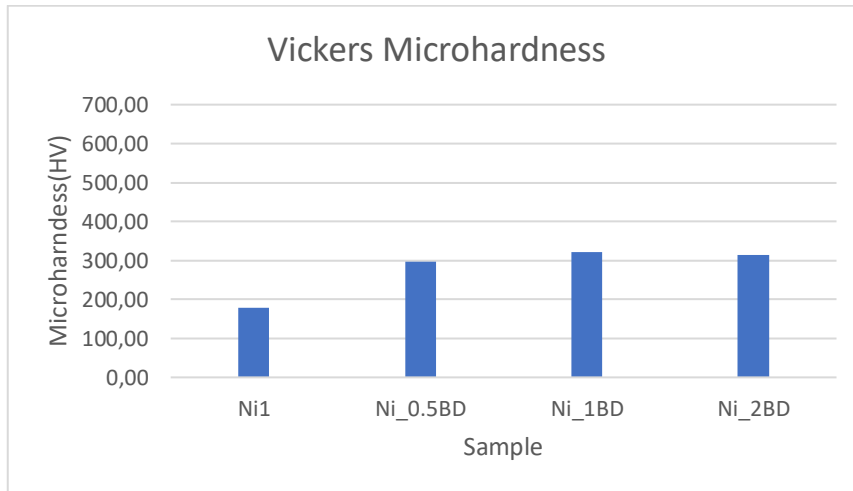


Figure 77: Vickers Microhardness values for pure Nickel coatings and coatings with three different concentrations of 2-butyne-1,4-diol.

Continuing, nanocomposite coatings were produced using nano-ZrO₂ as a reinforcing agent, by applying DC current.

The microhardness values ranged from 230HV to 300HV, with the highest recorded value being 300.7HV observed upon the addition of 8GR/L nano-ZrO₂.

The results are presented in Table 11,

Sample	Vickers Microhardness(HV)
Ni_0.5Z	218±19.34
Ni_1Z	239.21±21.67
Ni_2Z	250.32±25.28
Ni_3Z	231.02±19.16
Ni_4Z	259.48±30.68
Ni_6Z	271.35±28.23
Ni_8Z	300.70±24.75

Table 11: Vickers Microhardness for Ni-Matrix nanocomposite coatings.

The incorporation of nano-ZrO₂ into the nanocomposite coatings yielded notable improvements in microhardness. This enhancement was particularly evident when comparing these coated materials with conventional pure nickel coatings. By subjecting the coatings to comparative analysis, it becomes clear that the presence of nano-ZrO₂ resulted in a substantial increase in microhardness values. This enhancement in microhardness underscores the effective integration of the nano-ZrO₂ particles within the matrix of the coating material. As a result, the nanocomposite

coatings exhibited superior mechanical properties compared to their pure nickel sample.

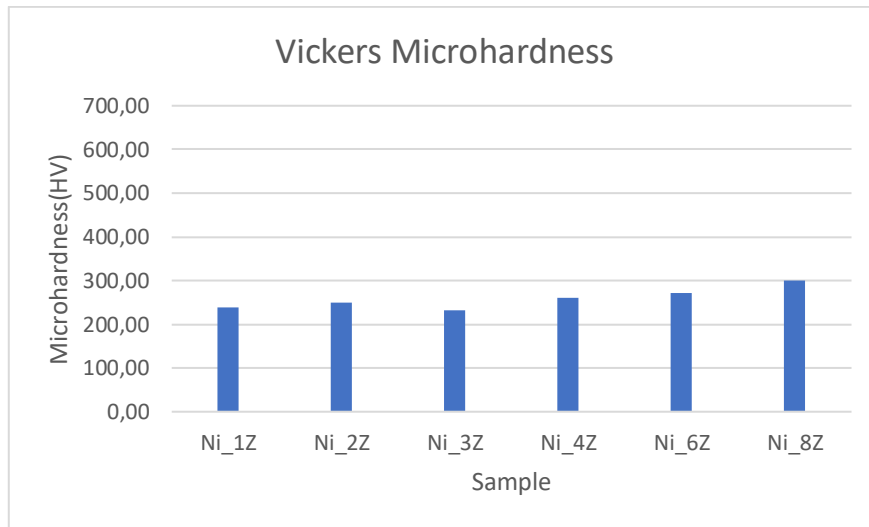


Figure 78: Vickers Microhardness values for Nickel-Matrix nanocomposite coatings using nano-ZrO₂ as reinforcing means.

Furthermore, it's evident that higher concentrations of nano-ZrO₂ result in increased microhardness values. This correlation suggests that the quantity of nano-ZrO₂ incorporated into the coating directly influences its microhardness. As the concentration of nano-ZrO₂ rises, there is a corresponding enhancement in microhardness, indicating the strengthening effect imparted by the nanoparticles. Based on Table 6, the sample Ni_8Z exhibits the highest weight percentage of zirconia and that led to higher microhardness.

Continuing the analysis of our experimental findings, now the Vickers microhardness assessment of Ni-Matrix nanocomposite coatings, infused with 8gr/L nano-ZrO₂ and subjected to three distinct concentrations of 2-butyne-1,4-diol, is presented. These evaluations were conducted under both Direct Current (DC) and Pulse Current (PC) conditions across four varying duty cycles (30%, 50%, 70%, 90%). The results of these examinations are detailed below.

It is evident that as the concentration of the brightener increases, so does the microhardness. Both the concentration of the brightener and the current condition exert influence on microhardness values.

The results are presented in Table 12,

Sample	Vickers Microhardness (HV)
Ni1_0.5BD_8Z	295.43±23.26
Ni2_0.5BD_8Z	239.48±23.19
Ni3_0.5BD_8Z	332.39±40.25
Ni4_0.5BD_8Z	316.71±25.23
Ni5_0.5BD_8Z	369.78±28.39
Ni1_1BD_8Z	507.45±71.45
Ni2_1BD_8Z	470.84±41.63

Ni3_1BD_8Z	539.36±38.62
Ni4_1BD_8Z	536.18±25.81
Ni5_1BD_8Z	487.57±42.70
Ni1_2BD_8Z	570.09±32.73
Ni2_2BD_8Z	612.39±37.73
Ni3_2BD_8Z	587.92±36.87
Ni4_2BD_8Z	530.29±46.71
Ni5_2BD_8Z	621.43±38.28

Table 12: Vickers Microhardness for Ni-Matrix nanocomposite coatings, under DC and PC conditions.

For samples with 0.5mmol/L of the brightener, the highest microhardness achieved at pulse current with 30% duty cycle. This result aligns with the percentage of zirconia , presented in Table 7, where the highest weight percentage of zirconia occurs with 30% and 70% duty cycle.

For samples with 1mmol/L of the brightener, the highest percentage of zirconia detected at pulse current with 70% duty cycle. This result, doesn't align with the content of zirconia in these coatings, presented in Table 8.

Finally, for samples with 2mmol/L of the brightener, the highest microhardness appeared at pulse current with 30% duty cycle, which doesn't aligns with the content of zirconia incorporated in the coatings, presented in Table 9, but it's clear that the sample with 90% duty cycle exhibit high value of microhardness and content of zirconia.

The peak microhardness of 621.43HV was attained at 2 mmol/L of 2-butyne-1,2-diole with a pulse current of 30% duty cycle. Overall, pulse current operations yielded higher microhardness values compared to DC.

A 30% duty cycle appears beneficial for samples with brightener concentrations of 0.5 and 2 mmol/L. Generally, a lower duty cycle corresponds to a longer t_{off} period, defined as the duration during which no current flows through the electrolyte. This extended t_{off} period allows more opportunities for nanoparticles to migrate to the double layer. Consequently, a greater amount of zirconia was incorporated into the coatings at low duty cycles, resulting in increased hardness [98].

For the sample with a 1mmol/L concentration of the brightener, a 70% duty cycle seems to be beneficial.

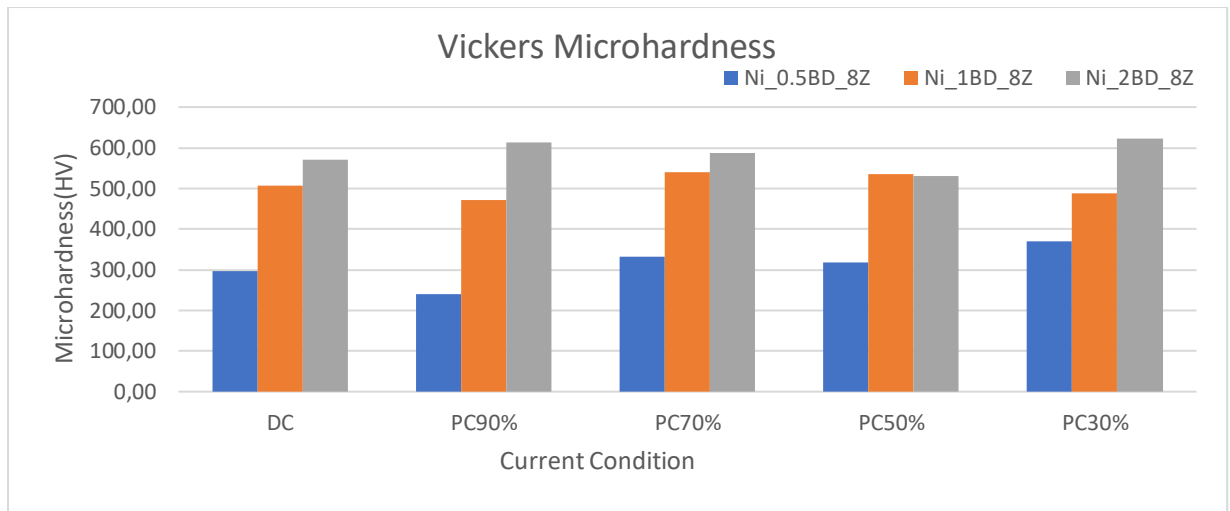


Figure 79: Vickers Microhardness values for Ni-Matrix nanocomposite coatings, under DC and PC condition.

8.5 Roughness

To determine the Ra values across all coatings, a portable digital profilometer was used, Hommel Tester T1000, manufactured by Hommel Werke. This device, utilized for roughness determination, not only directly recorded the surface profiles of the specimens but also automatically computed Rz, Rt, and Ra. Additionally, it featured a built-in printer capable of producing a comprehensive printout of the test results. A total traverse length of 4.8mm was selected, and a minimum of five roughness measurements were taken from various points on each specimen's surface. The roughness value of each specimen represents the average R_a values where the corresponding R_z and R_t do not exhibit significant deviation.

First, the change in the roughness of the coatings, with the increase in the concentration of the brightener, is presented.

The findings are displayed within

Table 13

Sample	Roughness(μm)
Ni1	0.22 ± 0.08
Ni_0.5BD	0.04 ± 0.01
Ni_1BD	0.08 ± 0.05
Ni_2BD	0.17 ± 0.07

Table 13: Roughness values for pure Nickel coatings with three different concentrations of the brightener.

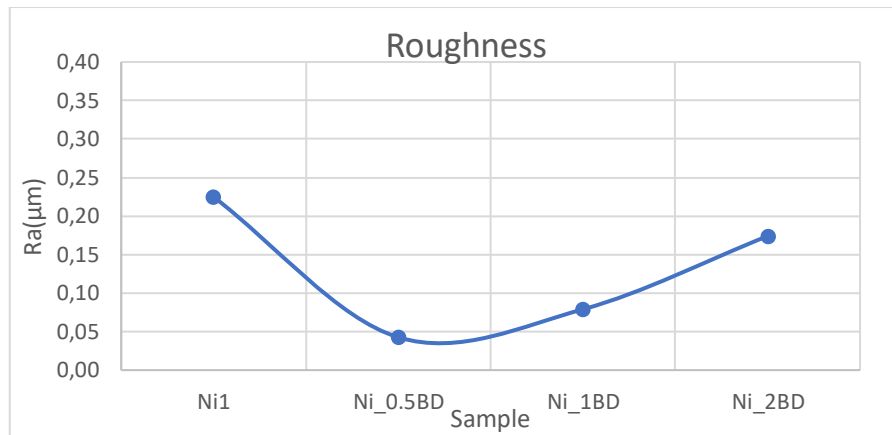


Figure 80: Roughness for pure Nickel coating and coatings with 2-butyne-1,4-diol.

Based on **Figure 80**, surface roughness, varying between 0.22µm and 0.04µm, exhibits the highest value in the pure nickel coating and the lowest when 0.5mmol/L of the brightener was being introduced in the electrolyte. It is evident that the presence of 2-butyne-1,4-diol has influenced the surface characteristics by diminishing the roughness, consequently yielding a smoother surface texture.

Typically, the primary function of brighteners is to enhance the leveling capacity of the bath, facilitating preferential deposition on surface defects and scratches. This process contributes to smoother surface texture with reduced roughness as the thickness of the deposit increases [56].

Subsequently, the change in roughness is presented concerning the quantity of nano-ZrO₂.

The findings presented in Table 14,

Sample	Roughness(µm)
Ni_0.5Z	0.17±0.03
Ni_1Z	0.25±0.03
Ni_2Z	0.16±0.03
Ni_3Z	0.17±0.02
Ni_4Z	0.19±0.04
Ni_6Z	0.16±0.01
Ni_8Z	0.20±0.03

Table 14: Roughness values for nanocomposite coatings.

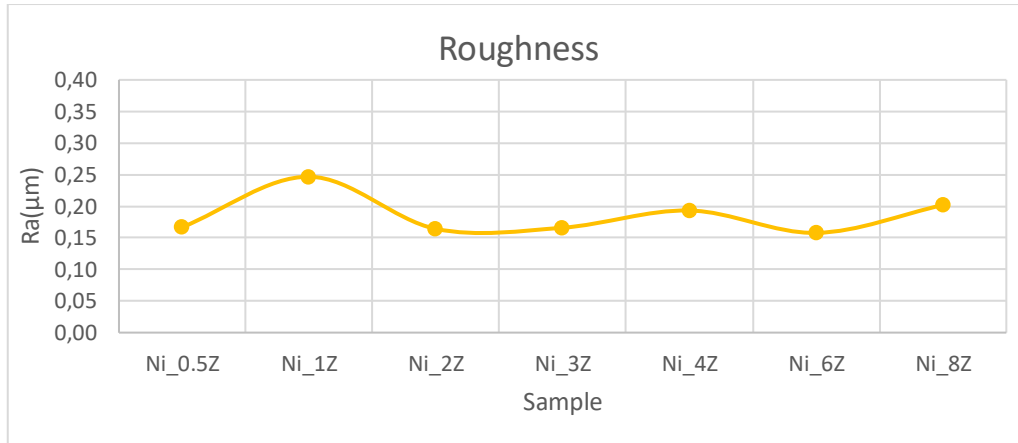


Figure 81: Roughness for Ni-Matrix nanocomposite coatings, using nano-ZrO₂.

It is obvious that the roughness remains almost steady with the concentration of nano-ZrO₂ in the electrolyte. The roughness spans from 0.25μm to 0.16μm, reaching its peak at 0.25μm with the addition of 1gr/L nano-ZrO₂ and declining to its lowest point of 0.16μm with the inclusion of 2 and 6gr/L nano-ZrO₂. Overall, the roughness is reduced compared to that of the pure nickel coating.

These results underscore the potential of nano-ZrO₂ in effectively mitigating surface roughness during the electroplating process. The decreasing in roughness levels with the incorporation of nano-ZrO₂ in the electrolyte suggests that it's possible to achieve smoother and more uniform surface.

Lastly, the influence of pulsed current, duty cycle, and brightener concentration on the roughness of the coatings is presented.

The results are displayed as follows,

Sample	Roughness(μm)
Ni1_0.5BD_8Z	0.15±0.03
Ni2_0.5BD_8Z	0.08±0.02
Ni3_0.5BD_8Z	0.17±0.04
Ni4_0.5BD_8Z	0.15±0.02
Ni5_0.5BD_8Z	0.25±0.05
Ni1_1BD_8Z	0.26±0.05
Ni2_1BD_8Z	0.21±0.05
Ni3_1BD_8Z	0.24±0.07
Ni4_1BD_8Z	0.20±0.02
Ni5_1BD_8Z	0.27±0.02
Ni1_2BD_8Z	0.19±0.03
Ni2_2BD_8Z	0.17±0.03
Ni3_2BD_8Z	0.21±0.05
Ni4_2BD_8Z	0.23±0.03
Ni5_2BD_8Z	0.23±0.02

Table 15: Roughness values for nanocomposite coatings, under direct and pulse current.

In evaluating the impact of pulse current, it is evident that both pulse current (PC) and direct current (DC) contribute to the production of coatings with reduced roughness.

Notably, a duty cycle of 90% yields particularly promising outcomes, characterized by surfaces that are notably smooth and uniform. Conversely, a duty cycle of 30% consistently results in the highest roughness across all concentrations of the brightener.

Regarding the concentration of 2-butyne-1,4-diol, the results reveal that a concentration of 1mmol/L of the brightener correlates with higher roughness levels, whereas the lowest concentration of the brightener corresponds to the least rough surfaces. Notably, nanocomposite coatings containing 2mmol/L of the brightener exhibit stability across all duty cycles.

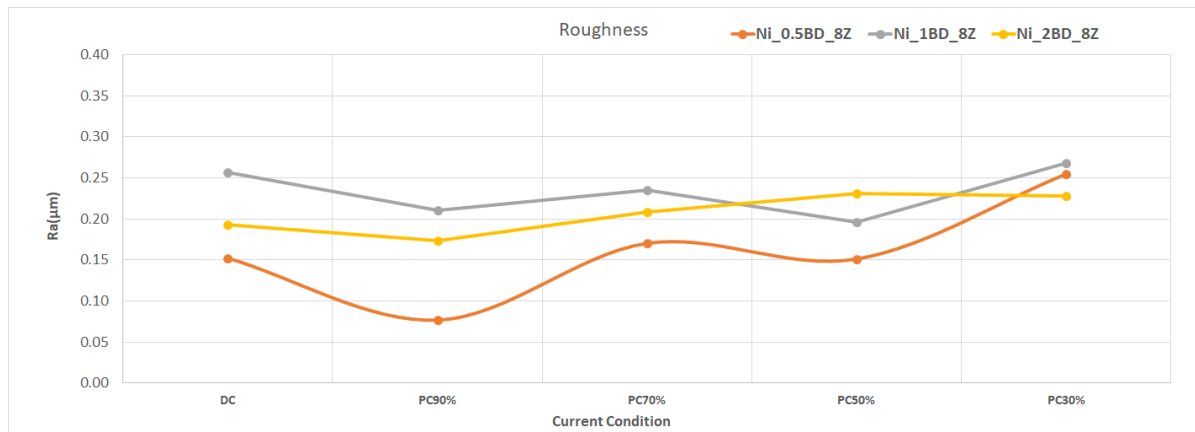


Figure 82: Roughness for Ni-Matrix nanocomposite coatings, under DC and PC. Red line represents then roughness for coatings with 0.5mmol/L brightener, yellow 1mmol/L brightener and grey 2mmol/L brightener.

In general, high-resolution Ni nanostructures are recognized for their low stress levels, high uniformity, and minimal roughness. Studies have indicated that as pulse times decrease (resulting in lower duty cycles), uniformity tends to reduce while stress levels increase, leading to increased roughness [99].

CHAPTER IX:
Conclusions and future work

9.1 Conclusions

9.1.1 The effect of the organic additive 2-butyne-1,4-diol

The organic additive utilized in this study was 2-butyne-1,4-diol. This additive was incorporated at three different concentrations of 0.5, 1, 2 mmol/L, to investigate its impact on the mechanical and morphological characteristics of the coatings. Comparative analysis with pure nickel coating revealed improvements in both properties.

Initially, with the addition of 0.5mmol/L of the additive, the preferred orientation Ni(200) remained unchanged. However, microhardness increased, from 177HV to 297HV, and coating roughness decreased, from 0.22 μ m to 0.04 μ m.

Subsequently, with the introduction of 1 and 2 mmol/L of the additive, the preferred orientation shifted from Ni(200) to Ni(111), and microhardness nearly doubled, rising from 177Hv to 321HV and 315HV with 1 and 2 mmol/L, respectively.

Moreover, roughness decreased from 0.22 μ m to 0.08 μ m and 0.17 μ m with 1 and 2 mmol/L brightener, respectively.

Thus, the incorporation of the additive significantly enhanced both the mechanical properties and the morphology of the structure. The observed enhancements include increased microhardness and decreased roughness. Furthermore, the transition of preferred orientation from Ni(200) to Ni(111).

The current efficiency for the sample of pure Nickel and with 0.5, 1, 2 mmol/L of the additive was steady at 100%.

These findings suggest that the incorporation of 2-butyne-1,4-diol holds promise for enhancing the performance and durability of nickel coatings in various applications.

9.1.2 The effect of nano-ZrO₂

The reinforcing agent employed in this investigation was nano-ZrO₂, which was added at seven different concentrations, ranging from 0.5 to 8g/L. Comparative analysis with pure nickel coating revealed significant alterations in the preferred orientation, shifting from Ni(200) to Ni(111) across all nanoparticle concentrations, indicating evident incorporation of nano-ZrO₂ in the coatings.

Vickers microhardness demonstrated a consistent increase at all nanoparticle concentrations, with the highest value observed at 4, 6, 8 g/L of nano-ZrO₂.

Moreover, roughness exhibited a slight decrease from 0.22 μ m to 0.19 μ m, 0.16 μ m, 0.2 μ m at concentrations of 4, 6, 8g/L, respectively.

These coatings were subjected to SEM and EDS analysis, revealing a rough structure with aggregates and pyramid formations across all concentrations. Elemental mapping identified the highest Zr content at 6 and 8 g/L, where the sample with 8g/L of the nanoparticles exhibited superior uniformity of Zr incorporation.

The current efficiency was for every sample almost above 90%, for samples with 2, 4, 6 g/L nano-ZrO₂, the current efficiency was lower compared to the other samples.

In conclusion, the incorporation of nano-ZrO₂ as a reinforcing agent in nickel coating has results in important improvements in their properties. The consistent increase in Vickers microhardness at all nanoparticle concentrations suggests enhanced mechanical strength. The decrease in roughness underscores better surface quality.

9.1.3 Synergetic effect of 2-butyne-1,4-diol and nano-ZrO₂ under Direct Current

Samples containing 8 g/L nano-ZrO₂ and three different concentrations (0.5, 1, 2 mmol/L) of 2-butyne-1,4-diol were prepared under both direct and pulse current conditions.

During direct current application, no shift in the preferred orientation of Ni(200) was observed with the addition of 0.5 mmol/L of the brightener, while the inclusion of 1 and 2 mmol/L shifted the preferred orientation from Ni(200) to Ni(111).

Moreover, the Vickers microhardness exhibited an increase with the addition of the brightener: 295 HV for 0.5 mmol/L, 507 HV for 1 mmol/L, and 570 HV for 2 mmol/L. These results underscore the significant role of the organic additive in enhancing the mechanical properties of the produced coatings.

Under SEM and EDS investigation, the surface morphology revealed that at 0.5 mmol/L of the brightener, the surface appeared rough and non-compact, but uniform. Conversely, at 1 and 2 mmol/L concentrations, the surface became more compact and uniform. This highlights the significant role of the brightener, as it contributes to refining the grain structure and reducing internal stress within the coatings. EDS analysis indicated a higher content of Zr at higher concentrations of the brightener.

Interestingly, the roughness exhibited a very low value with 0.5 mmol/L of the brightener, while it increased with 1 mmol/L.

The current efficiency was higher for samples with 0.5 mmol/L of the organic additive. With the increasing of the brightener, the current efficiency decreased.

In conclusion, the addition of the brightener resulted in increased Vickers microhardness, demonstrating the significant role of the organic additive in improving the mechanical strength of the coatings. Furthermore, at higher concentrations (1 and 2 mmol/L), the surface became more compact and uniform, indicating the ability of the brightener to refine the grain structure and reduce internal stress within the coatings. In addition, higher concentration of the brightener led to higher values of roughness.

9.1.4 The effect of pulse current

The examination of the nanocomposite coatings was conducted using both direct and pulse current methods, employing four distinct duty cycles: 90%, 70%, 50%, and 30%.

a. For 0.5mmol/L of 2-butyne-1,4-diol

For the coatings featuring 0.5 mmol/L of the brightener and 8 g/L nano-ZrO₂, remarkably, lower duty cycles correlated with increased microhardness. The highest microhardness value, reaching 369 HV, was observed at a 30% duty cycle, whereas the lowest value, 239 HV, occurred at a 90% duty cycle.

Upon elemental mapping via EDS, it was evident that the zirconia content was higher at lower duty cycles. Specifically, the highest zirconium content, measuring 2.3%, was recorded at both 30% and 70% duty cycles, while the lowest, at 0.2%, was noted during direct current and a 90% duty cycle. SEM analysis elucidated compact and uniform surfaces across most duty cycles, except for direct current and a 90% duty cycle. Interestingly, at a 30% duty cycle, the surface exhibited exceptional compactness and uniformity.

Contrarily, roughness displayed a reverse behavior, increasing at lower duty cycles. The highest roughness value, measuring 0.25 μm, was observed at a 30% duty cycle, whereas the lowest, at 0.08 μm, occurred at a 90% duty cycle.

The current efficiency was above 90%.

In conclusion, the investigation into coatings containing 0.5 mmol/L of the brightener and 8 g/L nano-ZrO₂ revealed a clear correlation emerged between duty cycles and Vickers microhardness, with lower duty cycles associated with increased microhardness. Moreover, zirconium content was higher at lower duty cycles. SEM analysis illustrated compact and uniform surfaces across most duty cycles, except under direct current and 90% duty cycles. Notably, surfaces exhibited exceptional compactness at a 30% duty cycle. Contrary to microhardness trends, roughness increased at lower duty cycles. The highest roughness was observed at 30%, while the lowest occurred at 90%.

b. For 1mmol/L of 2-butyne-1,4-diol

For coatings containing 1 mmol/L of the brightener and 8 g/L nano-ZrO₂, the relationship between microhardness and duty cycles appeared less defined. The highest microhardness value, reaching 539 HV, was observed at a 70% duty cycle, while the lowest, 470 HV, was recorded at 90% duty cycle.

Similar to previous observations, the zirconium content was higher at lower duty cycles. Specifically, the highest zirconium content, reaching 6.1%, was observed at a 30% duty cycle, contrasting with the lowest value of 0.3% during direct current application.

Surface analysis revealed that the coating was consistently compact and uniform across various duty cycles, except at a 90% duty cycle where cracks were observed, indicating inferior coating quality.

In terms of roughness, no direct correlation with duty cycles was apparent. The highest roughness value, measuring 0.27 μm, was observed at a 30% duty cycle, while the lowest, at 0.2 μm, was recorded at a 50% duty cycle.

The current efficiency was above 70%, and reached 100% with 90% duty cycle.

These findings suggest a more complex relationship between duty cycles and coating properties for samples with 1 mmol/L of the brightener and 8 g/L nano-ZrO₂. The microhardness and roughness did not display a clear relationship with duty cycles. Similar to previous observations, zirconium content was higher at lower duty cycles.

c. For 2mmol/L of 2-butyne-1,4-diol

For coatings featuring 2 mmol/L of the brightener and 8 g/L nano-ZrO₂, the relationship between microhardness and duty cycles appeared to lack a clear pattern. The highest microhardness value, reaching 621 HV, was observed at a 30% duty cycle, while the lowest, 530 HV, occurred at 50% duty cycle.

Similarly, the zirconium content did not show a consistent correlation with duty cycles. The highest zirconium content, measuring 4.7%, was observed at a 50% duty cycle, whereas the lowest, at 1.7%, was recorded at a 70% duty cycle. This suggests that factors beyond duty cycles may influence the distribution of zirconium within the coatings.

Surface analysis revealed that the coating exhibited a very compact and uniform surface at all duty cycles, indicating high quality and uniformity of the coatings irrespective of the duty cycle applied.

In terms of roughness, a reverse trend was observed, where roughness increased with decreasing duty cycles. The highest roughness values, measuring 0.23 μm , were observed at 30% and 50% duty cycles, while the lowest, at 0.17 μm , was recorded at 90% duty cycle.

The current efficiency was reduced compared to lower concentrations of the brightener.

It is very important to note that, for both direct and pulse current, at every duty cycle, higher concentration of the brightener (2-butyne-1,4-diol) led to higher value of Vickers microhardness.

9.2 General conclusions

The incorporation of ZrO₂ nanoparticles into the coatings proved successful under both direct and pulse current conditions. Notably, pulse current resulted in higher zirconium content and yielded surfaces that were more compact, and uniform compared to direct current applications. Overall, Vickers microhardness levels were higher under pulse current compared to direct current, where the highest exhibited value was 621HV, at 30% duty cycle. Moreover, roughness levels ranging from 0.15 to 0.27 μm , indicating notably low roughness values under pulse current.

Furthermore, the addition of 2-butyne-1,4-diol emerged as an important factor in enhancing the mechanical properties and surface morphology of the coatings. The incorporation of this additive significantly contributed to the improvements observed in the coatings' mechanical strength and surface characteristics.

These findings underscore the effectiveness of nanoparticle incorporation, pulse plating and organic additive introduction in enhancing the performance and quality of the coatings.

9.3 Future work

Various directions can be considered as future development and utilization of the knowledge gained from this study.

The utilization of nanocomposite coatings, incorporating nano-ZrO₂ as the reinforcing agent alongside 2-butyn-1,4-diol as the organic additive, has yielded highly promising outcomes. To further enhance the properties of these coatings, considering that the efficiency of electrodeposition is influenced by various parameters of the process, future endeavors may involve exploring different duty cycles and frequencies during pulse plating. Additionally, assessing the behavior of the resulting coatings could entail examining various current densities and pH levels.

Furthermore, conducting Dynamic Light Scattering (DLS) studies to determine the hydrodynamic diameter of nanoparticles within the electrolyte, along with investigating their tendency to agglomerate during electrodeposition, could offer valuable insights.

Employing Ultrasonication treatment before electrodeposition could serve to further disperse the nanoparticles within the electrolyte, enhancing the uniformity of the coating.

Moreover, evaluating the corrosion rate through Tafel testing and the tribological behavior stand as a pertinent step in comprehensively understanding the performance of these coatings. These proposed avenues for future investigation aim to advance the understanding and optimization of nanocomposite coatings for various applications.

References

- [1] S. D. G. DARRELL D. EBBING, in *General Chemistry, 10th edition*, Cengage Learning, 2013, p. 1040.
- [2] N. Spyrellis, "ΤΕΧΝΟΛΟΓΙΑ ΕΠΙΜΕΤΑΛΛΩΣΕΩΝ," Athens, 1997.
- [3] P. F. Lang, "Is a Metal "Ions in a Sea of Delocalized Electrons?"," *Journal of CHEMICAL EDUCATION*, 2018.
- [4] J. d. p. Peter Atkins, "Materials," in *Physical Chemistry*, Oxford, UK, 2018.
- [5] J. ., D. G. R. William D. Callister, "The Structure of Crystalline Solids," in *Materials Science and Engineering: An Introduction, 10th Edition*, pp. 51, 78-79.
- [6] M. ASHCROFT, in *Solid State Physics*, Cornell University, 2012.
- [7] X. Z. J. C. a. S. L. Shaodong Sun, "Identification of the Miller indices of a crystallographic plane: a tutorial and a comprehensive review on fundamental theory, universal methods based on different case studies and matters needing attention," *NANOSCALE*, 2020.
- [8] T. E. o. E. Britannica, "Britannica," Britannica, [Online]. Available: <https://www.britannica.com/science/Bragg-law>.
- [9] W. Bollmann, *Crystal Defects and Crystalline Interfaces*, Berlin, 1970.
- [10] D. G. Barceloux, "Nickel," in *Clinical Toxicology*, Topanga, California, 1999, p. 20.
- [11] D. C. Adriano, "Nickel," in *Trace Elements in Terrestrial Environments*, 2001.
- [12] O. T. G. A. Serkan Saridag, "Basic properties and types of zirconia: An overview," *World of Stomatology*, 2013.
- [13] E. G. Y. P. P. Fedorov, "Zirconium dioxide. Review," *Condensed Matter and Interphases*, vol. 23, no. 2, pp. 169-187, 2021.
- [14] O. A. Graeve, "Zirconia," in *Ceramic and Glass Materials*, Springer, Boston, MA, 2008, p. 169–197.
- [15] P. R. J. A. H. W. J.-m. Kuljirarnat Jitwirachot, "Wear Behavior of Different Generations of Zirconia: Present Literature," *International Journal of Dentistry*, vol. 1, pp. 1-17, 2022.
- [16] C. H. Erich H. Kisi, "Crystal Structures of Zirconia Phases and their Inter-Relation," *Key engineering Materials*, Vols. 153-154, 1998.

- [17] U. E. R. Jens Eichler, "Mechanical Properties of Monoclinic Zirconia," *Journal of American ceramic society*, Vols. 1401-1403, 2004.
- [18] K. N. T. J. D. McCULLOVGH, "The Crystal Structure of Baddeleyite (Monoclinic ZrO₂)," *Acta Crystallographica*, vol. 12, p. 507, 1959.
- [19] T. B. Bayanova, "Baddeleyite: A Promising Geochronometer for Alkaline and Basic Magmatism," *PETROLOGY*, vol. 14, 2006.
- [20] "Wikipedia, the free encyclopedia," [Online]. Available: https://en.wikipedia.org/wiki/Baddeleyite#cite_note-8.
- [21] V. R. Palanisamy Manivasakan, "Synthesis of Monoclinic and Cubic ZrO₂ Nanoparticles from Zircon," *The American Ceramic Society*, vol. 94, p. 1410–1420, 2011.
- [22] "Formation of ZrO₂ Nanocrystals in Hydrothermal Media of Various Chemical Compositions," *Russian Journal of General Chemistry*, vol. 72, pp. 849-853, 2002.
- [23] B. T. R. V. J. Manish K. Mishra, "Synthesis and characterization of nano-crystalline sulfated zirconia by sol–gel method," *Journal of Molecular Catalysis A: Chemical*, vol. 223, p. 61–65, 2004.
- [24] D. C. M. Knight, "Composite Materials," *Encyclopedia of Physical Science and Technology (Third Edition)*, pp. 455-468, 2003.
- [25] E. b. K. U. Kainer, "Basics of Metal Matrix Composites," in *Metal Matrix Composites: Custom-made Materials for Automotive and Aerospace Engineering*, 2006, pp. 1-54.
- [26] T. E. Twardowski, "Nanocomposites Paste and Future," in *Introduction to Nanocomposite Materials: Properties, Processing, Characterization*, 2007, pp. 1-8.
- [27] M. Sen, "Nanocomposite materials," in *Nanotechnology and the Environment*, 2020, pp. 107-118.
- [28] E. V. N. L. C. N. C. G. N. K. Emmanuel Zoulias, "A REVIEW ON WATER ELECTROLYSIS".
- [29] S. K. Lower, "Chemical reactions at an electrode, galvanic and electrolytic cells," in *Electrochemistry*, 2004.
- [30] J. G. L.-P. R. G. C. Edmund J. F. Dickinson, "The electroneutrality approximation in electrochemistry," *Electrochemistry: Past, Present and Future*, no. 15, p. 1335–1345, 2011.
- [31] Z. Stojek, "The Electrical Double Layer and Its Structure," in *Electroanalytical Methods*, Greifswald, Germany, 2001.
- [32] D. C. GRAHAME, "THE ELECTRICAL DOUBLE LAYER AND THE THEORY OF ELECTROCAPILLARITY," 14 July 1947.
- [33] "BYJU'S," [Online]. Available: <https://byjus.com/chemistry/electrochemical-cell/>.

- [34] C. B. , A. B. , R. B. J.-F. C. M. C. J.-M. C. E. C. , S. C. , A. D. F. Y. D. K. D. D. D. L. Balogh, "Copper electroplating for background suppression in the NEWS-G experiment," *Nuclear Inst. and Methods in Physics Research, A*, 2021.
- [35] "LibreTexts CHEMISTRY," [Online]. Available: [https://chem.libretexts.org/Bookshelves/Analytical_Chemistry/Instrumental_Analysis_\(LibreTexts\)/22%3A_An_Introduction_to_Electroanalytical_Chemistry/22.01%3A_A_Electrochemical_Cells](https://chem.libretexts.org/Bookshelves/Analytical_Chemistry/Instrumental_Analysis_(LibreTexts)/22%3A_An_Introduction_to_Electroanalytical_Chemistry/22.01%3A_A_Electrochemical_Cells).
- [36] "Calculating Standard Cell Potentials Study Guide," 28 March 2023. [Online]. Available: <https://www.inspiritvr.com/calculating-standard-cell-potentials-study-guide/>.
- [37] H. Kahlert, "Reference Electrodes," in *Electroanalytical Methods*, Springer, Berlin, Heidelberg, 2009, pp. 291-308.
- [38] W. P. Hall, "LibreTexts CHEMISTRY," LibreTexts FREE THE TEXTBOOK, 2017. [Online]. Available: [https://chem.libretexts.org/Bookshelves/Analytical_Chemistry/Supplemental_Modules_\(Analytical_Chemistry\)/Electrochemistry/Voltaic_Cells/The_Cell_Potential](https://chem.libretexts.org/Bookshelves/Analytical_Chemistry/Supplemental_Modules_(Analytical_Chemistry)/Electrochemistry/Voltaic_Cells/The_Cell_Potential).
- [39] F. C. Walsh, "The Overall Rates of Electrode Reactions: Faraday's Laws of Electrolysis," *Transactions of the IMF*, 2017.
- [40] E. Gregersen, "Faraday's laws of electrolysis," The Editors of Encyclopædia Britannica, [Online]. Available: <https://www.britannica.com/science/Faradays-laws-of-electrolysis>.
- [41] M. D. P. P. Mohsen Ariana, "On the Analysis of Ionic Mass Transfer in the Electrolytic Bath of an Aluminum Reduction Cell," *THE CANADIAN JOURNAL OF CHEMICAL ENGINEERING*, vol. 92, 2014.
- [42] M. D. Merrill, Water Electrolysis at the Thermodynamic Limit, THE FLORIDA STATE UNIVERSITY, 2006.
- [43] S. N. Sengeni Anantharaj, "iR drop correction in electrocatalysis: everything one needs to know!," *Journal of Materials Chemistry A*, 28 March 2022.
- [44] "Polarization and Its Effect on Corrosion," [Online]. Available: https://www.corrosionclinic.com/corrosion_A-Z/polarization.htm#index.
- [45] "Coating.ca," [Online]. Available: <https://coating.ca/definition/polarization-curve/>.
- [46] W. Olberding, "An Introduction to Electrodeposition and Electroless Plating," *Modern Surface Technology*, pp. 101-119.
- [47] D. S. JAYAKRISHNAN, "Electrodeposition: the versatile technique for nanomaterials," 2012.
- [48] M. S. Saeid Mersagh Dezfuli, "Deposition of ceramic nanocomposite coatings by electroplating process: A review of layer-deposition mechanisms and effective

- parameters on the formation of the coating," *Ceramics International*, vol. 45, 2019.
- [49] D. B. & F. W. C. Kerr, "Electrolytic Deposition (Electroplating) of Metals," *Transactions of the IMF The International Journal of Surface Engineering and Coatings*.
- [50] K. D. A. K. D. S. D. B S B Reddy, "Pulsed co-electrodeposition and characterization of Ni-based nanocomposites reinforced with combustion-synthesized, undoped, tetragonal-ZrO₂ particulates," *IOPscience*, vol. 19, 2008.
- [51] H. B. Hassan Karami, "Electroplating Nanostructured Hard Gold through the Pulse Galvanostatic Method," *International Journal of ELECTROCHEMICAL SCIENCE*, vol. 7, 2012.
- [52] M. Y. H. T. T.-F. M. C. T. N. ., D. Y. T. K. K. M. Chun-Yi Chen, "Pulse-Current Electrodeposition of Gold," in *Novel Metal Electrodeposition and the Recent Application*, IntechOpen.
- [53] W. L. Y. C. X. C. Mingjie Li, "Nickel micro-pillar mold produced by pulse and pulse-reverse current electrodeposition for nanoimprint lithography," *Materials Letters*, vol. 301, October 2021.
- [54] A. S. N. S. S. Revathy Sreekumar, "Recent trends and developments in two-dimensional materials based electrodeposited nickel nanocomposite coatings," *FlatChem*, 2022.
- [55] N. Mandich, "PULSE AND PULSE-REVERSE ELECTROPLATING," *Metal Finishing*, vol. 97, no. 1, pp. 382-387, January 1999.
- [56] S. P. Q. J. R. G. C. K. d. A. M. C. L. Edinéia P. S. Schmitz, "Influence of Commercial Organic Additives on the Nickel Electroplating," *International Journal of*, vol. 11, pp. 983 - 997, 2016.
- [57] M. R. N. S. E.A. Pavlatou, "Synergistic effect of 2-butyne-1,4-diol and pulse plating on the structure and properties of nickel nanocrystalline deposits," *Surface & Coatings Technology*, vol. 201, p. 4571–4577, 2007.
- [58] G. F. H. a. F. P. KUPIECKI, "SOME REACTIONS OF 2-BUTYNE-1,4-DIOL," *Chemical Laboratory of the University of Notre Dame*, pp. 1601-1609, 1953.
- [59] "2-Butyne-1,4-diol pure cryst.," BASF, [Online]. Available: <https://products.basf.com/global/en/ci/2-butyne-1-4-diol.html>.
- [60] "2-butyne-1,4-diol," WIKIDATA, [Online]. Available: <https://www.wikidata.org/wiki/Q209328>.
- [61] M. J. P. a. V. J. C. Andrew G. McCormack, "Microstructural Development and Surface Characterization of Electrodeposited Nickel/Yttria Composite Coatings," *Journal of The Electrochemical Society*, vol. 105, 2003.

- [62] S. B. a. I. S. Challakere Ramadas Raghavendraa, "Electrodeposition of Ni-nano composite coatings: a review," *INORGANIC AND NANO-METAL CHEMISTRY*, 2019.
- [63] P. M. S. K. G. Ranit Karmakar, "A Review on the Nickel Based Metal Matrix Composite Coating," *Metals and Materials International*, 2020.
- [64] A. S. N. S. S. Revathy Sreekumar, "Recent trends and developments in two-dimensional materials based electrodeposited nickel nanocomposite coatings," *FlatChem*, vol. 36, November 2022.
- [65] "Knowlegde for a brighter future," Nickel INSTITUTE, 2023. [Online]. Available: https://nickelinstitute.org/media/lxxh1zwr/2023-nickelplatinghandbooka5_printablepdf.pdf.
- [66] A. K. N. REDDY, "PREFFERED ORIENTATIONS IN NICKEL ELECTRO-DEPOSITS," *J. Electroanal. Chem*, vol. 6, pp. 141-152, 1963.
- [67] H. N. ., M. S. ., Y. H. Akinobu Shibata, "Microstructural development of an electrodeposited Ni layer," *Thin Solid Films*, vol. 518, no. 18, pp. 5153-5158, 2010.
- [68] D. Y.-j. Z. W. X. T.-d. Xu Yang-tao, "Microstructure and texture evolution of electrodeposited coatings of nickel in the industrial electrolyte," *Surface and Coatings Technology*, vol. 330, pp. 170-177, 2017.
- [69] I. E. M. F. & G. M. J. Amblard, "Inhibition and nickel electrocrystallization," *Journal of Applied Electrochemistry*, vol. 9, p. 233–242, 1979.
- [70] M. F. e. N. S. J. AMBLARD, "O R I G I N E D E S T E X T U R E S D A N S L E S D E P O T S E L E C T R O L Y T I Q U E S," *Physique des Liquides et Electrochimie*, vol. 4, 1976.
- [71] M. A. T. M. M. S. M. A. K. W. Q. K. Ghulam Yasin, "Metallic nanocomposite coatings," in *Corrosion Protection at the Nanoscale*, pp. 245-274.
- [72] M. M. Dardavila, APPLICATION OF PULSE CURRENT FOR THE CO-ELECTRODEPOSITION OF MICRON-SIZED ZrO₂ PARTICLES IN Ni MATRIX UNDER STRONG AGITATION - STUDY OF MICROSTRUCTURE AND PROPERTIES OF THE COATINGS, Athens: NTUA, 2019.
- [73] M. A. T. M. M. S. M. A. K. W. Q. K. Ghulam Yasin, "Metallic nanocomposite coatings," *Corrosion Protection at the Nanoscale*.
- [74] K. N. S. H. H. I. Hamid S. Mahdi, "Improvement of Microhardness and Corrosion Resistance of Stainless Steel by Nanocomposite Coating," *Al-Khwarizmi Engineering Journal*, vol. 10, pp. 1- 10, 2014.
- [75] D. B. & F. W. C. Kerr, "Electrolytic Deposition (Electroplating) of Metals," *Transactions of the IMF The International Journal of Surface Engineering and Coatings*.
- [76] E. S. Guler, "Effects of Electroplating characteristics on the Coating Properties," in

Electrodeposition of Composite Materials, 2016.

- [77] S. B. & I. S. Challakere Ramadas Raghavendra, "Electrodeposition of Ni-nano composite coatings: a review," *Inorganic and Nano-Metal Chemistry*.
- [78] S. K. R. A. Iz. N. REDDY, "PREFERRED ORIENTATIONS IN NICKEL ELECTRO-DEPOSITS. II. A CONSIDERATION OF THE EFFECT OF DEPOSITION CONDITIONS ON THE TEXTURES DEVELOPED," *J. Electroanal. Chem.*, vol. 6, pp. 153-158, 1963.
- [79] A. O. S. U. B. & J. S. R. Ajay D. Pingale, "Effect of Current on the Characteristics of CuNi-G Nanocomposite Coatings Developed by DC, PC and PRC Electrodeposition," *JOM*, vol. 73, p. 4299–4308, 2021.
- [80] L. B. M. Ghaemia, "Effects of direct and pulse current on electrodeposition of manganese dioxide," *Journal of Power Sources*, vol. 111, p. 248–254, 2002.
- [81] A. A. A.M. Rashidi, "The effect of current density on the grain size of electrodeposited nanocrystalline nickel coatings," *Surface & Coatings Technology*, vol. 202, p. 3772–3776.
- [82] F. X. W. X. Z. N. W. X. L. H. KAN Hongmin, "Effects of Surfactants SDS and CTAB on Ni-SiC Deposition," vol. 33, 2017.
- [83] B. C. T. P. S. A. K. S. I. U. S. Mohanty, "Roles of organic and inorganic additives on the surface quality, morphology, and polarization behavior during nickel electrodeposition from various baths: a review," *Journal of Applied Electrochemistry*, 2019.
- [84] A. A. Azad MOHAMMED, "SCANNING ELECTRON MICROSCOPY (SEM): A REVIEW," in *International Conference on Hydraulics and Pneumatics - HERVEX*, Băile Govora, Romania, 2018.
- [85] A. K. Z. ., S. T. Raghavendra Kumar Mishra, "Chapter 12 - Energy-Dispersive X-ray Spectroscopy Techniques for Nanomaterial," *Microscopy Methods in Nanomaterials Characterization*, pp. 383-405, 2017.
- [86] E. g. U. & H. Y. A.-E. Andrei A. Bunaciu, "X-Ray Diffraction: Instrumentation and Applications," *Critical Reviews in Analytical Chemistry*, 2015.
- [87] M. B. A. I. Jean-Marc Schneider, "Statistical analysis of the Vickers hardness," *Materials Science and Engineering*, p. 256–263, 1999.
- [88] A. N. R.E. Smallman, "Chapter 5 - Characterization and Analysis," *Modern Physical Metallurgy (Eighth Edition)*, pp. 159-250, 2014.
- [89] B. Bhushan, "Surface Roughness Analysis and Measurements Techniques," in *Modern tribology handbook*, Ohio, 2000.
- [90] "STAHLI FEELING FOR FINISHING," [Online]. Available: <https://www.stahlusa.com/stahli-publication/the-technique-of-lapping/surface->

finish-quality/.

- [91] E. P. N. S. P. Gyftou, "Effect of pulse electrodeposition parameters on the properties of Ni/nano-SiC," *Applied Surface Science*, vol. 254, p. 5910–5916, 2008.
- [92] B. L. , T. M. , M. L. , M. H. Z. Y. H. C. Weiwei Zhang, "Effects of graphene oxide and current density on structure and corrosion properties of nanocrystalline nickel coating fabricated by electrodeposition," *Colloids and Surfaces A: Physicochemical and Engineering Aspects*, vol. 648, 2022.
- [93] N. M. K. S. Y. X. S. Q. B. Y. J. K. L. Zhaodi Ren, "Mechanical properties of nickel-graphene composites synthesized by electrochemical deposition," *Nanotechnology*, vol. 26, 2015.
- [94] H. K. , M. T. Mahdi Aghaee Malayeri, "Improving the properties of nickel/graphene oxide coated copper plate by changing the electroplating process conditions," *Results in Engineering*, vol. 18, 2023.
- [95] W. L. , F. Z. Y. S. H. L. L. Z. a. H. C. Han Rao, "Electrodeposition of High-Quality Ni/SiC Composite Coatings by Using Binary Non-Ionic Surfactants," *Molecules* , vol. 28, 2023.
- [96] R. Riastut, "The effect of saccharin addition to nickel electroplating on the formation of nanocrystalline nickel deposits," : *Materials Science and Engineering*, vol. 541, 2019.
- [97] C.-J. H. I.-M. H. & J.-T. C. K-L Lin, "Electroplating of Ni-Cr on steel with pulse plating," *JMEP*, vol. 1, p. 359–361, 1992.
- [98] R. S. M.E. Bahrolloom, "The influence of pulse plating parameters on the hardness and wear resistance of nickel–alumina composite coatings," *Surface & Coatings Technology*, vol. 192, p. 154 – 163, 2005.
- [99] D. F. V. A. G. Y. E. Kenneth Hili, "Nickel electroplating for high-resolution nanostructures," *Microelectronic Engineering*, vol. 141, 2015.
- [100] C. Kindred, "FACTS.NET," 11 October 2023. [Online]. Available: <https://facts.net/science/chemistry/14-astounding-facts-about-crystal-defect/>.
- [101] M. Sen, "Nanocomposite Materials," in *Nanotechnology and the Environment*, BoD – Books on Demand, 2020, 2020, pp. 107-118.